The morphological characteristics of normal fault traces in the Apennines, Italy

ELLIOTT, ROBERT,GILES

Department of Earth Sciences, University of Durham

The morphological characteristics of normal fault traces in the Apennines, Italy

A thesis submitted to the University of Durham for the degree of Master of Science (by Research)

Robert Giles Elliott

2018

Under the supervision of Prof Ken McCaffrey and Dr Jonny Imber

Research conducted at:

The Department of Earth Sciences,

University of Durham,

Science Laboratories,

DH1 3LE

Abstract

Fault trace ruptures at the Earth's surface show sinuosity (departure from linear trace morphologies) at a variety of scales in map view, reflecting the growth of the fault, the mechanical stratigraphy of the surrounding geology, and interactions with neighbouring faults. This study uses a combination of new remotely sensed LiDAR and SRTM datasets, and novel techniques which seek to eliminate the distorting effects of topography upon the fault traces.

The 2D morphological characteristics of fault traces are mapped and quantified. The relationships between those characteristics and scale of observation and other fault parameters are investigated, to see what insight those relationships afford into fault growth and interaction. By characterising controls of sinuosity at different scales, a better understanding of the effect of fault trace variations on seismic hazard evaluation in active tectonic regions may be obtained.

At the whole fault scale, stress interactions between neighbouring faults and between en échelon segments within a fault appear to be the main controls on trace sinuosity. Linear correlations between sinuosity values and fault length and slip rate respectively are weak. However, sinuosity appears to be smoothed out with repeated slip, particularly in central parts of the fault traces.

At smaller scale (<100 m), sinuosity is more variable and values spread over a wider range. Local features such as pre-existing fractures/weaknesses appear to be a principal control over deviation. Sinuosity is apparently not much influenced by the controlling factors at the whole fault scale.

The current regional extensional stress regime sees normal faults striking broadly SE-NW. Deviation from that pattern may be a significant factor in controlling sinuosity at the whole fault level. Here, anticlockwise deviance from the regional strike appears to coincide with an increase in sinuosity values. The anticlockwise variance brings the faults closer to a previous extensional regime, which left inherited structures trending broadly SW-NE. Those minor structures could be reactivated as transfer faults or segments between en échelon faults or fault segments, particularly in left-stepping situations.

Table of Contents

List of Figures

List of Tables

Acknowledgements

I would like to thank my two supervisors, Prof Ken McCaffrey and Dr Jonny Imber at the Department of Earth Sciences, Durham University for all their support, help, and encouragement throughout the year, which has been of great help to me. I would also like to thank my two internal reviewers, Dr Nicola De Paola and Prof Simon Mathias for their helpful suggestions during the review process.

Chapter 1 Introduction

1.1 Background to this study

Using a combination of recently available LiDAR and SRTM topographic datasets the objective for this study is to map and quantify the 2D morphological characteristics of fault traces, and to investigate the relationships between those characteristics and scale of observation and other fault parameters. The aim is to see if those relationships afford any useful insight how faults grow and interact.

Fault trace ruptures at the Earth's surface show sinuosity at a variety of scales. Fault traces in 2D or map view often display segmentation, bending and undulations, reflecting the growth of the fault, the mechanical stratigraphy of the surrounding geology, and interactions with neighbouring faults. Topography will often exaggerate some of the geometrical variations for non-vertical faults. Although sometimes modelled as planar features, fault planes are in nature far from planar, both at depth and at the surface. Surface trace orientations at small scale invariably depart from the overall strike of a fault. An example of a fault which departs frequently from a straight line along overall strike is the Parasano normal fault in the Abruzzo region, Apennines, central Italy, whose surface trace (transposed from Google Earth) is at **Figure 1** below.

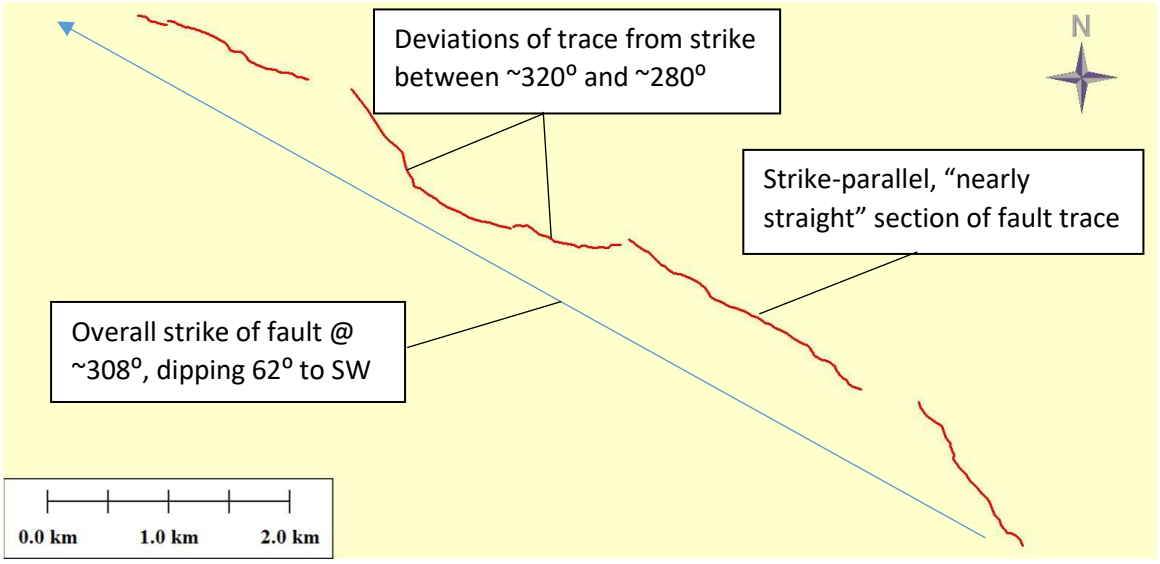

Figure 1 *Surface trace of Parasano fault, Abruzzo region, taken from a trace picked in Google Earth*

The Parasano fault trace is ~7 km in length. The overall strike is ~308°, with a fault plane dipping ~62° to the SW. However, within the trace segments shown, the strike varies

between ~320^{o} and ~275^{o}, and the amount of variation (and therefore sinuosity) varies along fault strike. The segment to the SE of the centre point of the fault is nearly straight, whereas the segment to the NW of the centre is obviously not.

In the field, the variations along strike are obvious at a variety of scales – **Figures 2 and 3** below are photographs of sections of the Fiamignano and Campo Felice faults (both normal faults from the Abruzzo region) at scales of ~0.25 km, **Figure 4** is a photograph of a section of the Magnola fault (Abruzzo) at a scale of 20 m. All show clear variations from strike at a variety of scales.

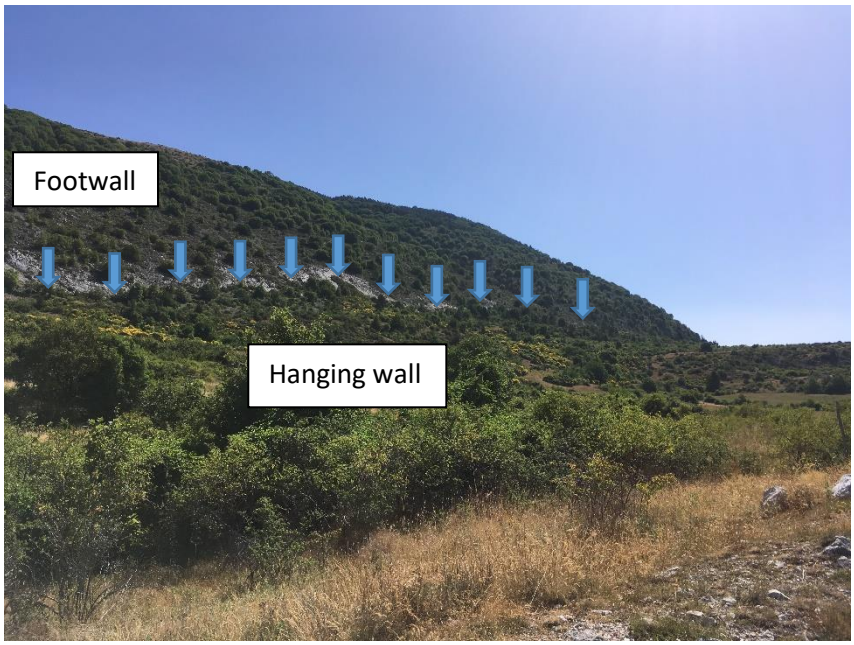

Figure 2 *Photograph of section of fault scarp shown with blue arrows (exposed limestone footwall) from Fiamignano fault, Abruzzo, looking NE, distance across centre of photograph ~250 m*

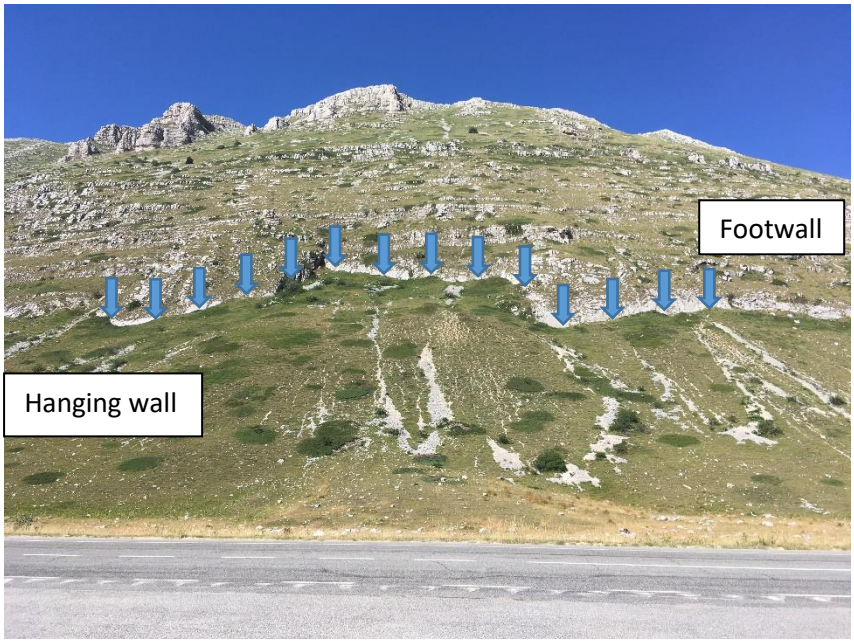

Figure 3 *Photograph of section of fault scarp shown with blue arrows (exposed limestone footwall) from Campo Felice fault, near Campo Felice ski resort, Abruzzo, looking NE, distance across centre of photograph ~200 m*

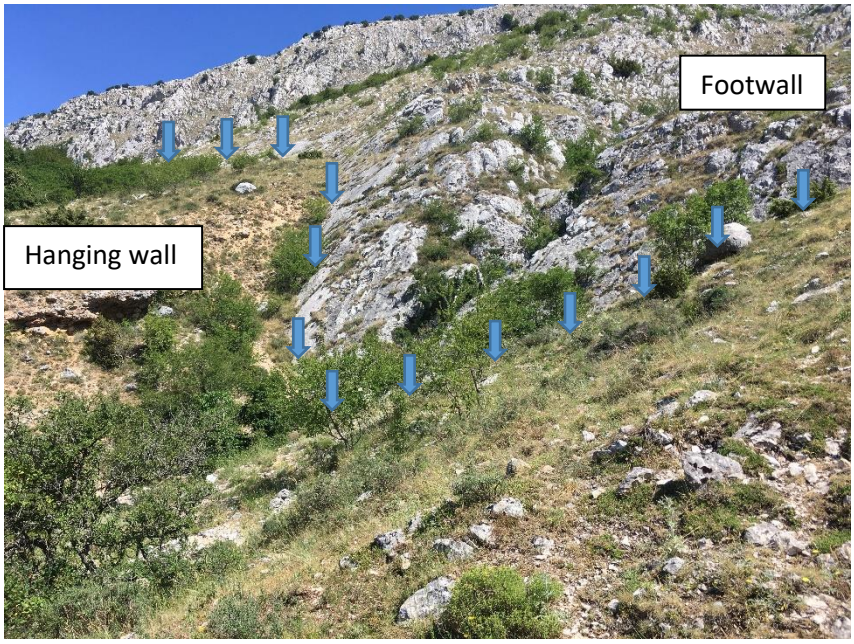

Figure 4 *Photograph of section of fault scarp shown with blue arrows (exposed limestone footwall) from Magnola fault, near Forme village, Abruzzo, looking NW, distance across centre of photograph ~20 m*

This study aims to use a geomorphological approach to seek to ascertain the factors which might influence trace morphology, using a combination of GIS and modelling techniques.

The concept of ascertaining a Sinuosity Index value is one commonly used to quantify the morphology of river systems. In more complex braided river systems, a variety of indices are used, some of which reflect both the down-river sinuosity, and the degree to which the river bed is braided (Leopold, Wolman and Miller, 1964 and Mueller 1968). However, in single channel river systems a more common approach is to assess "total sinuosity" by calculating straight line (reach length) against the length of the middle of the channel (an alternative is to measure that length by using the tal weg). The geometry of a river bed will also typically include an element of concavity, which will vary along the profile of the river from source to discharge. Therefore, the calculation is in the path defined by the direction of the maximum downslope. The resultant values are used to define a river's sinuosity by a set of commonly used categories - ≤1.05 = almost straight, 1.05-1.30 = sinuous, 1.30-1.50 = moderately meandering, >1.50 = meandering (e.g, Horacio 2014).

In an analogous context, "squirreliness" is an "unofficial" term used in the UCERF (Uniform California Earthquake Rupture Forecast 3). It denotes TAAD, or Total Absolute Angular Deviation, a measurement of the extent to which the surface trace of a fault rupture deviates internally from the overall strike of the fault. Studies of the morphology of map view fault traces (including TAAD) have been undertaken by Biasi and Wesnousky (2017 and 2018), based upon a database of faults of varying types (strike-slip, normal and thrust faults). Those faults are all in excess of 5 km in length, spread throughout the world with varying lithologies. No allowance is made in those studies for the effect of topography upon the traces, and the studies are limited to one scale of observation.

Recent research has identified bends in fault traces as possibly important factors in rupture propagation, with bends acting as stress barriers, preventing propagation and controlling the magnitude of main shock ruptures (Cowie et al 2017).

In this study the aim is to use more detailed fault mapping than that used by Biasi and Wesnousky in the form of LiDAR and SRTM images, to analyse a homogeneous set of known active normal faults from one area, the part of the Apennines in the Abruzzo and Umbria regions of central Italy. It is proposed to seek to minimise the potentially distorting effect of topography upon the fault traces, by projecting the traces onto a plane orthogonal to the slip direction of the faults. The more detailed data, and the more homogeneous target set of faults, should enable an investigation of the relationships

between sinuosity and scale of observation, fault length and slip, and to investigate the results in the context of proposed growth models for faults (Jackson et al 2017). Any significant relationships found may help give an insight into fault growth, and aid the process of hazard prediction in areas that have a long history of unpredicted fault movement causing significant loss of life and damage to property.

1.2. Hypotheses and questions to be addressed

1.2.1. Coulomb shear stress change at the whole fault scale

It is expected that the principal control on sinuosity at the whole fault scale (traces of >1 km) will be the Coulomb shear stress change resulting from movement on neighbouring faults, or en échelon segments of the fault through hard linkages such as fault bends or breached relay ramps. The local geometry, relative positions of the faults concerned and fault slip history, together with regional stress patterns, and the presence of inherited structures from previous deformation, are likely to be important factors influencing the surface morphology at the whole fault scale. Stress interactions between faults or fault segments are likely to cause faults to grow towards or away from each other, causing deflections from straight line strikes, which will impact upon sinuosity values.

1.2.2. Relationships between sinuosity and common factors at the whole fault scale

At the whole fault scale, it is expected that there should be some degree of correlation between sinuosity values and factors common to a number of the faults, with observable relationships. Those factors may include length of fault, rate of slip, strike of the fault, and whether the trace is towards the middle or tip of a fault. Continued growth and slippage of a longer fault might be expected to smooth out more sinuous segments than a shorter fault. A higher rate of slip might be expected to result in higher sinuosity values, as more distortion is experienced over a shorter period of time. A fault whose strike is near parallel to the regional predominant extensional regime may be more likely to propagate through linkages along strike, and therefore to be less sinuous than a fault whose strike deviates significantly from that pattern. Repeated slip events might be expected to have an evening-out effect (and lower sinuosity values) towards the middle of a fault, rather than at its tips.

1.2.3. Localised influences at smaller scale

At a smaller scale (investigating fault segments below ~100m in length), the sinuosity values are expected to be more locally influenced, and stress transfer from neighbouring faults correspondingly less important. It is expected that the primary controls on sinuosity at such a localised scale might be near-surface factors such as fracture patterns (which may in turn be a reflection of inherited structures or shallow fault plane variations such as bifurcation).

1.2.4. Sinuosity values dependent upon scale of observation

It is expected that sinuosity values will be dependent upon the scale of observation. At a smaller scale (below ~100m in length) sinuosity values may deviate from those seen at a larger scale, and the models of stress change from slippage on neighbouring faults or en échelon fault segments will be of relatively little application. It is also unlikely that there will be common observable relationships. Therefore, it is expected that sinuosity values will be more variable, and that the sinuosity values of the smaller scale traces would cover a wider range of values than those for longer fault traces, as the effect of localised more variable sinuosity would be smoothed out over longer fault traces as the growth of a fault evolves.

Chapter 2 Literature Review

2.1 History of deformation in the Apennine region, Central Italy

The Apennine region in central Italy is widely recognised as being an area within peninsular Italy which is currently dominated by NE-SW extension (with normal faults trending ~NW-SE, dipping to the SW). The Adriatic region to the NE of the Apennines is identified by Anderson and Jackson (1987) as currently being very stable, with N-S shortening in Northern Italy, and anti-clockwise movement about a pole in Northern Italy, with arguably equal extension and shortening of ~2mm y^{-1} in Italy and what was previously Yugoslavia resulting from that rotation.

The history of the development of the current extensional regime is related to the evolution of a thrust front associated with subduction of the Eurasian plate beneath the African plate. Jolivet et al (1998) considered the history of the central Mediterranean region encompassing the North Tyrrhenian and Aegean Seas from the Eocene (55.8 Ma b.p.) to present day. In their view, during the Eocene, westward subduction of the Eurasian plate below the continental basement of Corsica (African plate) led to the creation of an accretionary complex, with associated shear zones of ~100-200 km. The thrust front migrated eastwards, with extension developing in the back arc region. The extension associated with the shear zones migrated from W to E from Corsica across the Tyrrhenian Sea in the early Miocene. This migration followed the eastward movement of the Apennine compressional front. The subduction led to the development of a Miocene-aged metamorphic core complex associated with partial melting. Behind this, extension led to rifting and ultimately formation of the Tyrrhenian Sea. The extension associated with the shear zones migrated to the Apennine region itself from the Miocene to the Pliocene (5.3 - 2.6 Ma b.p.) with the subduction zone retreating eastwards during roll-back, accompanied by shallow E dipping extensional shear zones at depth at the brittle-ductile transition. Further migration eastwards of the thrust front from the late Pliocene to the present has led to the W dipping normal faults in the Apennines which now accommodate extension on the E side of the volcanic arc, with slow convergence of the plates continuing in the Adriatic Sea.

Figure 5 below shows the evolutionary model suggested by the authors.

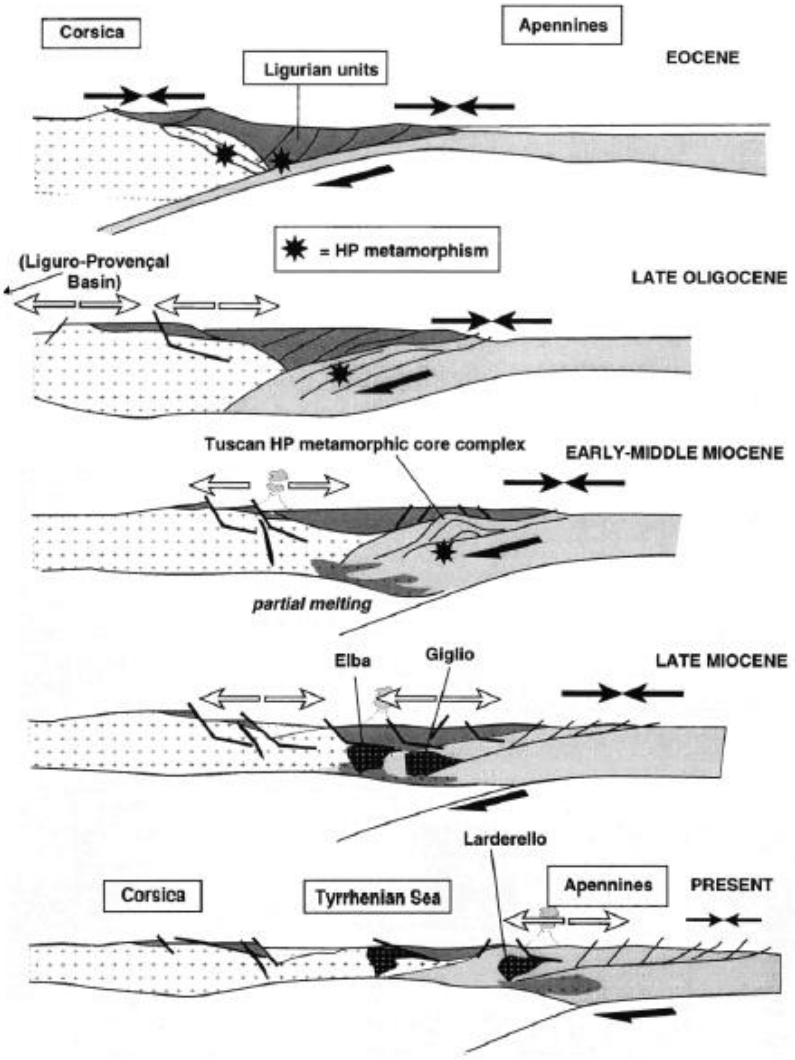

Figure 5 *Figure 20 from Jolivet et al, 1998, showing their evolutionary model of the central Mediterranean region from the Eocene to present day.*

More recently, the dominant control on the morphology of the Apennine region has been glaciation. Giraudi and Frezzotti (1997) analysed the glacial evidence from the Gran Sasso Massif area with a view to trying to constrain the last glacial maximum and retreat of glaciers in central Italy. They suggested that the last maximum was ~22,600 years b.p. (the Campo Imperiale Stadial), and the glacial retreat started ~21,000 years b.p., which left three recessional moraines. The interstadial was followed in turn by a stadial at ~16,000 years b.p. (the Fontari Stadial), further retreat at ~ 15,000 years b.p. with four more recessional moraines, and most recently the Monte Aquila Stadial of ~11,000 years b.p.

2.2 Analyses of normal faulting in the Abruzzo and Umbria regions of the Apennines, Central Italy

Since 2000 there have been a number of studies analysing the extensional faults in the Lazio-Abruzzo region of the Apennines, with a view to constraining the driving forces behind the frequent fault activity in that area, seeking to aid hazard prediction. The work by Giraudi and Frezzotti (1997) has helped to provide a basis for calculation of slip rates on visible fault traces on the surface, averaged over the period since the last glacial maximum. The prominent largely Mesozoic limestone scarps have proved a fruitful basis for such studies, offsetting the "regional marker" afforded by the last glacial maximum at ~16-18 ka b.p. Many of the studies have worked on refining methods of analysing the amount and timing of slip on many of the faults over the period since the last glacial maximum, relating slip to fault morphology, and modelling the interaction between neighbouring faults through stress build up.

Roberts and Michetti (2004) measured the geometry, kinematics and rates of extension of 17 active largely parallel faults trending NW-SE in the Lazio-Abruzzo region. The array studied consisted of individual faults each of some 20-40 km length spread over a region of 155 km length, 55 km across strike. **Figure 6** below shows the area studied.

The study relied principally on published geological maps and fieldwork, although the authors highlighted difficulty in assessing fault length with certainty. Throw profiles were constructed, and throw averaged over a period of 18 ka. Maximum throw rates and throw rate gradients were identified on the centrally located faults, and the authors identified a relatively recent change from more random movement within the array to higher growth rates associated with the centrally-located faults (such as the Sulmona, Fucino and Liri Faults). The authors speculated that this was because of interaction between adjacent faults and represented a concentration of stress over time. The throw rate database was shown to be compatible with both the recent historical record of seismic shaking in 14 local towns (since 1349 A.D.), and models of normal fault growth (Roberts et al, 2004).

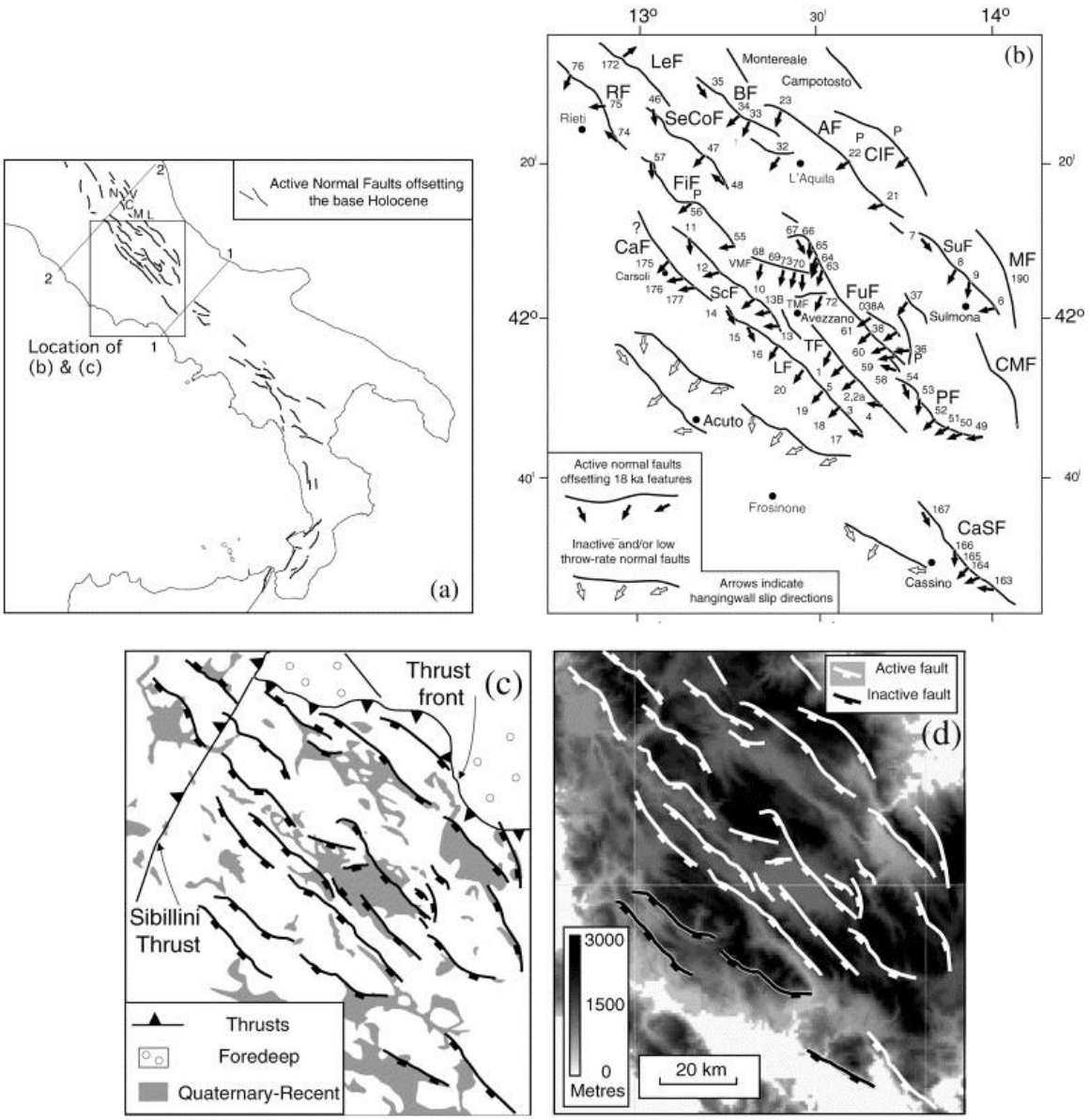

Figure 6 *From Roberts and Michetti, 2004, figure 2. Location maps for their study area. (a) Map of central-southern Italy showing major active normal faults that have slipped after the end of the last glacial maximum at 18 ka. N—Norcia Fault; C— Cittareale Fault; M—Montereale Fault; L—Laga Fault; V—Mt. Vettore Fault. (b) Map of Lazio–Abruzzo showing active and inactive normal faults. RF—Rieti Fault; LeF—Leonessa Fault; SeCoF— Sella di Corno Fault; FiF—Fiamignano Fault; BF—Barete Fault; AF—L' Aquila Fault; CIF—Campo Imperatore Fault; CaF—Carsoli Fault; ScF—Scurcola Fault; LF—Liri Fault; FuF—Fucino Fault; TF—Trasacco Fault; PF—Pescasseroli Fault; SuF—Sulmona Fault; MF—Maiella Fault; CMF—Cinque-Miglia Fault; CaSF—Cassino South Fault; VMF—Velino-Magnola Fault; TMF—Tre Monti Fault. (c) Simplified geological map of Lazio–Abruzzo showing Quaternary hanging wall basins to normal faults. (d) Fault map overlain on a 1 km2 pixel, digital elevation model.*

Two regions of highest strain rate were identified, Lazio-Abruzzo, and SE Campania and Basilicata by Faure Walker et al (2012) (see **Figure 7** below). That study investigated the

correlation between elevation, upper-crust strain rate, and upper-crustal finite strain within the Apennines.

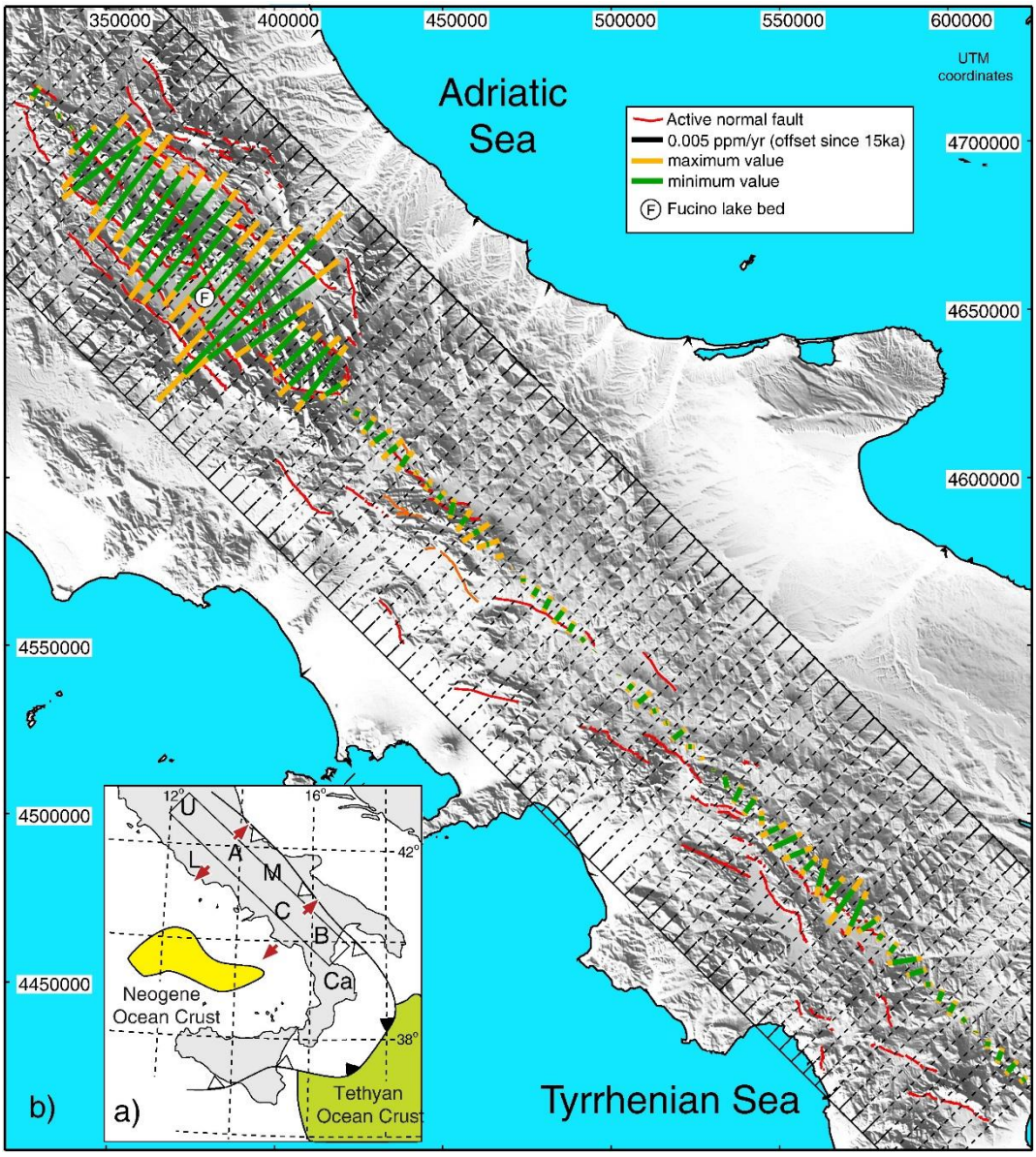

Figure 7 *From Faure Walker et al, 2012, Fig. 1. Map showing the spatial variation in principal horizontal strain calculated in 5×90 km boxes (dashed lines) traversing the Italian Apennines, derived from the directions and magnitudes of faulted-offsets since 15±3 ka of landforms dating from the last glacial maximum. (a) Location of study area indicated in the inset box. (b) SRTM DEM with strain rate bars overlain with a UTM grid. U = Umbria, L = Lazio, A = Abruzzo, M = Molise, C = Campania, B = Basilicata, Ca = Calabria*

Both regions identified are areas of raised topography (>600 m). They overlie mantle regions with relatively-long spatially-interpolated SKS delay times (1.2–1.8s) indicating anisotropy, suggesting relatively-high mantle strains, and high free gravity measurements. The intervening regions with lower upper-crustal strain rates and lower

elevations overlie mantle with shorter SKS delay times and lower free gravity measurements. Therefore, it would appear that mantle upwelling through a slab window may account for uplift/extension in the Abruzzo region and control strain rates in the upper crust. There might be higher strain rates at the sides of the slab window, which could also be relevant to the movement seen at the surface.

In order to constrain the slip history of an individual fault over the last 15 ka, cosmogenic ^{36}Cl surface exposure dating techniques were used by Palumbo et al (2004) on the central part of the Magnola Fault in the Abruzzo region, with samples taken from a 20 cm wide, ~2.5 cm deep sampling site based upon one well-exposed 10m high limestone scarp above the village of Forme. The conclusions drawn from the ^{36}Cl data were that there had been 5-7 earthquakes between about ~12-5 ka b.p., each producing slip of between ~1.5 and 3 m, with a suggested slip rate of ~0.8mm/annum. As there has been no activity in the last 5,000 years, there has either been an extended period of quiescence with a long recurrence time, or a future earthquake event is imminent. A similar result for the Magnola Fault was recorded by Schlagenhauf et al (2011), using similar techniques.

At an intra-fault scale, Faure Walker et al (2009) investigated a relay zone on the Parasano-Pescina Fault, considering the relationship between throw and the 3D orientation of the breaching faults crossing relay zones. The fault shows double maxima, but with a displacement deficit in the former relay zone after the linkage formed. The authors suggested that the displacement deficit was because the relay is much newer, but that it will catch up with the other parts of the fault in time, because the displacement rate is faster, due to the oblique strike of the breaching fault, and its relatively high dip. It needs to have a horizontal strain rate concomitant with its position at the centre of the overall fault. Therefore, whether the throw minima at fault linkage locations are preserved during progressive slip depends upon the 3D orientation of the breaching fault. The authors noted that the horizontal strain across a fault, its throw, its kinematics and its strike and dip are interlinked variables, and that without regard to all of those variables in 3D space, simply taking fault throw rate across a fault may not accurately reflect fault activity rates.

Terrestrial laser scanning images (LiDAR) were used by Wilkinson et al (2014) to investigate a central 5 km section of the Campo Felice Fault. The authors found that changes in fault strike can produce local maxima in throw rates of ~25% at relay zones. Despite a simple linear decrease in strain-rate along strike towards to the fault tip, a change in fault strike produced a localised anomaly in vertical motion, with the throw-rate increasing by ~40% close to the fault bend. Both Faure Walker et al (2009) and this study cautioned against the use of planar or simplified models to predict sub-surface geometry, or to model strain transfer to adjoining faults through sub-surface linkage. The geomorphology of the fault bends is a key element in constructing models of stress transfer.

GPR (Ground Penetrating Radar) was used by Bubeck et al (2015) to examine the extent of the footwall below the accumulated hanging wall sedimentation at the Magnola, Fiamignano and Tre Monti faults in the Abruzzo region, and TLS (Terrestrial Laser Scanning) to examine the exposed surface of the fault trace. By combining the two datasets, the authors showed how contamination of the results for accurate ^{36}Cl dating could result from processes of footwall incision, erosion, channel incision, hanging wall sedimentation and landsliding. The geomorphology of the sites varied considerably over relatively short distances, with many of those geomorphic processes combining with fault slip to produce the hanging wall exhumation seen on the ground. The authors showed how those effects can be differentiated in order to identify suitable sites for accurate ^{36}Cl dating.

Variations in cosmogenic ^{36}Cl were used by Cowie et al (2017) to constrain fault slip rates on the Fiamignano, Magnola, Tre Monti, Fucino, Parasano, San Sebastiano, Frattura and Pescasseroli faults in the Abruzzo region. The authors used sample ladders parallel to the slip vector, LiDAR and GPR data and trenches in the hanging wall colluvium. The findings from the analysis were that, in general, across the Apennines, the SW fault flanks are no longer active, and deformation is concentrated in the more active NE flank, as exemplified by the Colforito, L'Aquila, Vettore/Norcia sequence from 1997-2017. An averaged strain rate over the Holocene is approximately symmetrical on both flanks. The methodology employed involved sampling a buried portion of each fault, comparing that to an

exhumed section. The authors used LiDAR and GPR to rule out the effects of erosion and landsliding. The results showed varying slip rates and periods of high slip rate which are not synchronous (and probably not, therefore, climate-controlled), with episodic behaviour. The authors noted short periods of activity when the faults are slipping, but long quiescence when not, with a possible explanation that accumulation of finite slip progressively increases energy dissipation. Slip rates also vary over time, with healing between slip increasing the frictional strength of inactive faults, Alternating fault activity was predicted between the NE and SW flanks, with the recent concentration of slip movement on the NE flank a "snapshot" in time.

The importance of detailed along-strike throw rate or slip-rate profiles and variable fault geometry has been considered by Faure Walker et al (2019). The authors found that, for fault-based seismic hazard prediction, caution should be used where making assumptions and using models to simplify the shape of the fault (such as no max, boxcar and triangular fault displacement profiles), and to adopt a planar image of the fault. Using detailed slip data and geometry from 14 normal faults in the Apennines (Campo Felice, Liri, Barisciano, Roccapreturo, Parasano, Pescasseroli, Scanno, Carsoli, Trasacco, Fucino, Ocre, San Sebastiano, Fiamignano and Sulmona), the authors showed the degree of inaccuracy achieved in using those models (as opposed to the data available) to predict strain rates across the faults, source-to-site distance for ground motion, recurrence intervals and ground shaking intensities. In many cases the results produced by use of the simplified models are well outside the error margins of calculated strain rate/recurrence intervals predicted using the detailed data (see **Figure 8** below, figure 3 from the paper).

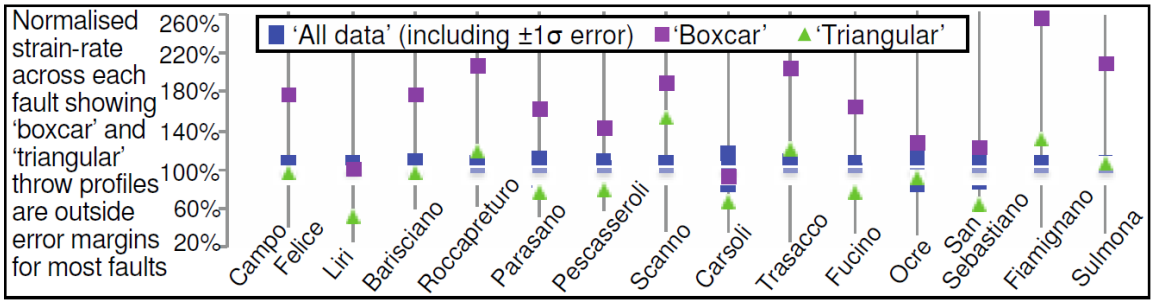

Figure 8 *Figure 3 from Faure Walker et al, 2019: Strain-rates calculated across 14 faults using different throw-rate profiles: 'all data' case (blue rectangles including ±1σ), 'boxcar' (purple squares), and 'triangular' (green triangles). The strain-rates calculated using simplified throw-rate profiles are shown relative to those calculated using the 'all data' throw-rate profiles. The inferred*

strain-rates calculated using simplified throw-rate profiles mostly lie outside ±1σ uncertainty of the 'all data' strain-rates.

The build-up of stress on the Mt Vettore, Laga and Norcia Faults from coseimic loading (using historical and palaeoseismic earthquakes) and interseismic loading was analysed by Mildon et al (2017) using strike-variable fault geometries constrained by fieldwork in Coulomb stress modelling. The build-up prior to the earthquakes in 2016-17 implies that ruptures generated stress heterogeneities that correlate with the limits of the main shock ruptures. Therefore, the authors suggested that stress barriers appear to be a primary control on the propagation of the faults, and the magnitude of the main shock ruptures. It had been suggested that the 2016 earthquakes filled a seismic gap resulting from the 1997 Umbria-Marche and 2009 L'Aquila earthquakes, as events increasing stress. The modelling by the authors showed that the long build-up of stress on the Mt Vettore Fault, compared to the relatively recent earthquakes on the Laga and Norcia Faults, produced the highest accumulation of stress at depth, and influenced how the stress patterns developed in 2016. The bends in the Mt Vettore Fault appear to have acted as stress barriers, preventing rupture propagation. The positive stress at depth remaining after the release of stress towards the surface may have meant that zero or low Coulomb stress patches were nevertheless reactivated. The authors suggested that models of seismic hazard analysis need to include not only the transfer of stress between adjacent faults during earthquakes, but also factor in the history of stress build-up across those faults.

Subsequent research by Walters et al (2018) investigating the same (Mt Vettore) fault sequence in 2016, has analysed a variety of geodetic, seismological and field data, and suggested that the principal control on the extent and termination of fault ruptures was the interaction of fault segments with pre-existing minor structures. Fluid diffusion along those structures possibly plays a role in determining the timing of the sequences involved.

The relative importance of co-seismic stress changes versus inter-seismic stress accumulation for earthquake occurrence and fault interaction was investigated by Wedmore et al (2017), looking at historical records of 30 earthquakes since 1349 A.D to model elastic interactions between 97 faults in central Italy. Nearly all earthquakes occurred on faults where there was accumulated (positive) loading stress. The pattern of

earthquakes which fail is not random, and statistically earthquakes are more likely to occur on faults with higher levels of Coulomb stress. Coulomb stress changes can alter earthquake recurrence times by significant amounts (up to 1000 years, lower or higher), and fault length determines the intensity of this effect. The stress changes seem to have a greater effect on shorter faults in areas with lower slip rates.

2.3 Pre-existing structures and fracture patterns in the Abruzzo and Umbria regions of the Apennines, Central Italy

In addition to the pattern of Quaternary extensional faults trending NW-SE across the region, the previous history of the region has resulted in pre-existing tectonic features which continue to influence the current tectonic regime, and which have been investigated by a number of researchers in order to better understand the factors which control fault movement in the region. Principal among those structures are the NNE-SSW and ENE-WSW extensional structures which Pizzi and Galadini (2009) suggested were not major seismological sources in this region, but could be locally reactivated as transfer faults between two en échelon NW-SE trending normal faults, where the faults are located in a favourable setting (typically in a left-stepping arrangement). Otherwise, they are more likely to act as barriers to fault propagation. Reactivation of pre-existing NW-SE structures from the late Pliocene/early Miocene thrust tectonics is more favoured, given the favourable alignment to the present extensional regime (Pizzi and Scisciani 2000).

Civico et al (2017) identified NNE-SSW pre-existing structures as being cross-cut by the NW-SE trending Paganica-San Demetrio Fault System. In that study, the inherited NNE-SSW and ENE-WSW structures were identified as a likely major control on the basin shape in the Middle Aterno Valley, Abruzzo region, the location of the 2009 L'Aquila earthquake, which lies ~8 km to the NE of the Campo Felice Fault. The inferred NNE-SSW and ENE-WSW structures are F1, F7 and F8 on **Figure 9** below (Figure 8 from the study). Those structures are in turn possibly cross-cut by later NW-SE trending inferred buried faults.

Fracture patterns appear to have been relatively little studied in the Abruzzo region (possibly because it is not known as a major hydrocarbon reserve). However, studies of

the Upper Triassic and Lower Miocene platform carbonates in the Southern Apennines have considered the development of the fracture structure over time in a similar setting.

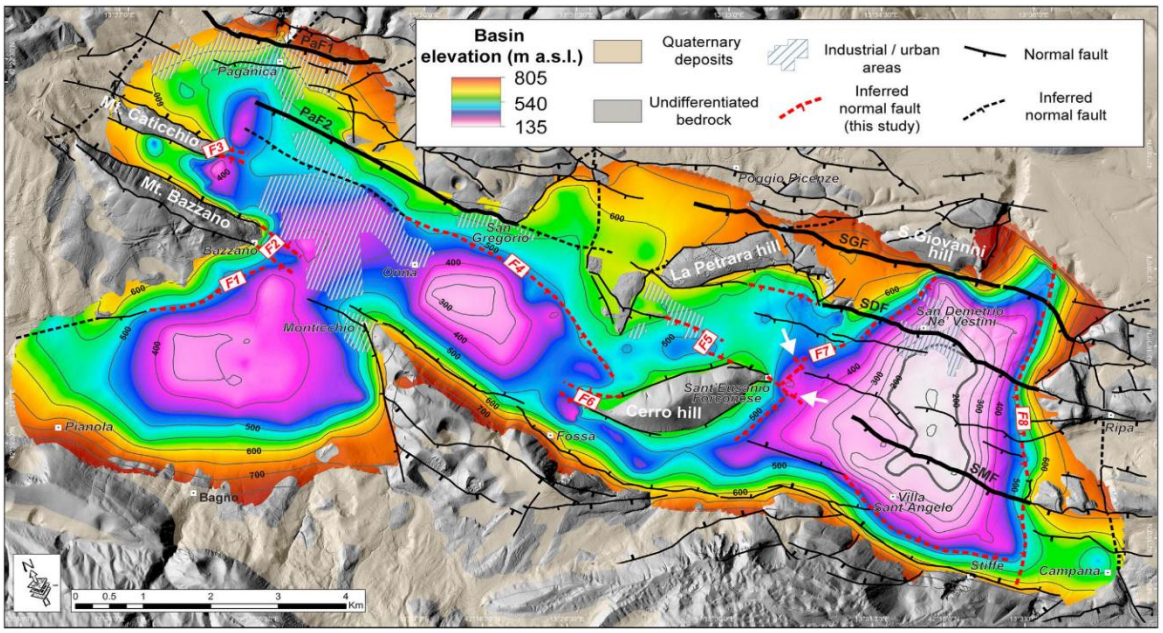

Figure 9 *Figure 8 from Civico et al, 2017, Shape of the continental basin bottom (contour interval 50 m). The basin architecture is compared with the fault system at the surface [modified after Pucci et al., 2014]; inferred buried normal faults are shown in red; major faults of the PSDFS are shown in black bold lines: PaF1, Paganica Fault; PaF2, San Gregorio splay of the Paganica Fault; SGF, San Giovanni Fault; SDF, San Demetrio Fault; SMF, San Mauro Fault. The white arrows indicate the deflection of the elevation contour lines possibly related to the activity of NW-SE trending inferred buried faults. The bold grey elevation contour line encloses the base of the SDD depocenter. Note the rotated north arrow.*

Vitale et al (2012) investigated the development of fracture networks in poly-deformed carbonate reservoir analogues in Mt Chianello, Southern Italy. The fracture sets found in the cretaceous carbonates in the platform are shown in Stereonet (a) in **Figure 10** below (an extract from Figure 6 in the study), with two sets of steeply dipping fractures orthogonal to the bedding planes. The fracture sets show near vertical fractures trending NNE-SSW and WNW-ESE. Stereonets (b) and (c) show the fracture sets in early Miocene carbonate deposits, with similar characteristics. Stereonet (e) shows all of the fracture measurements adjusted to restore the bedding to the horizontal. These extensional features are assumed to have derived from normal faulting associated with lithospheric bending during a forebulge setting. Although the region was subsequently subject to

thrusting and strike slip faulting (transpression) and further extension, overprinting those fractures to a degree, the “background” network remains largely unaffected.

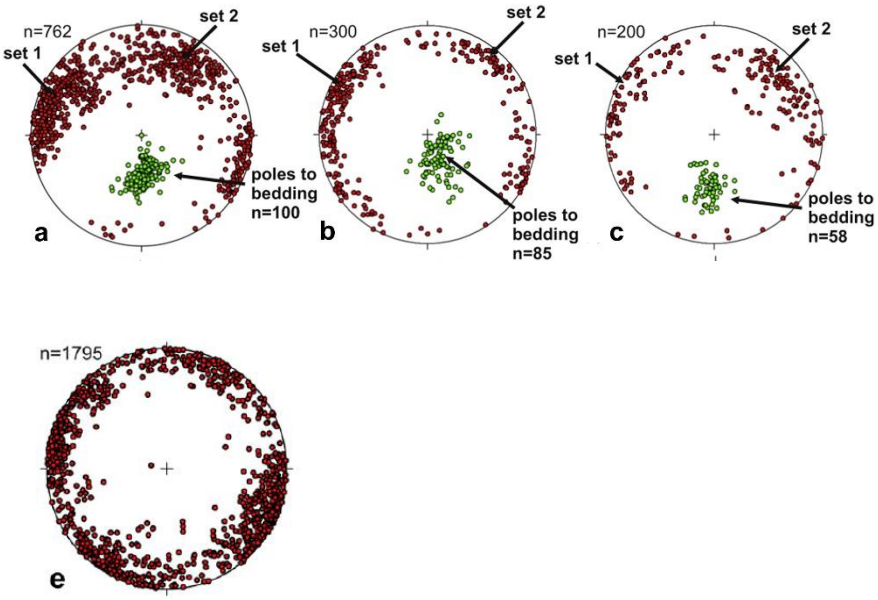

Figure 10 *Extracts from Figure 6 from Vitale et al, 2012, from Mt Chianello region, Southern Apennines - a. Poles to fractures and bedding planes Cretaceous Carbonates, b. and c. Poles to fractures and bedding planes from Early Miocene Carbonates, e. all poles to fractures, adjusted to restore bedding to horizontal.*

Similar work was carried out by Guerriero et al (2010) and (2011) on platform carbonates at the Sorrento Peninsular, Naples, and by Marchegiani et al (2004) further N, at the NE external zone of the Apennines (Majella Mountain) with similar results.

2.4 Surface rupture traces morphology

Marchal et al (2001) first developed the concept of fault morphology to describe geometric variations along dip and strike directions of the fault plane, including bends, jogs and undulations. Subsequently this has been applied to analysing surface rupture traces.

Wesnousky (2006), Wesnousky (2008), Biasi and Wesnousky (2016) and Biasi and Wesnousky (2017) developed a methodology for analysing surface rupture traces for distinguishable fault patterns (or morphology) related to the geometry of those traces. Biasi and Wesnousky (2016) analysed the mappable discontinuities (fault ends or steps of >1 Km between faults) evident in the rupture traces of 67 historical, large-scale faults.

Biasi and Wesnousky (2017) analysed the same rupture traces for map-scale features such as fault bends, discontinuous rupture, overlaps and fault-fault step-overs. In both studies, the authors were seeking to analyse statistical relationships potentially relevant to PSHA (Probabilistic Seismic Hazard Analysis).

The data set used by the authors was common to both the 2016 and the 2017 papers. It consisted of maps of 67 historical, large-scale faults, drawn from surface rupture maps and related published literature, put into common format. The measurements were limited to where the fault branches at both ends are at least >7 km. Only comparatively large-scale features were analysed. The 2016 paper tabulated steps and gaps of >1 km. The 2017 paper looked at linear fault sections of 5-7 km minimum length, as there is room for local rupture dynamics to overcome features of a shorter length.

Map view was used, as little or no data was available to the authors about the changes in the 3D geometry or dip, and map view is generally seen as the starting point to identifying where to concentrate investment in 3D geometry resolution. No 3D geometry was recorded. Some degree of smoothing was used through the small angle deviations of the longest ruptures.

The 2017 paper:

1. Measured and tabulated the angles of bends at the inside of the fault trace, and at its ends;
2. Measured the total and net angular deviations of fault strike along the ruptures;
3. Compiled instances of Y and T branching structures, and rupture mechanisms associated with fault-to-fault ruptures; and
4. Tabulated and analysed rupture overlap lengths.

Figure 11 below shows the approach taken by the authors to calculating the degree of deflection through internal angles in a fault rupture trace.

Figure 12 below is an example of one of the plan view maps used, for what is termed the Avezzano fault, from Abruzzo, in the Apennine region. The fault incorporates 4 faults, including the Fucino/Gioia dei Marsi fault.

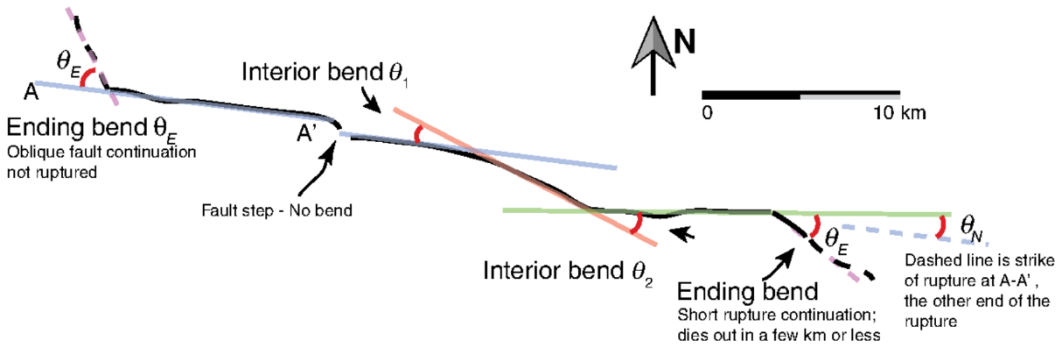

Figure 11 *Extracted from figure 1, from Biasi and Wesnousky, 2017, showing method used for quantifying angular deviations.*

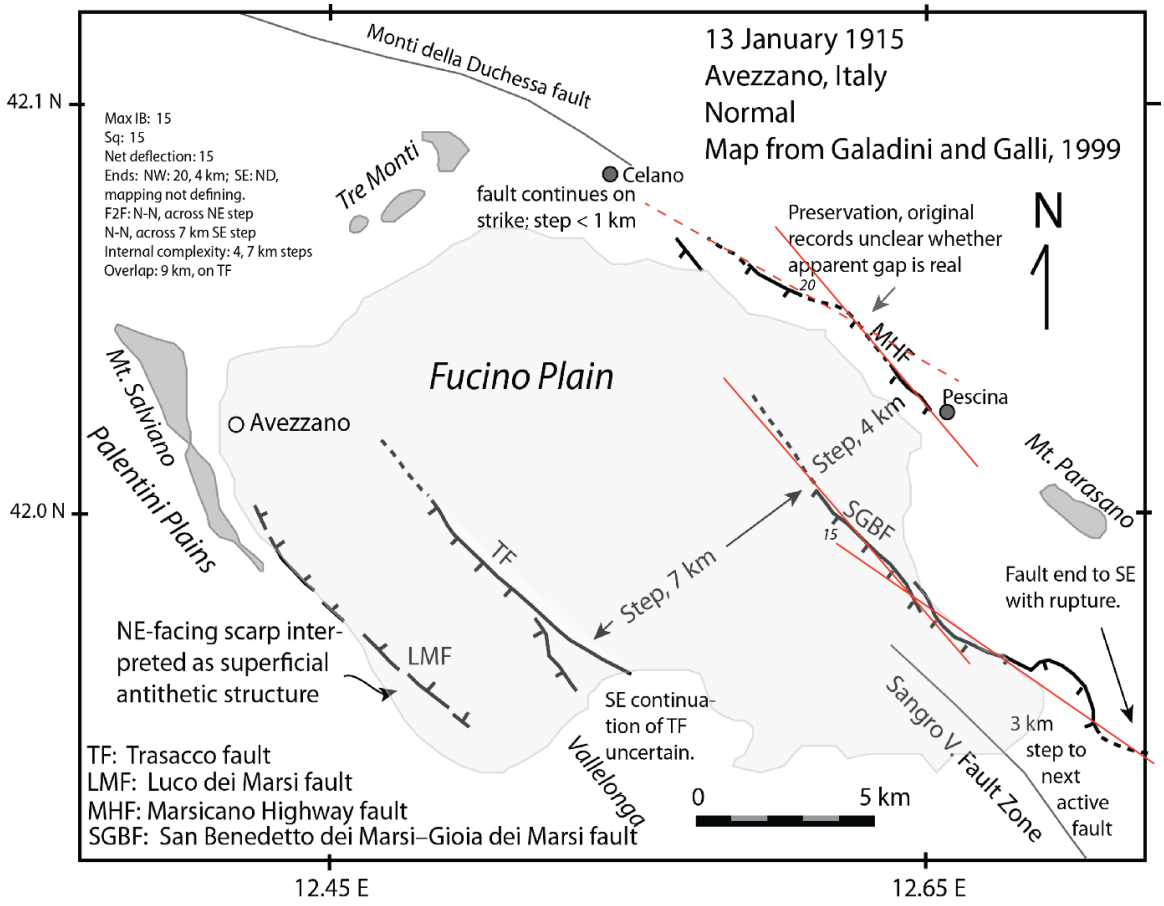

Figure 12 *Plan view for Avezzano fault region from Biasi and Wesnousky, 2017, supplementary material, showing Biasi and Wesnousky's calculation of angles relevant to assessment of TAAD, map from Galadini and Galli, 1999.*

One of the attributes of the dataset analysed by the authors was the TAAD or "squirreliness" (Total of Absolute values of Angular Deflections interior to a rupture trace, or sum of IB (Interior Bend) angles/changes in rupture direction), which they tabulated in terms of its relationship with fault length and degrees per km.

It is not clear from the 2017 paper how the authors have assigned an azimuth to the strike direction of the faults from which the degree of deflection has been calculated. In the Avezzano example, two internal deflections of 15° and 20° are recorded, making a total TAAD of 35°. The fault is measured at 40 km length, giving a deviation per km figure of 0.875 degrees/km.

The overall findings reached by Biasi and Wesnousky in relation to TAAD are illustrated in their Figure 6 (**Figure 13** below). For Dip Slip faults, TAAD/km varied between 0 degrees/km and 8 degrees/km, with a clustering of figures below 2 degrees/km. TAAD/km for Dip Slip faults was significantly higher than for Strike Slip faults. The data for Dip Slip faults were limited to 14 normal faults and 11 reverse faults. The TAAD figures within that dataset showed a tendency towards higher values of TAAD/km at shorter fault lengths.

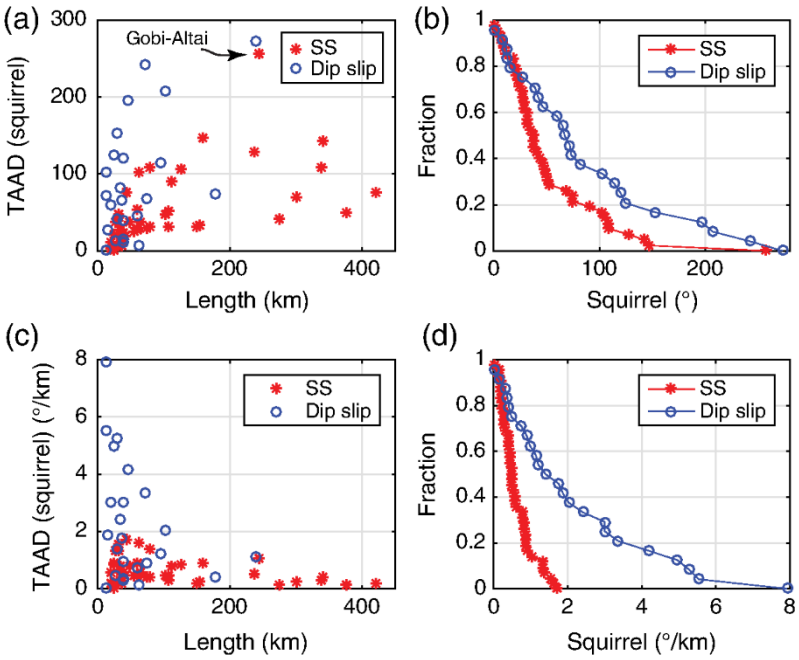

Figure 13 *Adapted from figure 6, from Biasi and Wesnousky, 2017. Total absolute angular deflection (TAAD), or squirreliness, as a (a) function of length, (b) complimentary cumulative distribution showing data fractions greater than a given TAAD, (c) TAAD interpreted as average curvature in units of degrees/km of length, and (d) complimentary cumulative distribution of curvature in units of degrees/km. Dip-slip ruptures change direction by a factor of 3 times more than strike-slip ruptures.*

The authors acknowledged that their work is based on large scale observations, and large scale features. Because of the size of the data set used, the authors nevertheless believe

that the analyses in their 2016 and 2017 papers give a useful reference point in analysing seismic hazard, to compare against models of expected fault behaviour.

2.5 Alternative models of fault growth

Walsh et al (2003) argued for the kinematic connection from initiation of segments in a fault array, based upon an interpretation from a 3-D perspective, as a preferred model to understand the growth of normal fault arrays and the development of relays between fault segments. The authors suggested this as the model to be preferred over the suggested model of incidental overlap between originally isolated faults (eg Huggins et al 1995).

In a review of previous studies, Jackson et al (2017) highlighted the "constant length" and the (more favoured in the literature) "isolated" models of fault growth (see **Figure 14** below). The alternative models produce different predictions in areas of continental extension in terms of rift development, earthquake size and occurrence times. The authors tested those models against natural examples by looking at growth strata using expansion index analysis, isochrone analysis, displacement backstripping, and relay-zone backstripping to produce detailed 3D seismic reflection models. The faults examined were the Suez Rift, the Santos Basin, offshore Brazil, and the Egersund Basin, offshore Norway. The authors' conclusion was that constant length seems more consistent with the faults seen, although with subordinate periods of relatively minor tip propagation and coeval displacement accumulation. However, it could be that isolated model growth occurs first (the data is lacking to prove that). It may be that constant length applies where there are no pre-existing structural weaknesses. The faults generally accumulated their near-final length within ~20-30% of their slip history, prior to accumulation of significant displacement.

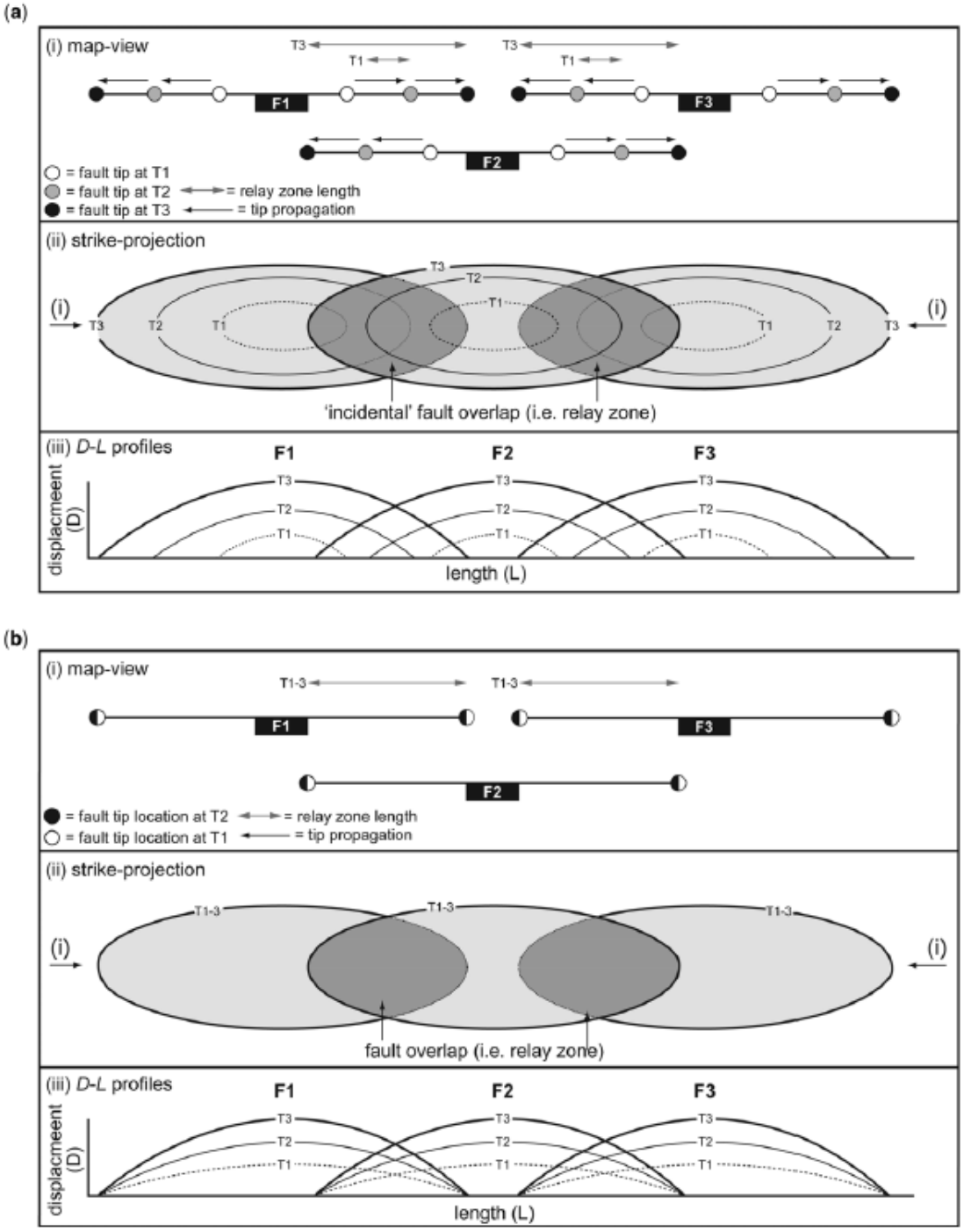

Figure 14 *Figure 1 from Jackson et al, 2017. Conceptual models for the development of blind normal fault systems: (a) the isolated fault model (Walsh & Watterson 1988; Dawers & Anders 1995; Huggins et al. 1995; Cartwright et al. 1995); and (b) the constant-length fault model (cf. Childs et al. 1995; Walsh et al. 2002, 2003; Giba et al. 2012; see also Baudon & Cartwright 2008; Jackson & Rotevatn 2013; Nicol et al. 2016). The (i) plan-view, (ii) strike-projection and (iii) displacement–length (D–L) plots are shown to illustrate the key geometrical and evolutionary aspects of each model. The black arrows in (ii) show the fault level of the map shown in (i). F1-3, faults 1–3; T1-3, time-steps 1–3. Note that, based on the final fault length (i.e. T3 in i), shape (i.e. T3 in ii) and throw distribution (i.e. T3 in iii), it is difficult to determine which growth model best describes its evolution.*

2.6 Geometrical structures in fault growth models

Among those predicting models of fault behaviour, Childs et al (1995) identified 2 types of overlaps between faults. Those are relay zones where displacement is transferred between overlapping faults, and non-relay overlaps where there is no displacement transfer. Overlaps result from the continual growth of a fault system, and are subject to destruction. The overlap comes from interference between isolated faults, or from bifurcation of a single fault, with the mode of overlap being reflected in the 3D geometry. "Synthetic overlap" can be predicted when the dips of the faults are in the same direction. If faults are "geometrically coherent" there will be a regular aggregate throw pattern, suggesting kinematic interdependence. A high footwall could be expected across the relay, with asymmetrical throw profiles. Breaching of the overlap may occur from either deflection of the tip of the overlapping fault, or a secondary link "shear" fault. There should be high bed dips in the volume between a main fault and an associated splay. A relay is more likely when the rock can accommodate strain (and therefore less likely in more competent rocks such as granite). The thickness of units at small scale may be relevant, as well as the extent of the lithological anisotropy. At larger scales crustal thickness may be a factor. The influence of primary rock anisotropy was further considered by Walsh et al, 1999. The authors found that the orientation of a fault surface and slip direction relative to the mechanical anisotropy of the faulted sequence is a dominant control on the character and internal structure of relay zones – a slip direction parallel to the layering of the primary rock is likely to inhibit the survival of relays (leading to a propensity towards hard-linkage between faults).

Marchal et al (2001) identified and termed branched structures at vertical terminations of fault planes ("Ear" structures), and en échelon structures at horizontal terminations ("Lobate" structures). The latter are rarely seen connected to the principal plane in 2D, but a connection is seen in 3D, with "deep linkage". The authors questioned whether relay fault development stops lateral fault propagation, depending upon whether there are Mode II or Mode III configurations.

The relationship between overlap between faults and separation (the relay aspect ratio) was investigated in Long and Imber (2011). The authors found a best fit power law ratio of $y=3.634x^{0.97}$, $R^2 = 0.98$ (where y = overlap and x = relay separation), with a mean aspect

ratio of 4.2, by revisiting previous measurements and using a more extensive set of data, although with an order of magnitude scatter at all scales in both overlap and separation. The paper also concentrated on possible geometric variability. The primary control on relay zone geometry is the size of the relay-bounding faults. Lithology of the host rock does not appear to be a first order control on relay geometry. The authors reference the Gupta and Scholz elasto-plastic model of fault interaction (Gupta and Sholz, 1998 and 2000), under which little interaction is expected between overlapping faults where the separation distance exceeds 15% of their total length. Where the critical stress drop contour intersects the overlapping fault tip, propagation ceases. Mechanical layering can restrict fault growth, with high relay aspect ratios resulting from thick mechanical layering. Pre-existing structures such as veins and the extent of the heterogeneity of the layers are also important factors. The extent of scatter in overlap and separation can largely be accounted for by the variation in 3D geometry within the relay zones.

Recent research has looked at modelling Coulomb Stress transfer in normal faults within a variety of gemetrical parameters, in particular looking at fault bends, breached ramps and transform faults. Hodge et al (2018) modelled an assumed receiving linking fault conforming to their definitions of those types of linkages, between two parallel source fault segments at varying degrees of overlap and underlap, and separation, using Coulomb 3.4 software. They also modelled an along-strike receiving model as an alternative to the soft or hard linkage between the source fault segments. Fault bends are hard linkages by secondary faults, at an average angle (θ) between the tips of the respective source segments of 30^{o} (and therefore also the angle between the source segment and the linkage (α)), where the tips of the source segments do not overlap the fault bend segment. Relay ramps (breached ramps) are soft linkages which become hard linkages, where the tips of the source fault segment will overlap the ramp segment, producing an angle between the source fault segments (θ) of > 90^{o}, with the linkage at a mean angle of 45^{o} (α) to the strike of the source segments. Transform faults link fault tips at θ angle of 100^{o}, with a mean α angle of ~75^{o}. The linkages are shown in figure form below (**Figure 15**, figure 2 from Hodge et al 2018).

When a single segment rupture is modelled, the authors predicted positive stress transfer when the source faults underlap (for fault bends and breached ramps), and negative

stress transfer when there is overlap. The magnitude of each increases with separation between the source segment. Fault bends represent the preferred geometry (over relay ramps) where there is underlap, where separation ≤ underlap. With underlap, where separation > underlap (where $\theta^o > 45^o$) breached ramps are the preferred geometry. A two segment rupture generally produces larger magnitude stress transfers (positive and negative).

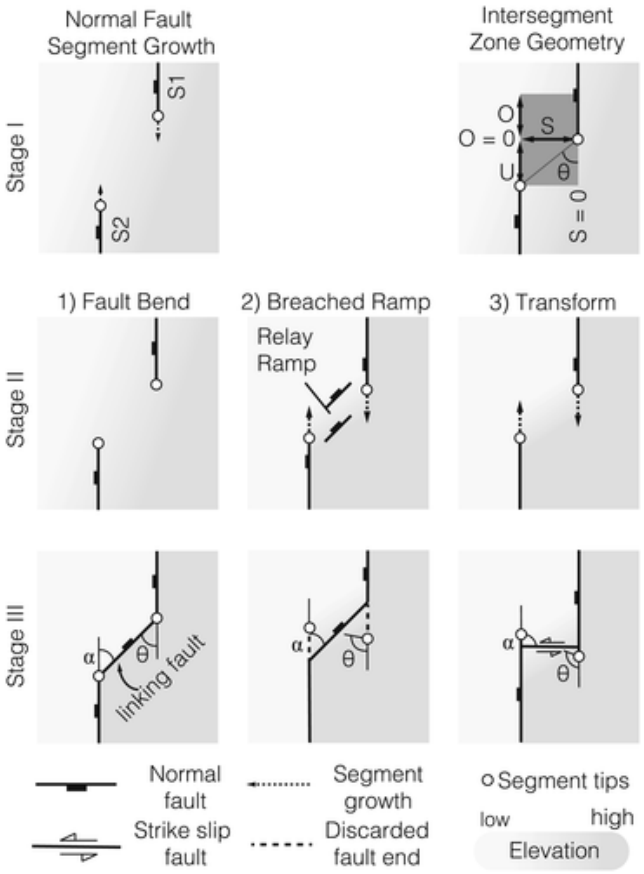

Figure 15 *Hodge et al, 2018, Figure 2. Development of end-member linking fault configurations between parallel normal fault segments: (1) fault bend, (2) breached ramp, and (3) transform fault. Stage I shows incremental growth of one or both fault segments. (1) For fault bends, segment geometry begins to be influenced by the adjacent fault segment (Stage II); the linking fault then develops with strike at angle α (equal to ϑ) to the strike of the segments (Stage III). (2) For breached ramps, displacement becomes localized in the relay ramp, then secondary faults nucleate striking at angle α to the strike of the segments (Stage II); one of the secondary faults breach across the ramp, generating the hard-linked connection (Stage III). (3) For transforms, segment growth continues without a change in strike (Stage II); geometry becomes favorable for linkage with a strike-slip transform fault striking at angle α to the strike of the segments (Stage III).*

If the alternative along strike receiving fault is also modelled, where there is a single source rupture, it generally shows a higher stress transfer, and is the preferred link except where the separation is < 2 km, where transform fault linkage is preferred. Where there

is a dual source, along strike linkage is still preferred where separation > 8 km, but fault bends are the preferred geometry where there is underlap and separation ≤ underlap. However, breached ramps are only preferred over the along strike alternative where underlap < 4 km.

Hodge et al (2018) concluded that multiple fault segment ruptures or sequences of ruptures promote the development of hard linkages (in the form of fault bends or breached relays), but a single rupture may favour along-strike propagation.

Chapter 3 Methodology

Note: In all strike and dip measurements quoted below the figures are given using the British Right Hand Rule, with the addition of the dip direction (as an example, a bedding plane dipping at 55^{o} towards an azimuth of 221^{o} will be written 311/55 SW).

3.1 Google Earth Traces

The aim is to identify traces of normal faults using data from Google Earth images (Shuttle Radar Topography Mission, SRTM data), and to analyse those traces quantitatively. The analysis involves the calculation of sinuosity values at this scale, and assessing any patterns of those values against attributes including fault length, and slip rate, to see if sinuosity values can provide an insight into models of fault growth.

This study encompasses 28 normal faults from the Apennine area of central Italy, principally from the Abruzzo and Umbria regions. Those faults are among 30 normal faults listed in a Cl_proj_2016 spreadsheet, updated in 2017 (referred to here as "the GR 2016 spreadsheet"). **Appendix A** contains data extracted from the spreadsheet, which includes the data relevant to this study. The GR 2016 spreadsheet is a compilation of data from various sources (primarily LiDAR and other fieldwork carried out by scientists from Birkbeck, Durham, and Edinburgh Universities) organised by Gerald Roberts, intended for use in modelling. It is unpublished, and was prepared using NERC (National Environmental Research Council) grants.[1] A .kml file ("the Abruzzo GE .kml file") which is understood to have been prepared alongside the GR 2016 spreadsheet using Google Earth (see Roberts, 2008), shows overall surface traces for the 30 faults, as well as other faults in the Abruzzo and Umbria region.

[1] (1). Testing Theoretical models for Earthquake Clustering using Cl-36 Cosmogenic Exposure Dating of Active Normal Faults in Central Italy, NERC Standard grant led by P. Cowie (Edinburgh), K McCaffrey (Durham), G. Roberts (Birkbeck) (2008).

(2). A LiDAR and field study of surface rupture and post-seismic slip for the 6th April 2009 L'Aquila Earthquake (M6.3) (URGENCY GRANT), NERC Urgency grant. Led by K McCaffrey, G. Roberts, P. Cowie. (2009).

(3). Earthquake hazard from 36-Cl exposure dating of elapsed time and Coulomb stress transfer. NERC Standard grant to K McCaffrey. (2012).

The data summarised in the GR 2016 spreadsheet include the throw rate for each of the 28 faults, using multiple cosmogenic Cl^{36} data from studies such as Cowie et al, 2017. This provides a throw rate averaged over 15 ka at the site of cosmogenic Cl^{36} testing. Other data in the GR 2016 spreadsheet include the length of the faults derived from **[Joanna's faults at depth???]**, and overall strike derived from an analysis of the Abruzzo GE .kml file conducted using Google Earth **[by whom?]**. Those data are used as described below, without further analysis.

The GR 2016 spreadsheet identifies the Roccacasale and Sulmona Hercules Faults separately, and assigns them different throw rates (0.79 and 0.60 mm/year respectively). However, they appear from the Abruzzo GE .kml file to be a continuation of the same fault and are identified as the same fault in that file. They are therefore treated as one fault here, the Sulmona Fault, using the lower throw rate figure. The Colle Enzano Fault identified in the GR 2016 spreadsheet as a 21km fault is not obvious on Google Earth. Although it would appear that it may be either the same as the Paganica Fault, or part of that fault and its associated traces, it is not clear to what traces the measurements refer. Therefore, that fault is omitted from this study, which is confined to 28 identifiable faults. Antithetic faults are excluded from the study.

All Google Earth imagery studied has a resolution of 30m, limiting the extent to which detail below that resolution could be identified. After attempts to pick rupture traces by eye from a variety of elevations using Google Earth, a vertical height of ~250-300 m is considered to be a reasonable compromise between detail of trace and accuracy, on fault traces which in some cases exceed 20 km in length. Lower elevations do not necessarily yield a clearer image of the fault trace, and in many cases are impractical over a fault trace of 20 km or longer. Higher elevations tend to lose some detail of sinuosity.

Picking of fault traces concentrates on following visible fault scarps in the limestone footwalls, and ignoring areas where either the fault traces are too obscured to be visible (except where extrapolation is obvious), or the trace is too faint to be identified with sufficient certainty. The consequence of this approach is that the traces picked tend to be those where greater (or more recent) movement has occurred, which in turn means that tip points, relays and other linkages between faults are less well represented. Traces in areas of high erosion, such as more mountainous regions (the Campo Felice Fault being

one example) or of comparatively recent sediment deposition (the Fucino Fault being an example, where much of the trace is covered by lake sediment) are also comparatively difficult to pick.

Where continuous picking of the rupture traces is not possible (which is in the majority of cases), individual sections are picked and separately identified.

Digital Elevation Models (DEMs) of the central Italian region in the form of ASTGTN2 files from USGS' Earth Explorer website (earthexplorer.usgs/gov) are loaded into Global Mapper GIS software[2]. The individual "picked" fault traces are loaded into the same Global Mapper file as .kml files, draped onto the DEMs, and then re-exported as .xyz files, maintaining their x, y, and z coordinates, using the UTM 33T co-ordinate system with WGS84 datum. MOVE[3] software is then used to create a flat surface for each trace or segment, creating a plane in MOVE orthogonal to the slip plane (using slip vector and dip data from the GR 2016 spreadsheet). The traces are then projected onto the flat surface in MOVE, with a view to eliminating the effects of topography on the geometry of the traces.

An example of the projection in MOVE, from the Campo Felice Fault, is shown below. The figures show respectively the original CF1C trace in MOVE (**Figure 16**), the trace and surface derived as above (**Figure 17**) and the trace projected onto the surface (**Figure 18**). In the case of the CF1C trace, the dip and slip vector azimuth in the GR 2016 spreadsheet, both taken from the "cosmo site" (cosmogenic ^{36}Cl test site), are 57→206^{o} (or a slip plane of 296/57 SW, using the nomenclature in this study). The surface is created as a plane orthogonal to the slip plane, namely 026/33 NE.

[2] Global Mapper GIS software, version 19.1 from Blue Marble Geographics
[3] MOVE™ 2017.1 modelling software from Midland Valley Exploration Limited

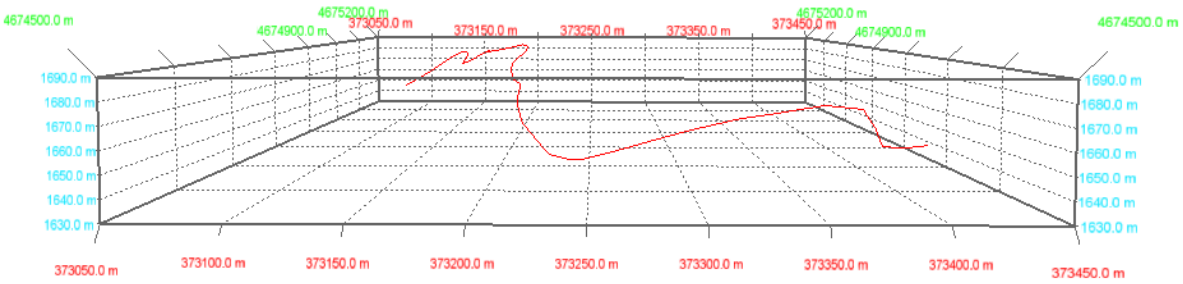

Figure 16 *CF1C trace from Campo Felice Fault (in red), shown in MOVE without projection*

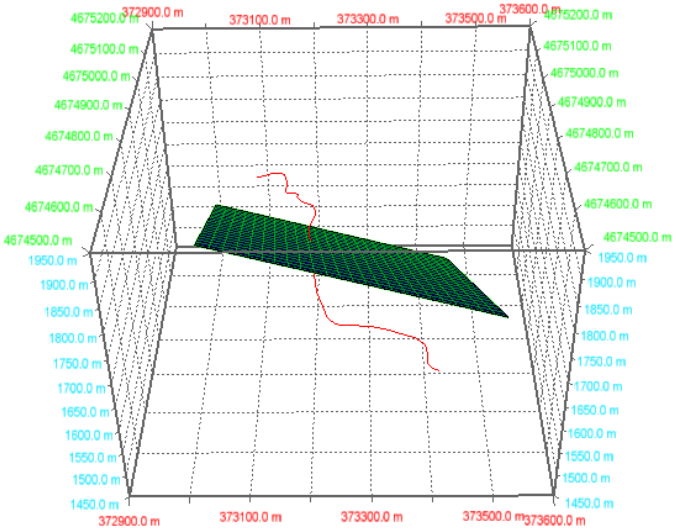

Figure 17 *CF1C trace from Campo Felice Fault (in red), and projection surface (in green/blue) at 026/33NE shown in MOVE, tilted towards view.*

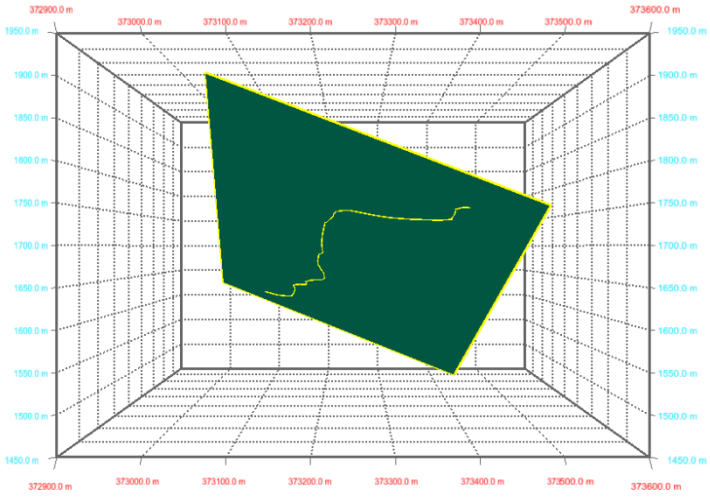

Figure 18 *CF1C trace from Campo Felice Fault projected onto projection surface (trace in yellow and projection surface in green at 026/33NE) shown in MOVE*

The straight line distance between the ends of the trace in projected line form is then measured using the MOVE measuring tool. The length of the trace is converted into a sinuosity value, by dividing the projected length of the trace by the distance between its ends in a straight line. In the case of CF1C the original length of the trace is 761.5 m, in projected form it is 789 m, and the straight line length between the ends of the projected trace is 709.8m. The sinuosity value is 789/710 = 1.111 to 3 significant figures.

As part of the analysis of observable patterns at this scale, sinuosity values are then plotted against the length of fault, projected length of fault trace, throw rate and overall strike of the fault in question (the data in each case taken from the GR 2016 spreadsheet).

Given the incomplete nature of many of the mapped traces, in order to create a sub-set of more complete traces, faults are identified where >5 km of traces in total is mapped, where those traces constitute at least ~50% of the "Fault Length" figure in the GR 2016 spreadsheet. 5 km is taken as the cut-off point, analogous to the approach of Biasi and Wesnousky, 2017, which was taken in their case to reduce the effect of solely localised structures. Here, the intent is to create a sub-set of data which more accurately represents a significant part of the faults in question, by omitting more minor (and therefore, probably less representative) results. The sinuosity values for the subset of "longer traces" are then plotted against throw rate, fault length and projected trace length. The "longer traces" are further analysed as "end" and "middle" traces, where "end" means within 1 km of the previously mapped faults (from the Abruzzo GE .kml file traces, other traces being "middle").

In order to test whether bias in the results could be imported as a result of underlying relationships between throw rate and fault length, those data (from the GR 2016 spreadsheet) are plotted against each other.

3.2 Sensitivity analysis of data for projection of Google Earth traces

The throw rate data in the GR 2016 spreadsheet are from readings taken in the field from the "cosmo" sites (sites of cosmogenic ^{36}Cl testing), which do not necessarily coincide with the location of the picked fault traces. In order to try to test whether throw rate data more specifically linked to the location of fault traces would yield differing results from the use of the GR 2016 spreadsheet figures, data from the Roberts and Michetti (2004)

paper are used, with the latitude and longitude figures given used (through ArcMap[4]) to match up with individual fault traces. Although there is some difference in the nomenclature used to identify the individual faults, the location data enable accurate identification. As an example, the Roberts and Michetti paper uses the nomenclature L'Aquila Fault, to cover elements of what in the GR 2016 spreadsheet are called the Caporciano, Barisciano and Collebrincioni Faults, which is the nomenclature adopted in this study. The sinuosity of the traces concerned is then plotted against the individual throw rates given in Roberts and Michetti's table 1.

The projection of the traces onto an inclined plane relies upon assumptions as to the applicable orientation of the fault plane. This will not be uniform throughout the length of a fault, or indeed a trace of a section of the fault. The data used in this study for the projection are the slip vector and azimuth readings taken from GR 2016 spreadsheet which are themselves averages of varying number of readings taken in the field. In some cases there are in excess of 90 measurements, although in other cases the data is more sparse. However, the readings were taken in connection with cosmogenic ^{36}Cl dating, and are not necessarily representative of the fault as a whole, or sections of the fault away from the ^{36}Cl sites.

Therefore, in order to test the sensitivity of the sinuosity figures obtained, sample traces are reassessed for sinuosity using 4 alternative data sets (each based upon data derived from the GR 2016 spreadsheet): (1) overall strike of the fault in question and measured dip from the cosmo site; (2) measured slip vector from the cosmo site and average dip of the 28 faults analysed in this study (55^{o}); (3) overall fault strike and average dip (55^{o}); and (4) the overall fault strike corrected by the average difference between overall fault strike and dip azimuth at the cosmo site (which produces a difference of 6^{o} anti-clockwise) and average dip (55^{o}). The sample traces analysed in this way are Barete A, Fiamignano, Laga D, Liri C, San Sebastiano C and Magnola A. The selection was based upon a minimum length criterion of >7km, and in the case of Fiamignano, Magnola and San Sebastiano, because those faults are also investigated using LiDAR data (see below).

[4] ArcMap™ 10.3 application, part of ArcGIS® software from ESRI

3.3 LiDAR image traces

It is expected that sinuosity at different scales would be influenced by differing factors, and in particular that there could be a difference between sinuosity relationships seen at fault scale, and those seen at a more localised scale. In order to analyse fault trace data at smaller scale using higher resolution images, terrestrial LiDAR datasets are examined from the Campo Felice, Magnola and Parasano Faults, and airborne LiDAR datasets for the Fiamignano Fault.

The LiDAR datasets for Campo Felice and Parasano were collected from previous fieldwork by M. Wilkinson and filtered subsequently to a resolution of ~25 cm. The Magnola dataset was taken with scanners placed further from the scarp as part of a training exercise, and is therefore at a lower resolution of ~35 cm. The airborne LiDAR dataset for Fiamignano was obtained through NERC, at a resolution at ~15 cm, giving a better viewing angle from overhead than terrestrial LiDAR scans.

Although the datasets are higher resolution than the Google Earth datasets (which are themselves variable in quality), problems in picking surface traces become apparent where tree shadows obscure the trace (notably with the terrestrial LiDAR datasets), and when the surface movement is lower than the resolution of the datasets. Fault tips and relays are therefore again under-represented. Because of the lower resolution of the Magnola fault dataset than for the other 3 faults it does not allow picking at a scale to produce segments of ~50-60 m. However, in general, the higher resolution of the data means that a more complete trace of the fault can be picked.

Using Cloud Compare software[5], and from an altitude of ~50m the Magnola traces are picked in sections of ~110m. The Campo Felice, Fiamignano and Parasano traces are picked from an altitude of ~30m in sections of ~50-60 m. Cloud Compare is then used to fit a plane to the dip surface of each individual trace, which in turn is then used in MOVE to create a plane perpendicular to that plane, onto which the traces are then projected (as with the Google Earth-derived traces). The projected traces are analysed for sinuosity using the MOVE measuring tool to derive the straight line distance between the ends of the traces, and dividing the projected length by the straight line figure.

[5] Cloud Compare Open Source 3D Point Cloud and mesh processing software from cloudcompare.org

The sinuosity values for the traces are plotted against the fault traces (along fault from NW to SE) to assess whether there is any pattern to the change in sinuosity along the fault.

3.4 Comparison of results from projected traces with non-projected traces

Sinuosity values from the study using projection of the traces against a plane are also compared with trace sinuosity values without projection, using MOVE's measuring tool to obtain a measured map view straight line distance. This produces a further set of sinuosity values based solely on map view measurements.

3.5 Identification of fracture patterns

Fracture patterns from the area are reviewed, with the aim of seeking to identify localised, small scale features which might have a bearing upon sinuosity seen at the level of >100 m length traces.

Cropped sections of the LiDAR datasets for the Campo Felice, Fiamignano and Parasano faults each incorporating sections of the fault scarp and the footwall above the fault scarp are loaded into the VRGS software[6] package, and triangulated. The VRGS software allows point clouds to be analysed for co-planar features, which in this case can be used to identify possible fractures (as well as more prominent features such as the fault scarp itself). It is hoped to establish fracture patterns by using the co-planarity tool to identify common patterns within the footwall above the fault scarp, and within the scarp itself. Filters are applied to the co-planarity results to reduce the scope of the output, and concentrate on more significant results. The co-planar sections identified are then picked at random from the fault scarp and footwall areas, and readings taken of dip and dip azimuth from ~75 locations in the case of each fault, using the interpretation, fractures mode, three points dip azimuth tool in VRGS (see **Figure 19** below).

[6] VRGS version 2.39, VRGS Viewer, Virtual Reality Geological Studio 3D data visualisation and interpretation software tool

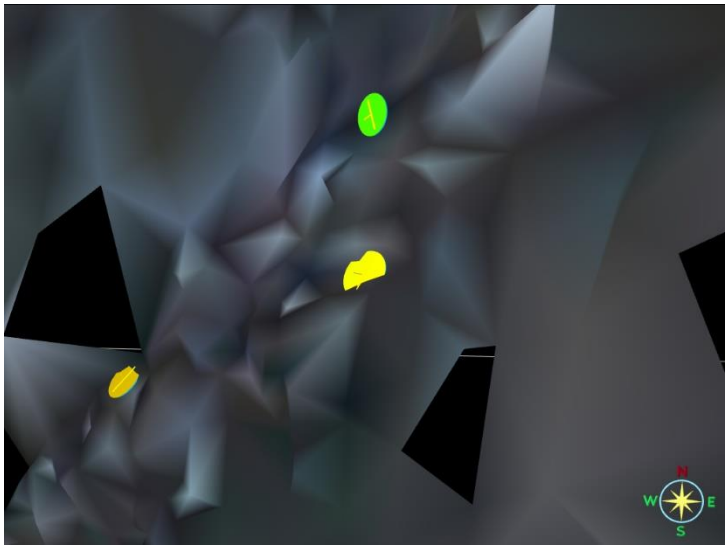

Figure 19 *Example of picked co-planar locations on a triangulated point cloud from a section of the Fiamignano fault footwall, using three points dip azimuth tool in VRGS, yellow example in centre of figure shows fracture dipping 38°→290°*

The results are plotted in contoured stereonet form.

Limited measurements were also taken in the field of bedding and fracture planes from the Fiamignano, Magnola and San Sebastiano faults during a reconnaissance visit to Italy in July 2017. Those measurements are also plotted in contoured stereonet form.

3.6 Identification of local topographical features at small scale

Where significant variation in sinuosity values is shown, individual LiDAR traces picked using Cloud Compare are exported to Google Earth by saving the Vertex Attributes of the .dxf files (from Cloud Compare, in non-projected form) in MOVE as .csv files, restoring true coordinates in Excel, creating feature sets from the resulting .xlsx files in Arc Catalog[7], adding Projected Coordinate System (UTM/WSG1984/Northern Hemisphere/Europe/Zone33N), saving as .shp feature sets (also in Arc Catalog), creating .lyr files, then exporting the result from Arc Catalog to Google Earth as .kml files using Arc Catalog's .lyr to .kml Conversion tool. This process enables the small scale variations in sinuosity values identified from the LiDAR datasets to be seen in the context of the Google Earth images for those faults.

[7] Arc Catalog geographic information organisation and management application, part of ArcGIS® from ESRI

3.7 Coulomb Stress modelling

At fault scale, a potential source of deviations in the fault traces, and thus in sinuosity values, is the effect of stress transfer from neighbouring active faults, or between active and static segments of a fault. Coulomb Stress modelling allows the transfer of stress to be modelled as to its likely magnitude, its location, and its changes over time as slip develops, on alternative models of fault growth.

Coulomb stress change ($\Delta\sigma c$) is the change in static stress state caused by slip on a source fault, resolved onto a receiver fault. A source fault in this sense is an active fault, whose slippage is modelled, the receiving fault modelled as static. The change is defined by the following equation:

$$\Delta\sigma c = \Delta\tau s - \mu' \Delta\sigma n,$$

where $\Delta\tau s$ is the shear stress change (positive in the slip direction), $\Delta\sigma n$ is the normal stress change (negative when the fault is unclamped), and μ is the static friction coefficient. μ' reflects the impact of pore pressure, ρ, where $\mu' = \mu (1 - \beta)$, and $\beta = \rho/\sigma n$.

Using the Coulomb Stress modelling software downloaded from the USGS website, Coulomb 3.3.01 (https://earthquake.usgs.gov/research/software/coulomb/)[8] a number of models of fault patterns are run using MATLAB®[9], to identify the likely stress changes on a selection of receiver faults from neighbouring source faults exhibiting either constant length or isolated fault behaviour. Although the Coulomb Stress model does not include dynamic processes, and is essentially a static model, it has been used widely to model earthquake aftershocks, and as an aid in forecasting earthquake sequences (eg Wedmore et al, 2017).

The World Stress Map[10] is used as a source for data from earthquake events in the Abruzzo region, to identify regional stresses used in the models. A sample of 7 such events centred around the city of L'Aquila, Abruzzo, produces an average regional S1 stress of

[8] Coulomb 3.3 Graphic-Rich Deformation and Stress-Change Software for Earthquake, Tectonic,and Volcano Research and Teaching

[9] MATLAB R2015b, from The MathWorks, Inc.

[10] World Stress Map compilation of information maintained at the Helmholz Centre Potsdam GFZ, downloaded from http://www.world-stress-map.org/download/

~330/70, S2 of ~140/17, and S3 of ~235/05. Those figures are used for regional stress. A DEM showing one of the locations used (Pondrelli) is at **Figure 20** below.

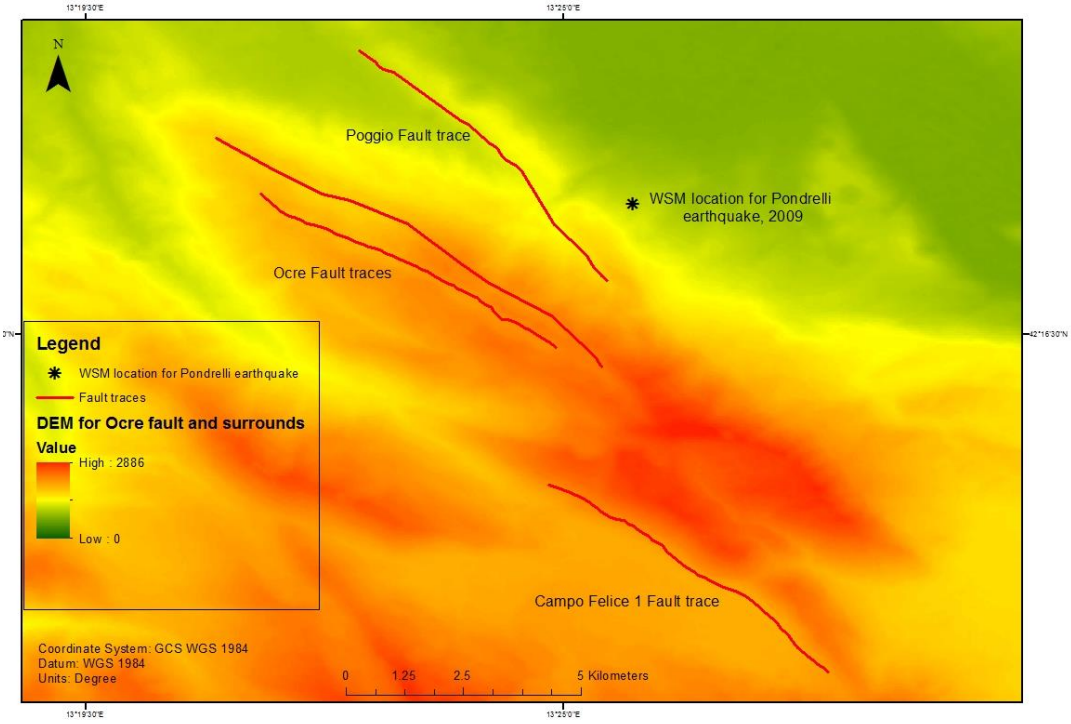

Figure 20 *DEM showing one of the focal mechanism locations from the World Stress Map used to calculate approximate regional principal stress axes, here Pondrelli, Ocre, Abruzzo, location of Normal Fault 5.3 Mw earthquake in April 2009, at 15 km depth, S1 315/57, S2 135/33, S3 004/01. Location of neighbouring traces from Abruzzo GE .kml file shown in red.*

The nomenclature S1, S2 and S3 refers to principal stress axes (where S1 is the axis of greatest stress, and S3 the axis of least stress), shown in normal faulting in **Figure 21** below, taken from the WSM Scientific Technical Report STR 16-01. The figure also shows predominantly dip-slip faulting with a strike slip component.

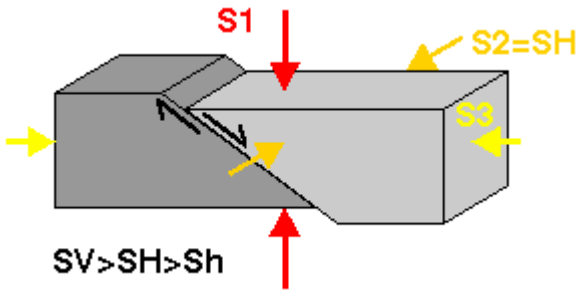

NF: Normal faulting

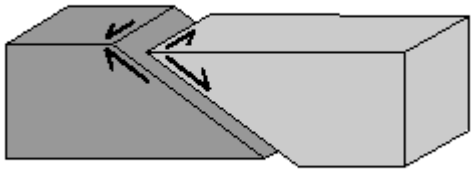

NS: Predominantly normal faulting with strike-slip component

Figure 21 *Diagrams from the WSM Scientific Technical Report STR 16-01 illustrating orientation of principal stress axes in normal faulting, and with component of strike-slip.*

At whole fault scale, a potential source of deviations in the fault traces, and thus in sinuosity values, is the effect of stress transfer from neighbouring active faults, or between active and static segments of a fault. The aim here is to use a modelling approach to assess the likely magnitude of stress transfer, its location, and its changes over time as slip develops, on alternative models of fault growth, on a selection of receiver faults analysed using the methods reported in Chapter 4 below.

In order to set up models for the faults chosen, it is necessary to set up parameters, including the principal stress axes. Surface stress for S1 is taken as being 175 bar (17.5 MPa) over a I km depth, making an allowance from a typical dry continental rock vertical stress gradient of 26.5 MPa per km (Fossen, 2016, page 87) (100 bar = 10 MPa) due to the known presence of fluids in the limestone rocks. This is approximated to 17.5 bar (1.75 MPa) per km (one tenth of the S1 figure) for S2. The vertical stress gradient of 175 bar (17.5 MPa) per km is only applied in the case of S1.

A default Poisson's ratio (v) of 0.25 is applied, as in other Coulomb Stress studies (eg Hodge et al, 2018), a representative value for limestone of 800,000 bar (80 GPa) for the Young's modulus (E) (Fossen, 2016, Table 6.1, page 104), and 0.4 coefficient of effective

friction (μ'), appropriate for large continental faults (allowing for the effect of pore pressure from a dry Byerlees' law value of 0.65).

The average figures for slip azimuth derived from the GR 2016 spreadsheet show a difference of 6° anticlockwise between the slip azimuth and dip direction across the faults. Recognising the small element of shear stress involved, lateral slip is modelled as a tenth of the amount of dip slip. The 6° anticlockwise difference suggests the application of left lateral slip. In each case normal faulting is modelled, with a 10% component of strike-slip (as in **Figure 22** below).

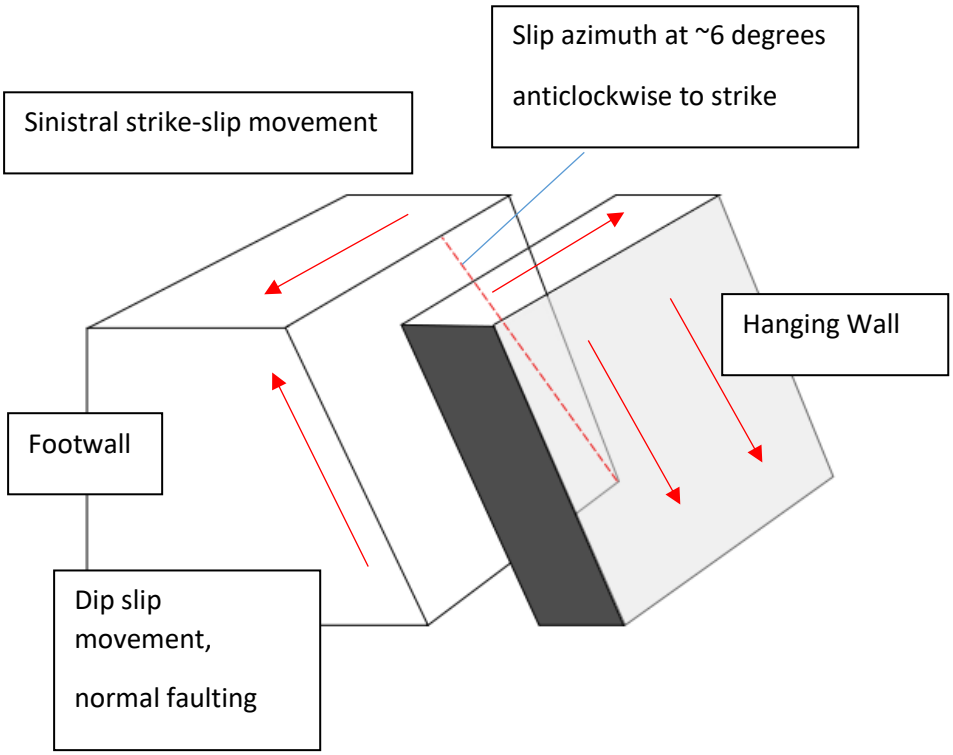

Figure 22 *Model of strike slip element modelled on normal faulting.*

A seismogenic depth of 10 km is used. The calculation depth used in all cases is 5 km. All faults are modelled as planar features.

The approximate perpendicular distances between faults used in the models are taken from Google Earth measurements.

The models are computed at 3 ka intervals over a time period of 15 ka. In the constant length models the fault is assumed to have reached its final length throughout, with slip

increasing linearly in stages. In the variable length models, the fault is assumed to have reached approximately half its final length at 3 ka, and then to have grown in length proportionately over the following 12 ka at 3 ka intervals to its final length at 15 ka, with slip increasing linearly at the same time. In order to reduce complexities in modelling (and in the absence of data as to the spatial evolution of the respective faults), in the majority of cases a fixed point has been used for the starting point of the source faults at the NW end of the fault traces, and the varying length adjusted. In instances where the source fault is significantly longer than the receiving fault, a further alternative iteration has been run which assumes the source fault grows along strike in both directions (generally NW and SE) from a central point.

Chapter 4 Results/Analysis – Google Earth and LiDAR

4.1 Google Earth Trace analysis

Data on all traces from the 28 faults mapped in the Apennine region obtained using the Google Earth method described at 3.1 above are set out in detail in **Appendix B.** The data include identification of locations, fault length, throw rate, and fault strike extracted from the GR 2016 spreadsheet, and calculations made in respect of the traces mapped (including azimuth, projected length of trace, and sinuosity).

4.1.1 All projected traces

The spread of sinuosity values over all the projected traces (85 in total from 28 faults) is shown in the histogram at **Figure 23** below. The mean sinuosity value is 1.079.

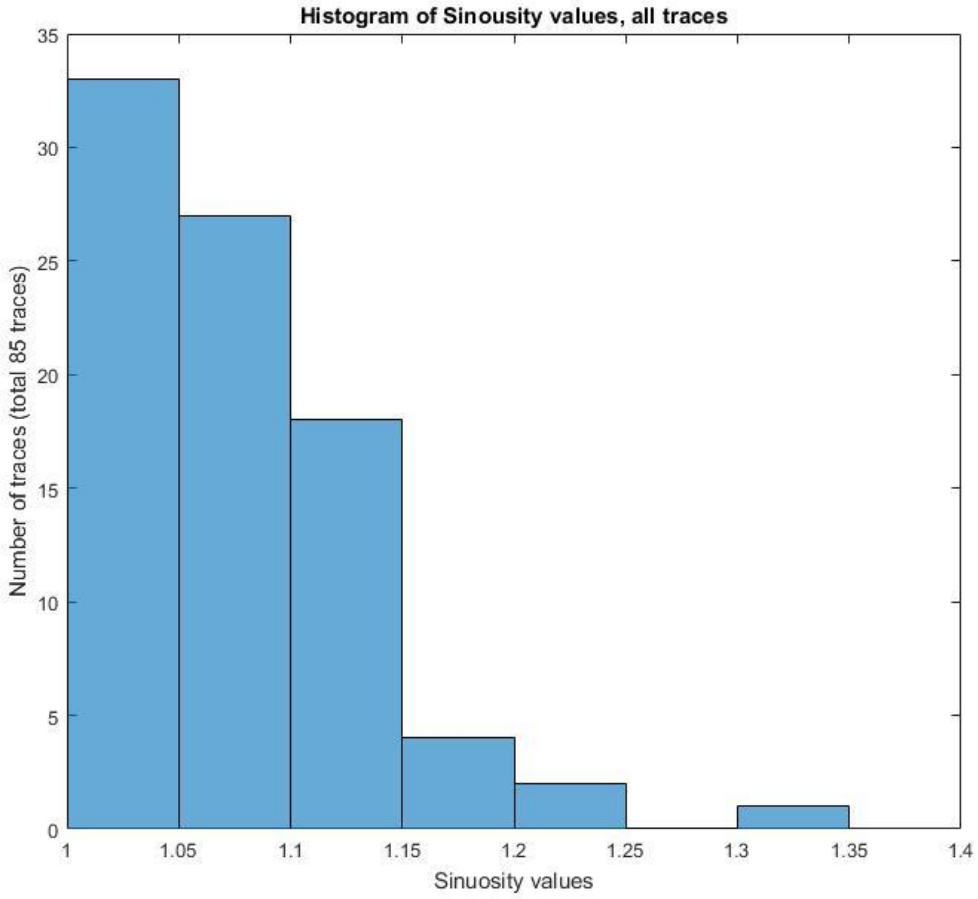

Figure 23 *Histogram showing spread of sinuosity values over all projected traces taken from Google Earth.*

Figures 24, 26 and 27 below show the relationships between sinuosity for all projected traces, and (respectively) fault length, projected trace length, and throw rate. The R^2

(coefficient of determination) value in relation to fault length (0.0027) (R, coefficient of multiple correlation = 0.05) indicates that the very slight decrease in sinuosity seen with fault length is almost certainly statistically irrelevant. The variability in sinuosity values decreases with length, with fewer values above 1.100 and below 1.025, which may suggest that more variable surfaces converge on smoother surfaces as faults grow or accumulate slip.

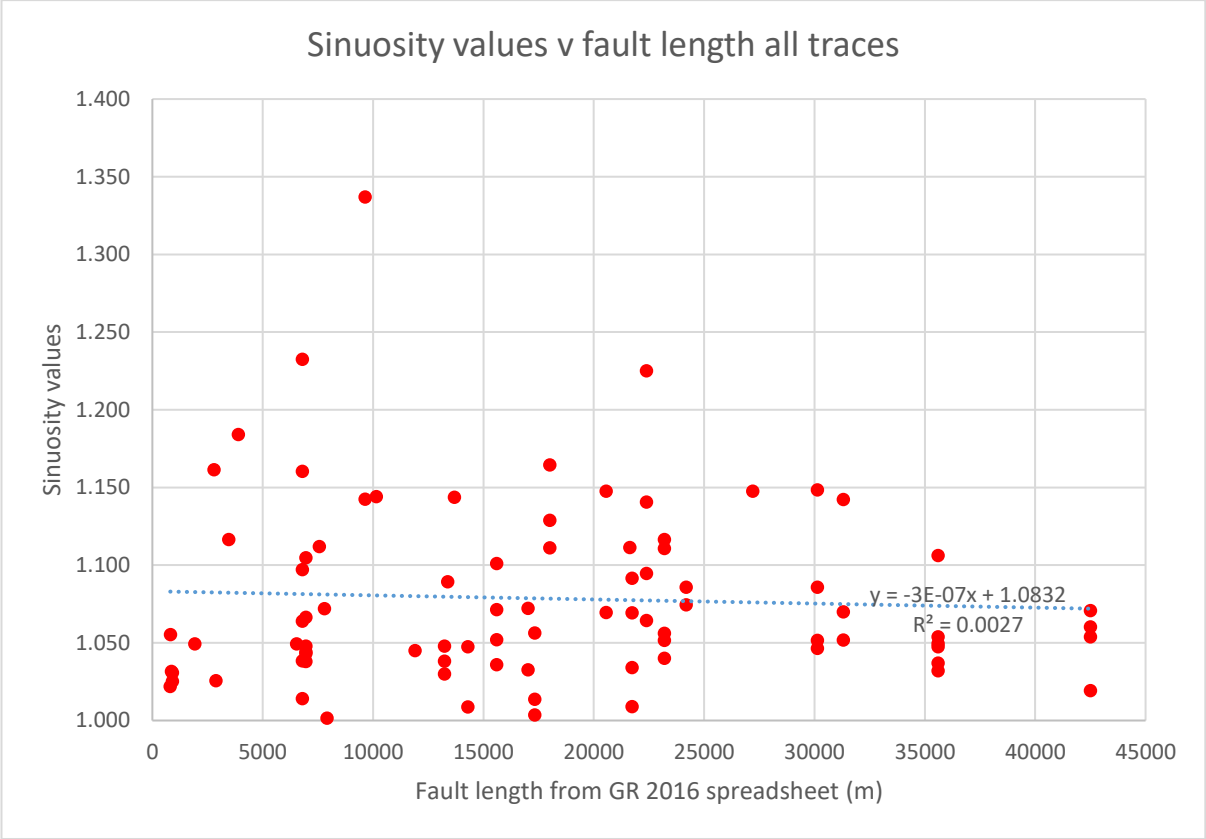

Figure 24 *Relationship between sinuosity values and fault length (from GR 2016 spreadsheet), all traces.*

The same figure, with standard deviation shown (**Figure 25** below) reinforces the trend towards less variability as the fault length increases. Standard deviation figures decrease as fault lengths increase. Standard deviation figures of 0.058 and 0.081 for the shorter faults (calculated for the faults within the length ranges of 0-5000 m and 5000-10000 m respectively) decrease to 0.032 and 0.019 for longer faults (30000-40000 m and >40000 m respectively).

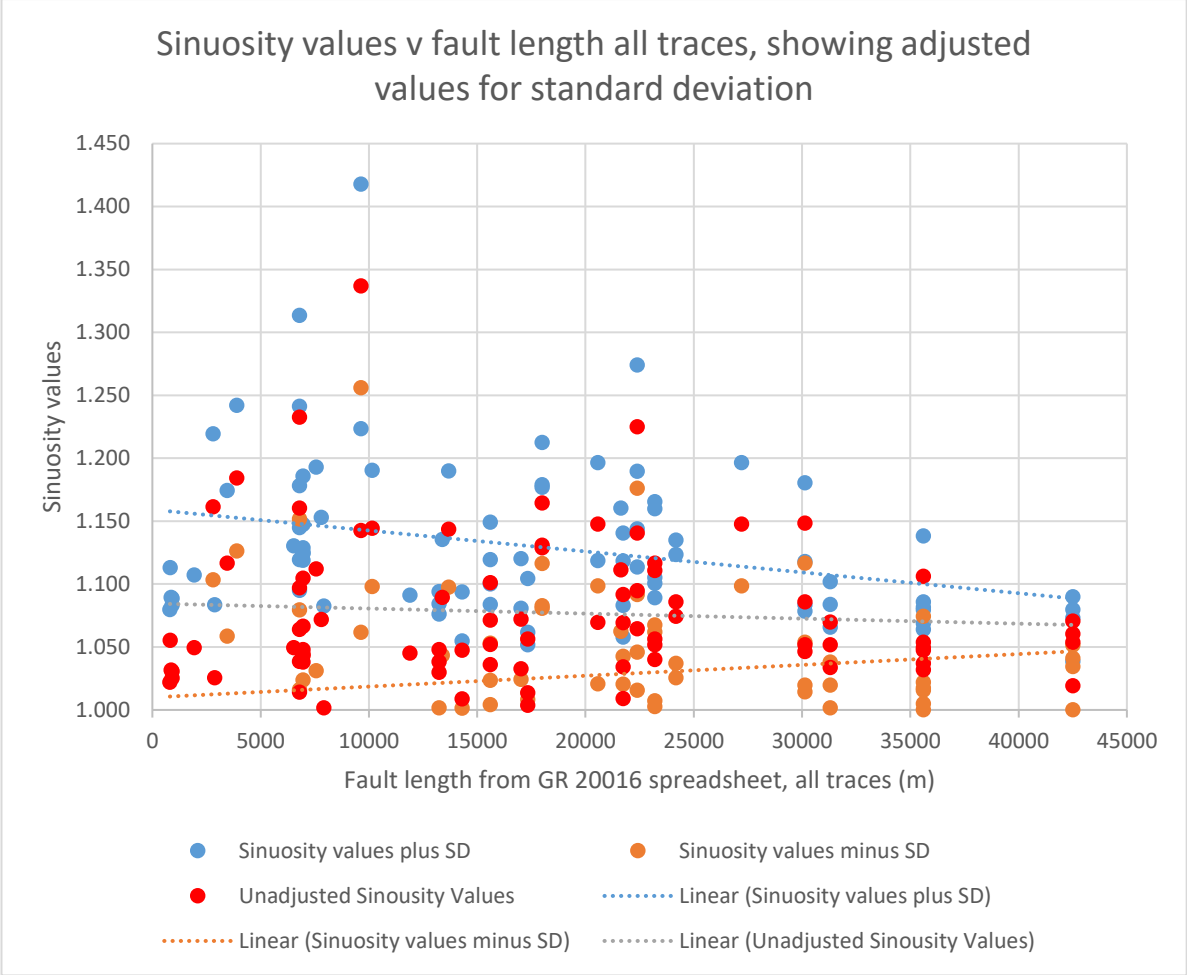

Figure 25 *Relationship between sinuosity values and fault length (from GR 2016 spreadsheet), all traces, with standard deviation calculated in 5000m intervals, until 20000m, thereafter at 10000m intervals, original sinuosity values shown in red.*

The R^2 value in relation to trace length (0.0356) (R = 0.19) (**Figure 26**) may suggest some weak correlation between moderately increasing sinuosity with increasing projected trace length. The data is less abundant as trace length increases. Sinuosity increases with throw rate (**Figure 27**), but the R^2 value (0.0248) (R = 0.16) also suggests only weak statistical correlation.

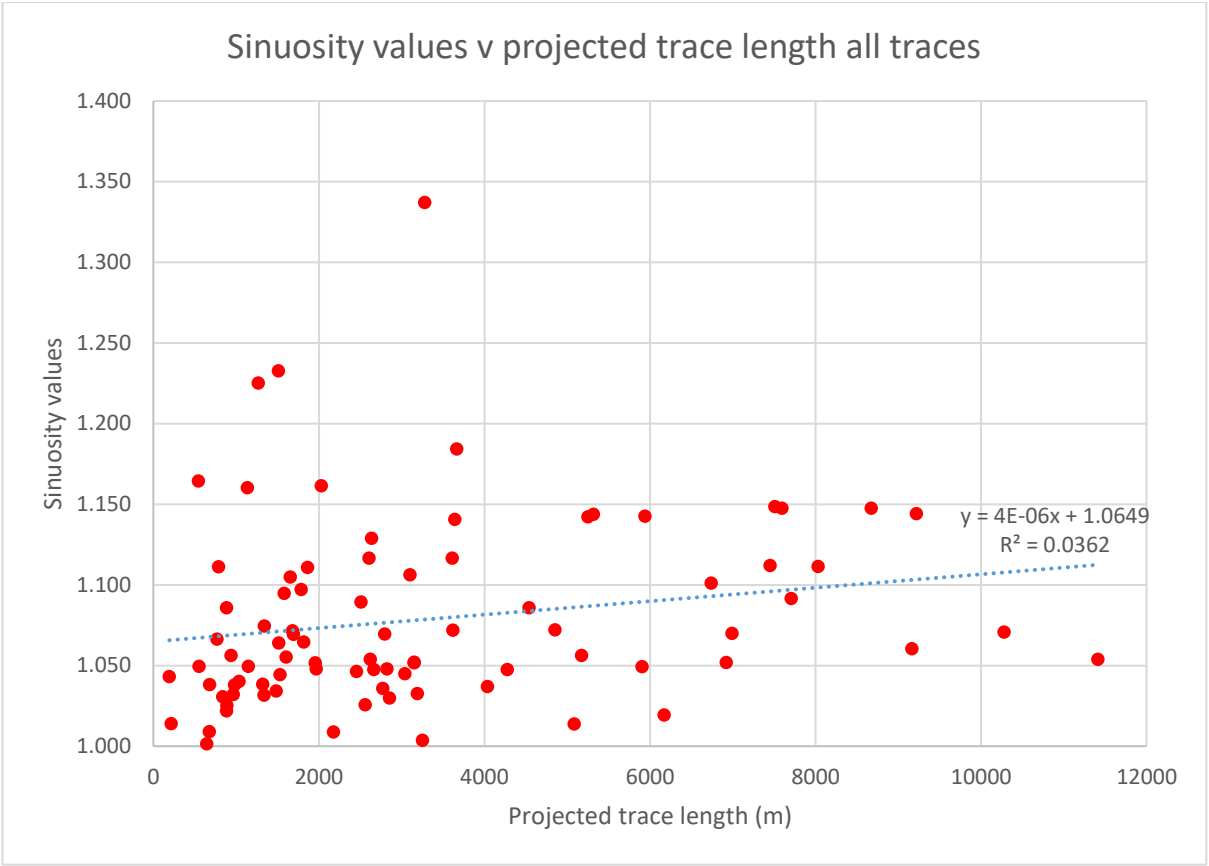

Figure 26 *Relationship between sinuosity values and projected trace length, all traces.*

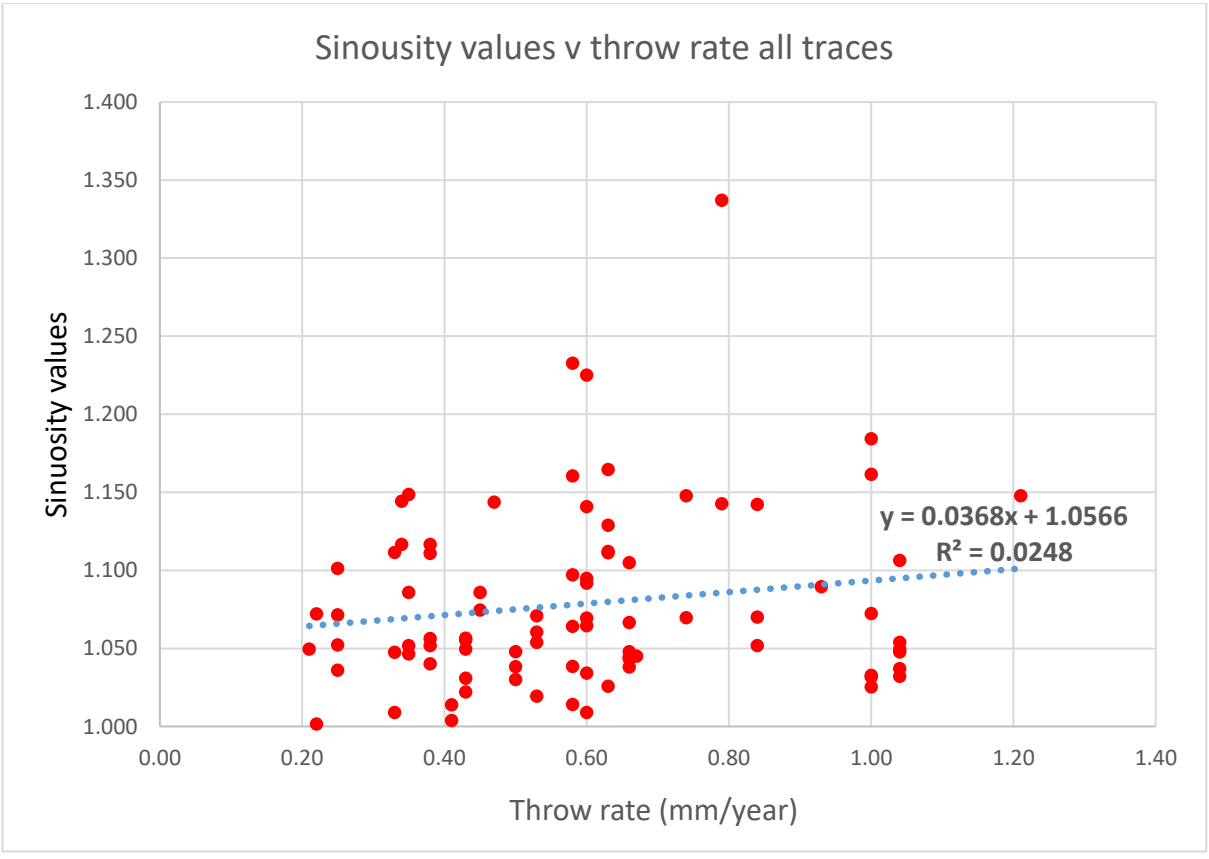

Figure 27 *Relationship between sinuosity values and throw rate, all traces.*

There is, however, an observable relationship between sinuosity values and overall fault strike. **Figure 28** below demonstrates a relationship between sinuosity and strike which shows a decline in sinuosity values as strike approaches 180°. The R^2 value is 0.0635 (R = 0.25). The strikes are plotted as 0-180° (which, given the common dip to the SW throughout, means a strike of 180-360° using the British Right Hand Rule). The average strike of the faults studied is 311° (or 131° in this figure). The sinuosity values clustered around 131° and with a strike clockwise from there are among the lowest. The values anticlockwise are the most widely spread, and include most of the higher values. The distorting effect of two faults (Tre Monti and Magnola) is discussed further below.

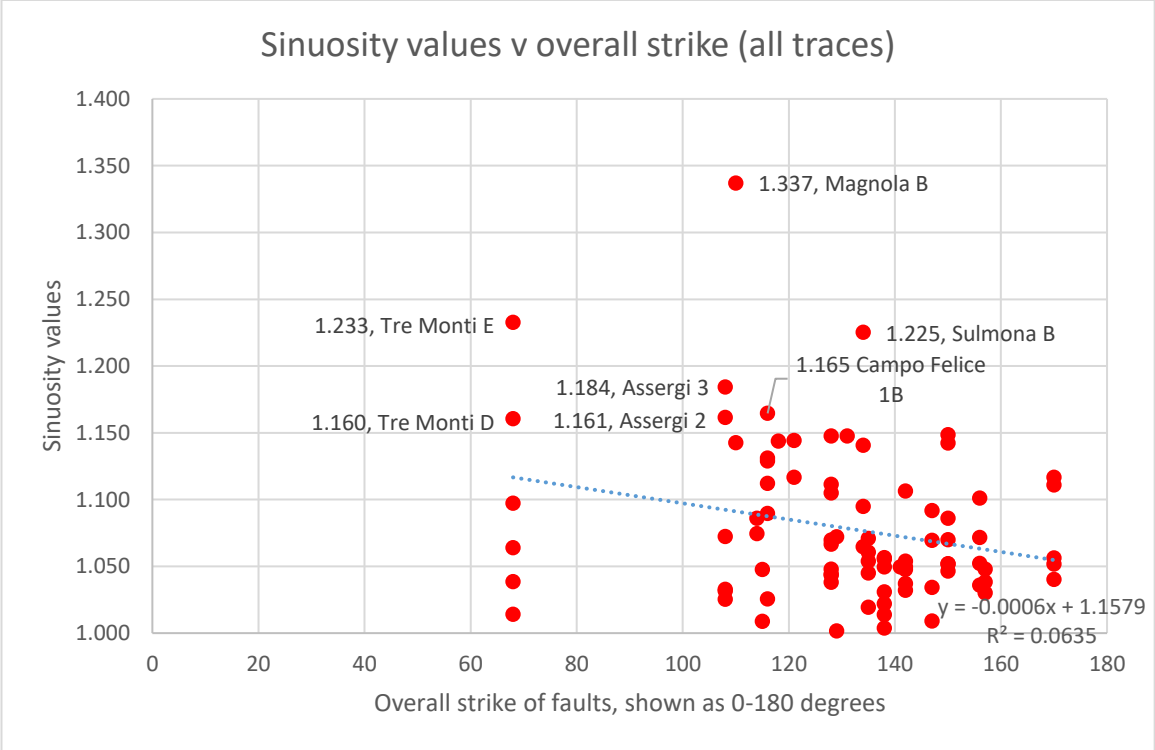

Figure 28 *Relationship between throw rate and overall strike of the faults, all traces. Strike shown as 0-180°, sinuosity values for 6 highest values labelled*

When the throw rate figures in the GR 2016 spreadsheet are plotted against the recorded figures for fault length, there is a marginal increase in throw rate in line with increasing fault length (**Figure 29** below). However, the R^2 value is less than 0.1 (at 0.0255, R = 0.16). Therefore, there seems to be little statistical significance in that relationship.

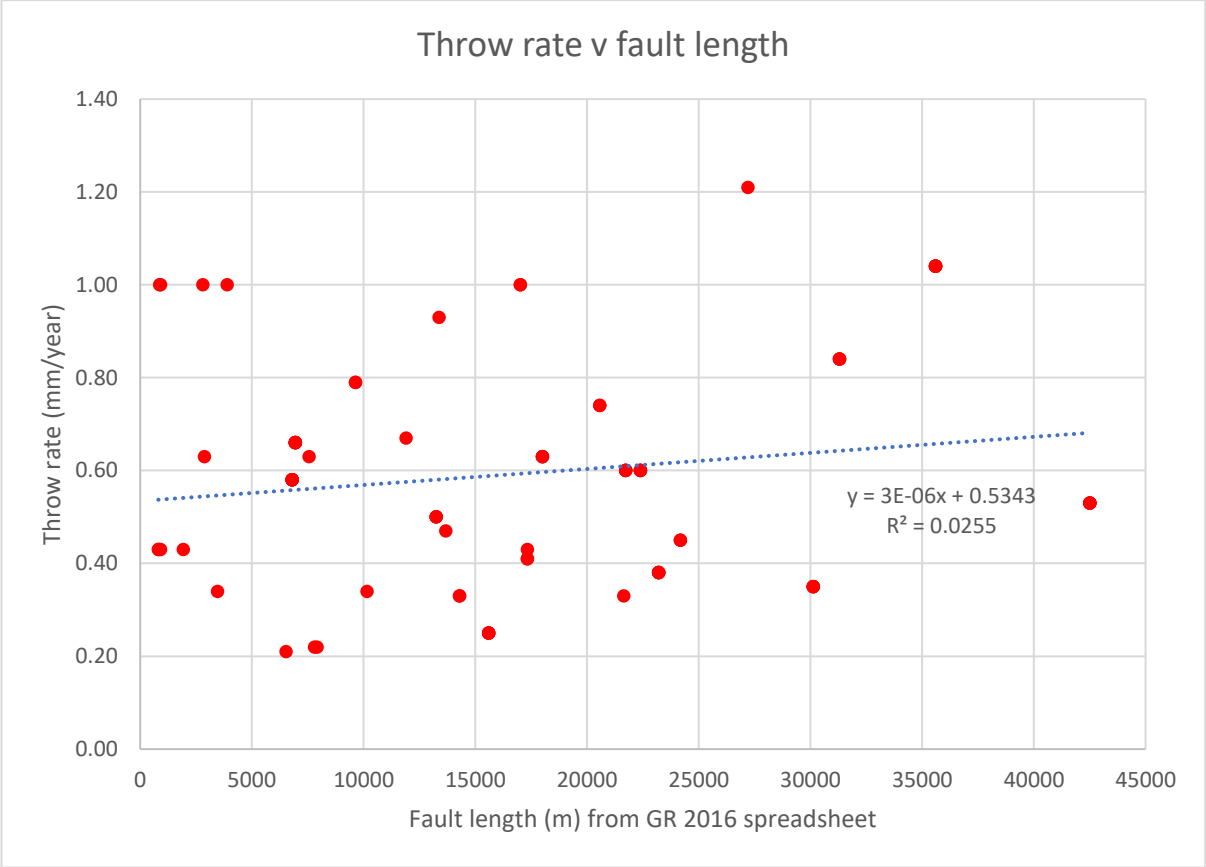

Figure 29 *Relationship between throw rate and fault length figures from the GR 2016 spreadsheet.*

4.1.2 Longer traces

The "longer traces" mapped are those which in total exceed 5 km for the fault in question, and where the extent of the traces mapped exceeds 50% of the "fault length at depth" figure taken from the GR 2016 spreadsheet. The total number of traces involved is 34, covering 11 faults. The traces are further classified by whether they are "end" traces (<1 km of the fault tip at surface) (14 traces) or "middle" traces (>1 km of the fault tip at surface) (20 traces). The data for those traces is set out in **Appendix C.** The sinuosity values are the same as for "all traces", above.

The histogram at **Figure 30** below shows the spread of sinuosity values for the longer traces. The mean value is 1.076.

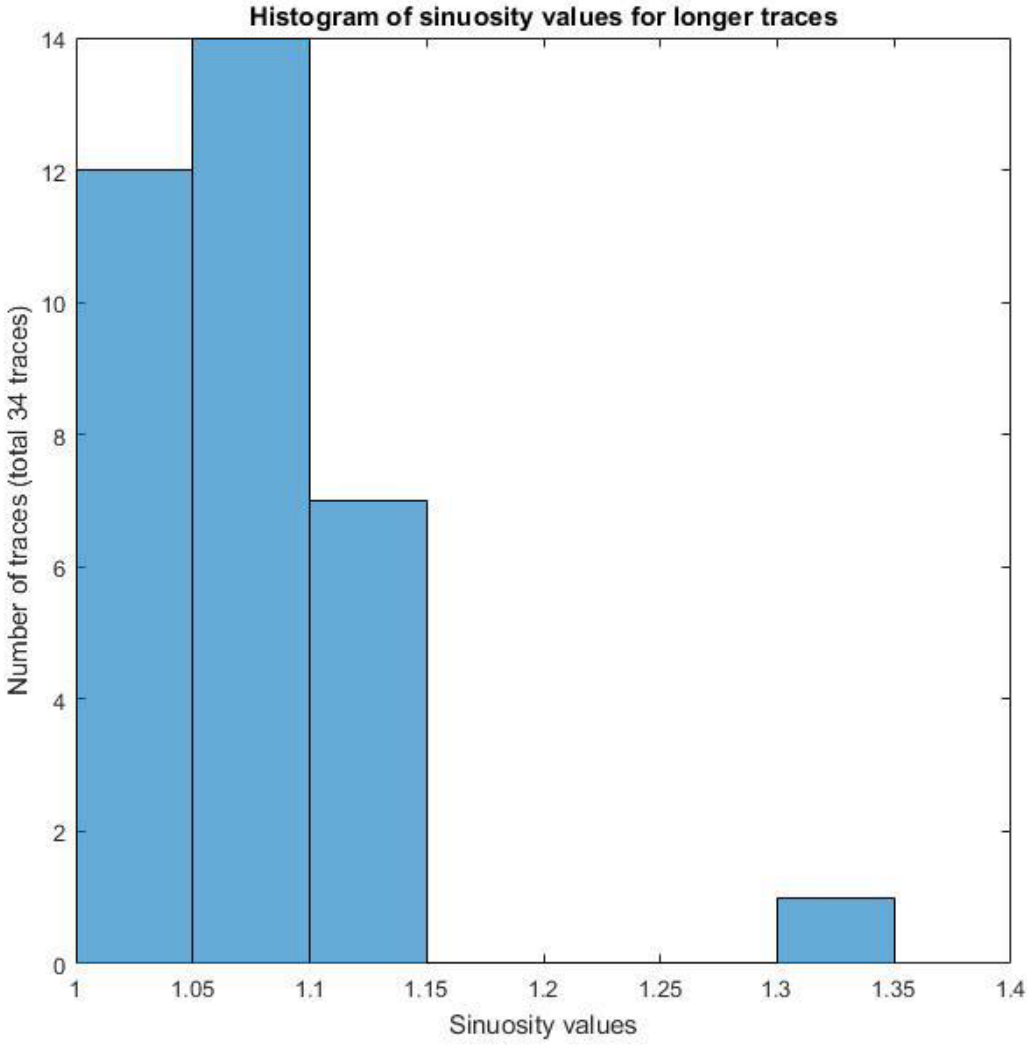

Figure 30 *Histogram showing spread of sinuosity values for longer projected traces taken from Google Earth.*

As that figure and **Figure 31** below demonstrate, there is a general range of sinuosity values for all faults where longer traces are identified, between ~1.05 and ~1.15, which does not vary appreciably by fault length. The longer traces results remove some of the more variable results seen for all traces, with the removal of some of the shortest traces from the results. The exception to this smoothing out of the results is the Magnola Fault, at a sinuosity value of ~1.20 (more than double the "mean" value of the other longer faults). The vales for Magnola produce a distorting effect, showing a decline in sinuosity with increasing fault length.

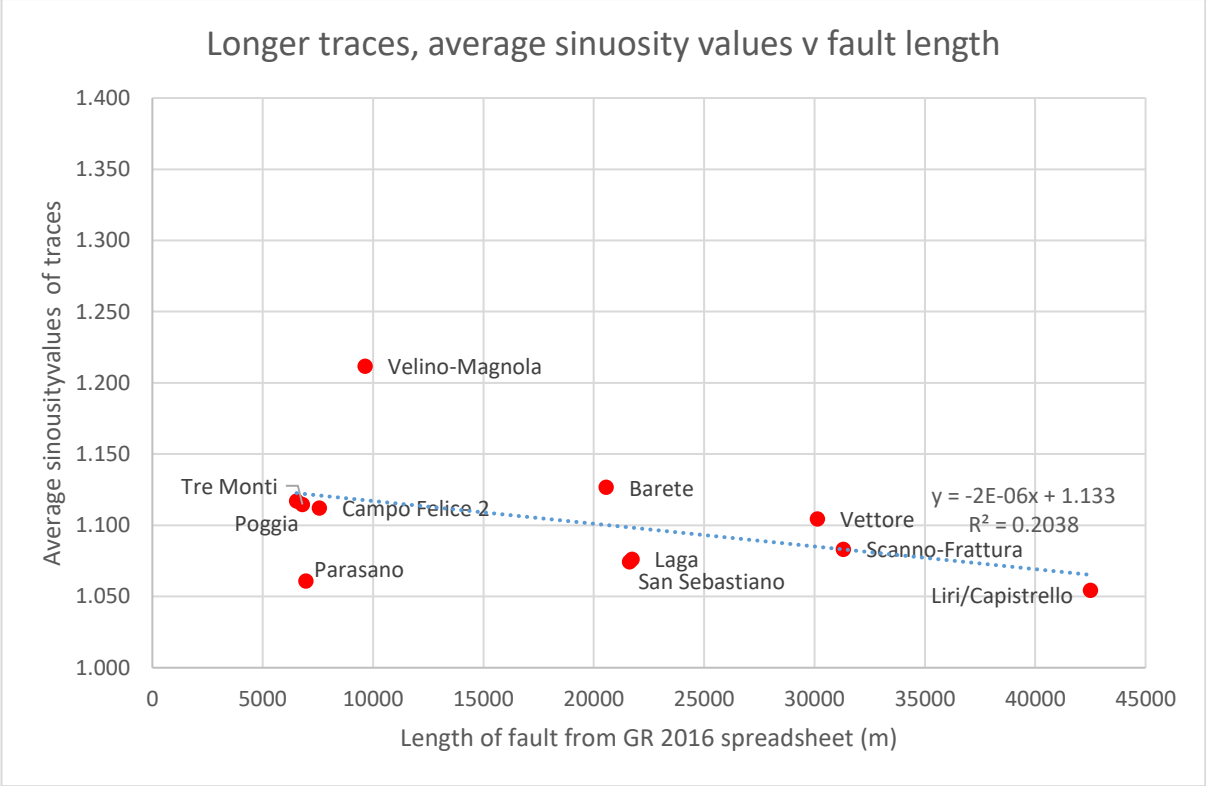

Figure 31 *Average sinuosity values of longer traces compared to fault length*

A comparison of the sinuosity of "end" and "middle" traces show that the average sinuosity values of the middle traces are very slightly less than that of the end traces (although the difference is small) (**Figure 32**). The average sinuosity value for "end" traces is 1.085, and for "middle" traces it is 1.082**.** The figure also highlights the outlying sinuosity values for the Magnola Fault traces (the two traces involved are both "end" traces), as well as the much greater spread of sinuosity values for the Tre Monti Fault (which has both the greatest and the smallest of sinuosity values for middle traces). That can also be seen from **Figure 33,** where sinuosity values are compared to throw rate.

Omitting the Magnola traces from the figures for "end" traces, the average sinuosity value for "end" traces would be 1.059 (with "middle" traces showing significantly higher sinuosity values than "end" traces). This suggests less sinuosity towards fault tips than in the centre of faults, but the population is not large, with only 12 "end" traces once the Magnola results are omitted.

There is a marginal increase in sinuosity values with throw rate, but an R^2 figure of 0.0675 (R = 0.26) suggests there is only weak statistical correlation. There is a small increase in

sinuosity values with increasing trace length (figure not shown), but an R^2 value of 0.0134 (R = 0.12) suggests this is not likely to be statistically relevant.

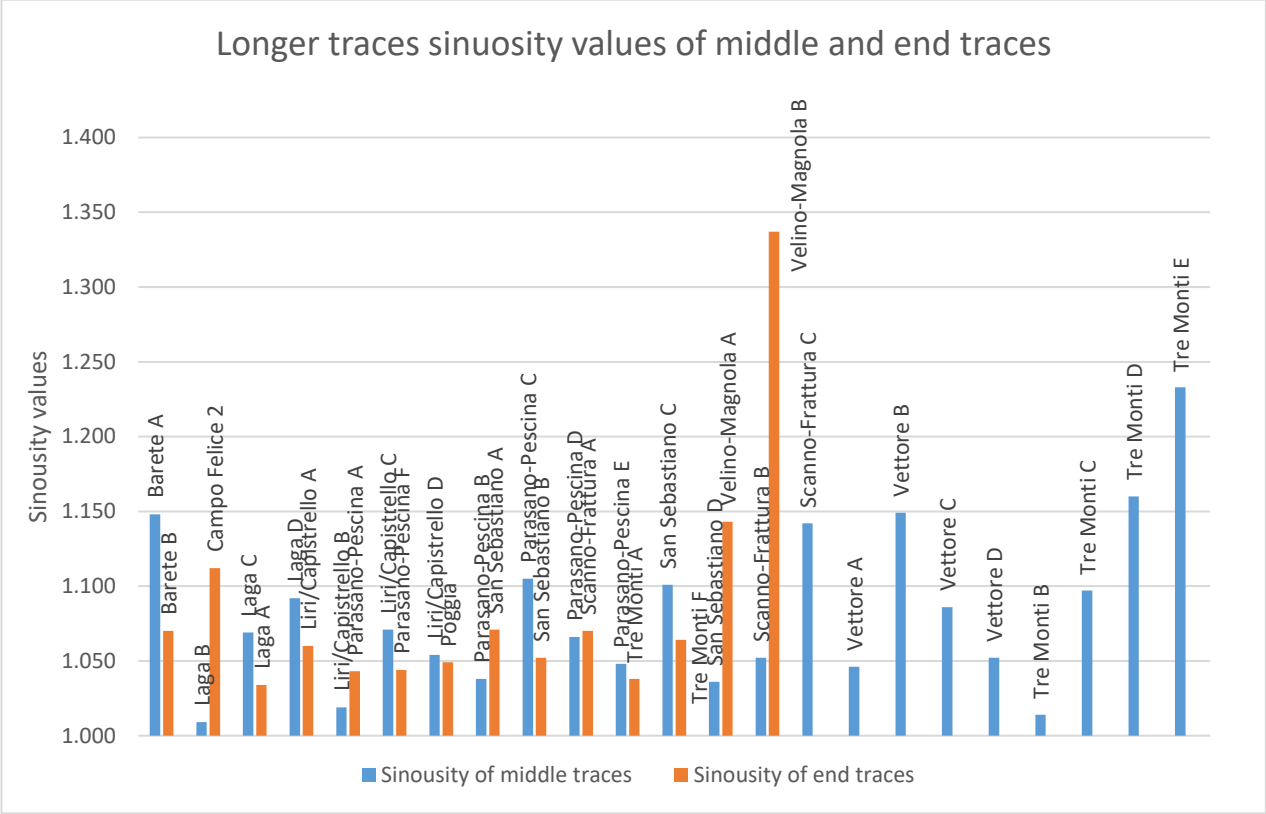

Figure 32 *Comparison of sinuosity values of middle and end traces (longer traces)*

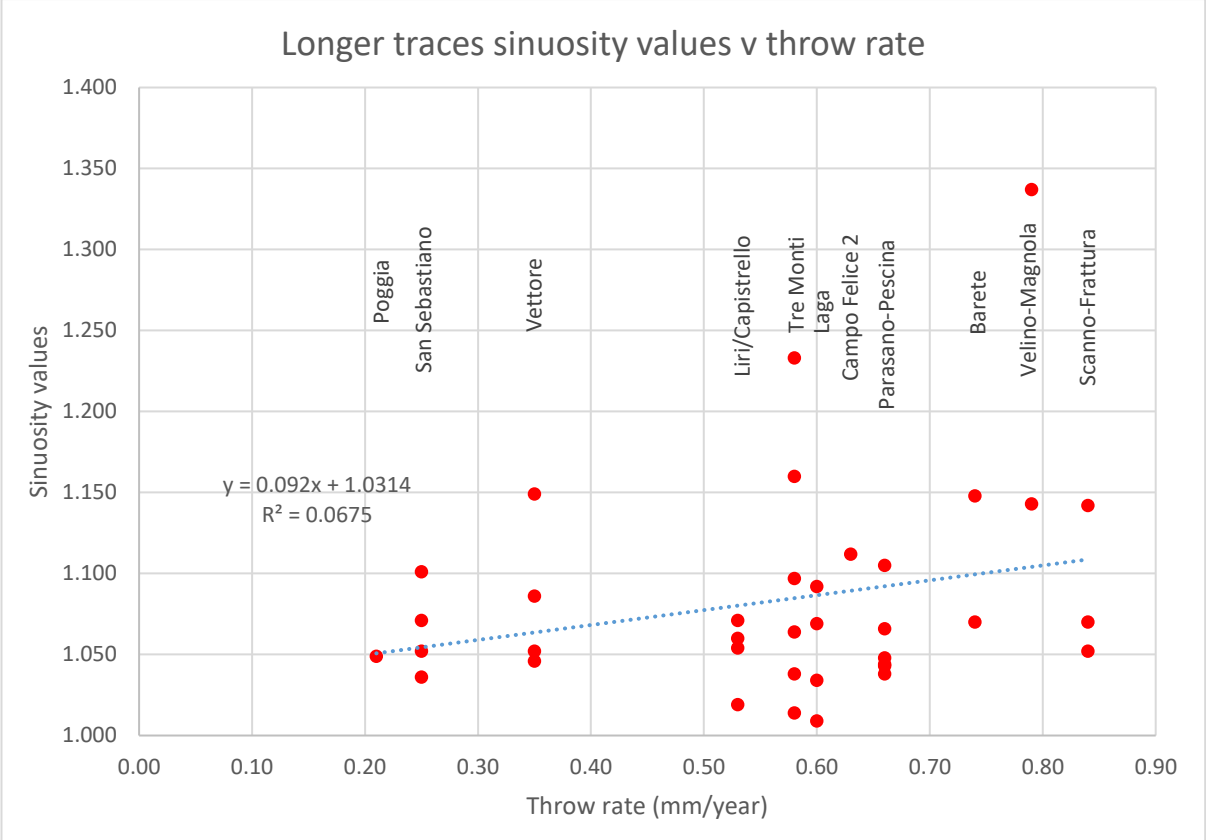

Figure 33 *Comparison of sinuosity values of longer traces against throw rate, from GR 2016 spreadsheet*

Eliminating the Magnola sinuosity values from the comparisons produces no appreciable or statistically valid trend in comparing sinuosity values with fault length and throw rate**.** There does, however, appear to be a moderate degree of positive correlation between sinuosity and projected trace length (**Figure 34)**, with an R^2 figure of 0.1727 (R = 0.42).

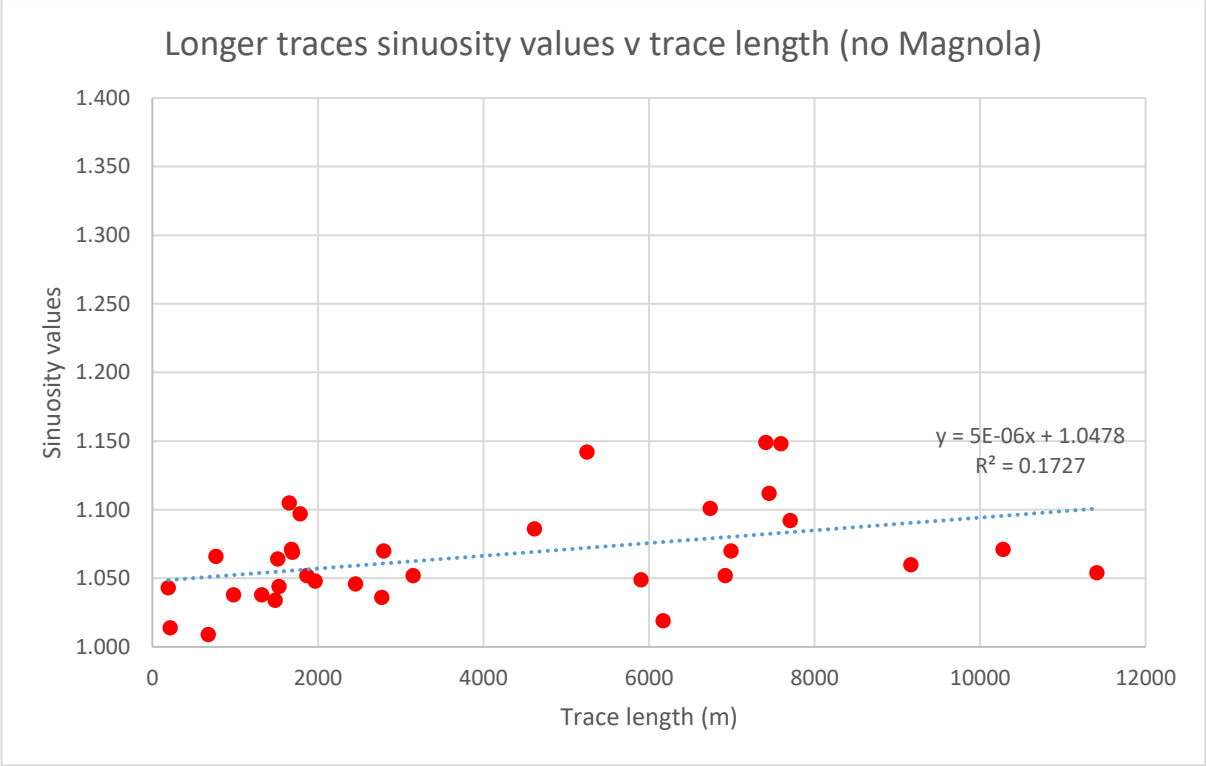

Figure 34 *Longer trace sinuosity values by trace length, omitting results from Magnola Fault*

4.2 Sensitivity analysis for data used in projection of Google Earth traces

4.2.1 Comparison with Roberts and Michetti, 2004 throw rates

The throw rates used in this study are those which appear in the GR 2016 spreadsheet. As noted above, those are averages across the fault, or relate to measurements taken at specific points which do not necessarily equate to the area covered by the relevant trace. The throw rates calculated by Roberts and Michetti (2004) (see 3.2 above) are identified by specific coordinates, which enables a cross–reference to be carried out with the traces mapped. **Appendix D** is a table collating those data, by reference to the individual traces.

Only 13 of the traces directly coincide with individual measurements by Roberts and Michetti. In some cases (notably the Leonessa and Maiella Faults), although the traces coincide, the figures given by Roberts and Michetti for those faults are themselves a range of values (0.33-0.40 and 0.55-0.83 mm/annum respectively), and those have therefore been excluded from the comparison. The figures given show little agreement between the throw rates in the two respective studies (possibly reflecting that subsequent research has built upon and refined the initial Roberts and Michetti findings). **Figure 35** below shows the comparison of sinuosity values against the Roberts and Michetti throw

rate figures. The resulting chart shows a marginal decrease in sinuosity values with throw rate. The statistical relationship is, however, weak (with an R^2 value of 0.0718), and the dataset is small. Therefore, although the comparison suggests a similar conclusion of only weak statistical relationship between throw rate and sinuosity values, its value as a meaningful cross-check is limited.

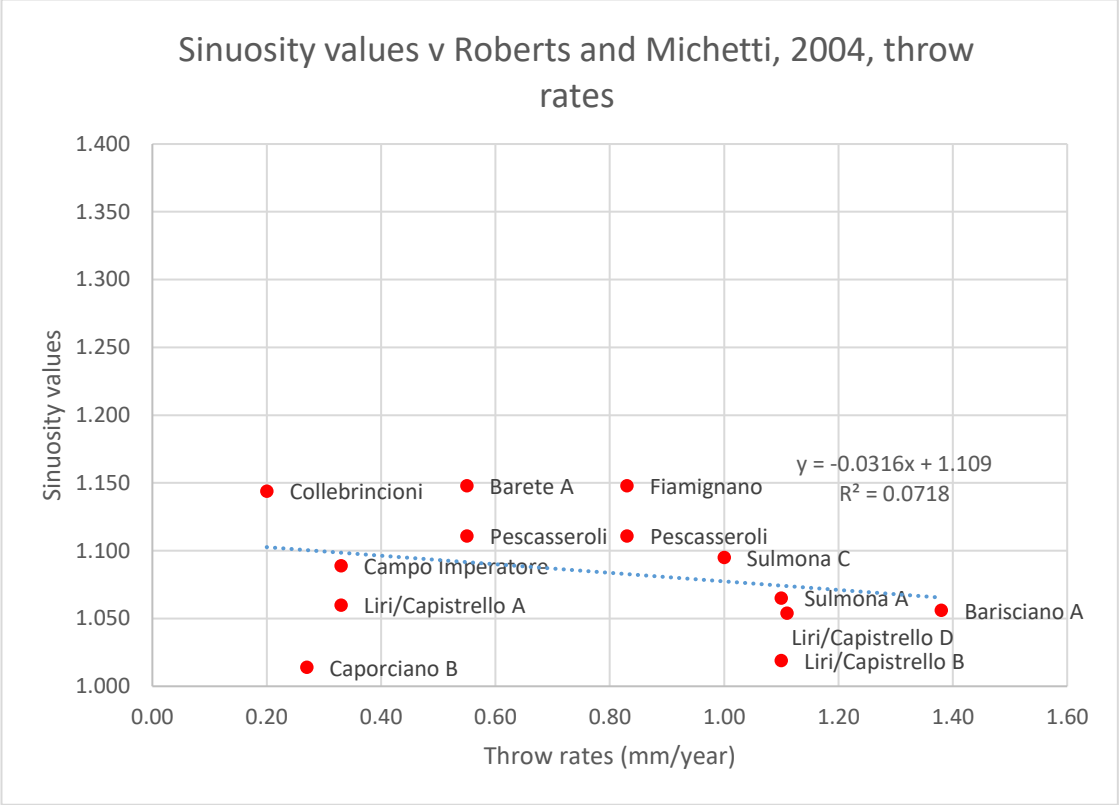

Figure 35 *Sinuosity values against throw rates from Table 1, Roberts and Michetti, 2004*

4.2.2 Use of alternative fault attributes in projection of fault traces

A sensitivity analysis of 6 fault traces using alternative fault attributes (including overall fault strike, average fault dip and average deviation of slip azimuth from dip azimuth), produces the sinuosity figures set out in tabular form below (**Table 4.2.2**):

	Sinuosity value using cosmo slip vector and dip	Sinuosity value using fault strike/cosmo dip	Sinuosity value using cosmo slip vector and average dip (55)	Sinuosity value using fault strike and average dip (55)	Sinuosity value using fault strike - 6 and average dip (55)	Standard Deviation (to 3 d.p.)
Barete A	1.148	1.141	1.111	1.124	1.120	0.015
Fiamignano	1.148	1.175	1.168	1.173	1.190	0.015
Laga D	1.092	1.092	1.094	1.091	1.090	0.001
Liri C	1.071	1.079	1.038	1.104	1.031	0.030
San Sebastiano C	1.101	1.103	1.121	1.118	1.123	0.010
Magnola A	1.143	1.151	1.106	1.106	1.102	0.023
Max to min values	0.077	0.096	0.130	0.082	0.159	

Table 4.2.2 *Table of values showing sensitivity of sinuosity figures to changes in fault attributes used for projection of fault trace.*

The standard deviation figures vary from 0.001 in the case of the Laga D trace to 0.030 in the case of the Liri C trace (where the deviation is more evident from **Figure 36** below, which shows the values by trace). There is, however, little pattern in the variation. The greatest variation in range of values (0.159) is when adjusting fault strike to allow for average difference between slip azimuth and dip values, the smallest (0.077) using cosmogenic site values for slip vector and azimuth (the approach taken in this study).

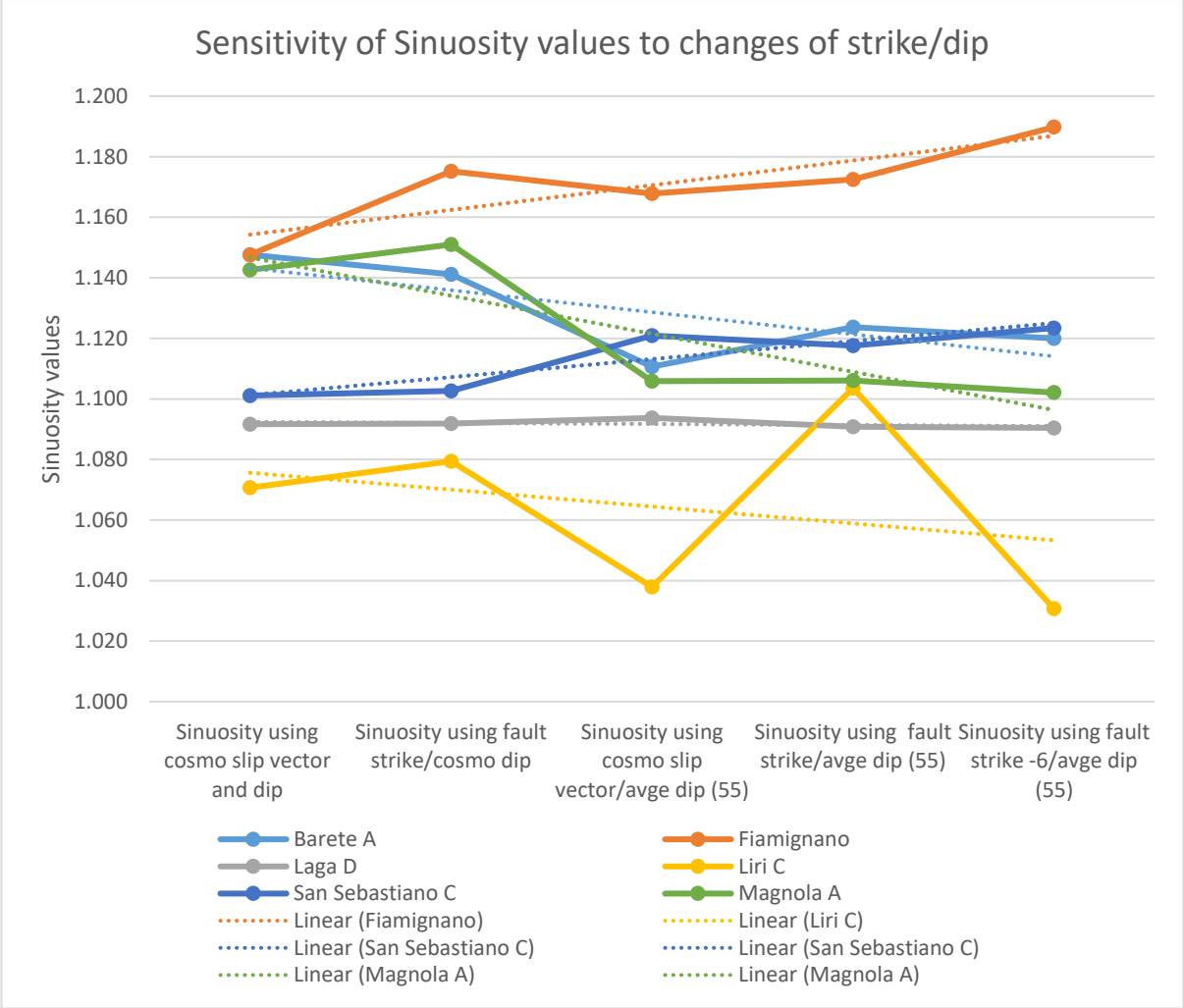

Figure 36 *Sinuosity values calculated using alternative datasets, varying strike and dip*

4.3 LiDAR image traces

4.3.1 Overall sinuosity values using LiDAR datasets

Combining data from the traces from the faults studied using LiDAR data (total number of 121 traces) produces the spread of sinuosity values set out in **Figure 37** below. The mean value is 1.087.

The traces produced using LiDAR data and their respective sinuosity values are set out in **Appendix F**.

The overall results show more variability of sinuosity values than for the Google Earth traces, with both higher values (5 above 1.35, which is the highest value for a Google Earth trace, Magnola B, itself an outlier) and a greater percentage of low values (below 1.05 (59/121 or 49%, compared to 33/85 or 39% for the Google Earth traces).

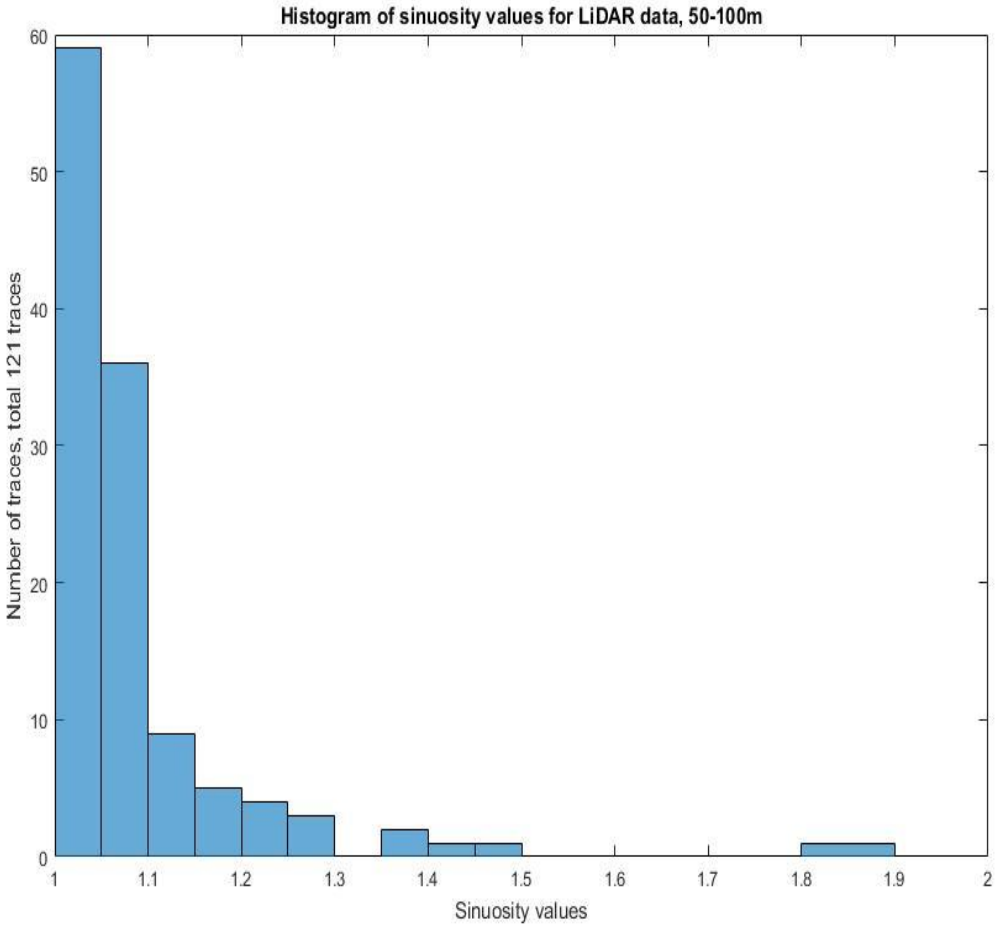

Figure 37 *Histogram showing combined spread of sinuosity values for all small-scale (50-110m) mapped traces from LiDAR data.*

4.3.2 Campo Felice fault

The mapped traces from LiDAR data in ~60 m sections are in two stretches of respectively 2916 and 701 m (against traces mapped through Google Earth of 3786 m, and an overall fault length of 18005 m), with a divide between them where the LiDAR data does not allow a reliable trace to be picked at that scale. The stretches begin and end respectively at 370429, 4677543 and 372256, 4676053 (NW section) and 372477, 4675784 and 372838, 4675400 (SE section). The weighted average sinuosity using LiDAR data is 1.117, against a Google Earth sinuosity figure of 1.112. **Figures 38a and 38b** below show the variation in sinuosity from NW to SE. Average strike for the NW section is 306/53 SW and for the SE section 315/52 SW.

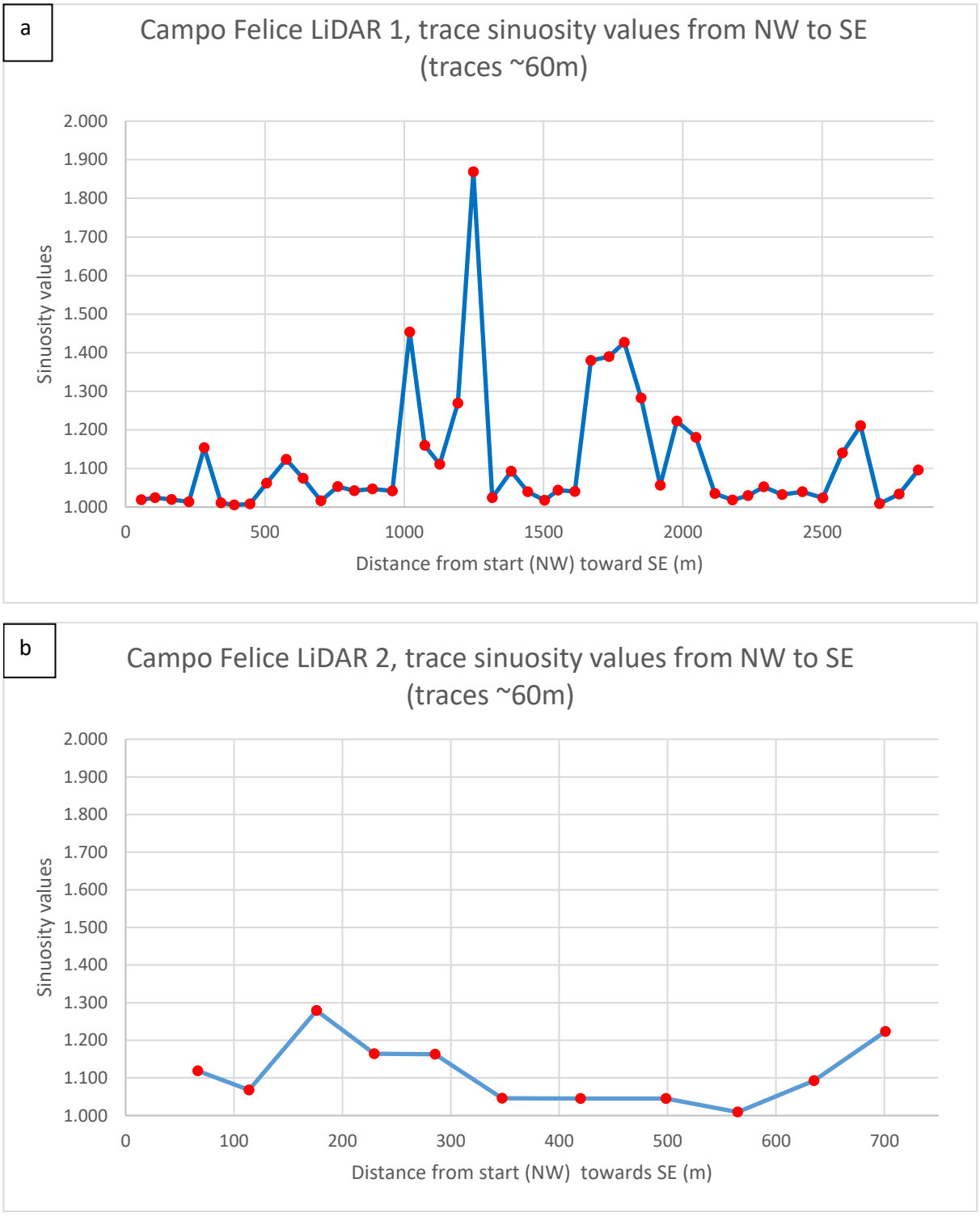

Figure 38 a and b *Sinuosity value profiles of LiDAR data derived traces for Campo Felice fault from NW to SE, traces ~60 m length*

4.3.3 Fiamignano fault

The mapped traces from LiDAR data picked in sections of ~50 m total 1049 m (against mapped traces through Google Earth of 7835 m, and an overall fault length of 27200 m).

The average sinuosity using LiDAR data is 1.066, against a Google Earth sinuosity figure of 1.061. **Figure 39** below shows the variation in sinuosity. The section runs from 344479, 4681907 to 345265, 4681494. Highest sinuosity values are seen at ~800 m from NW towards SE. Average strike and dip is 296/58 SW.

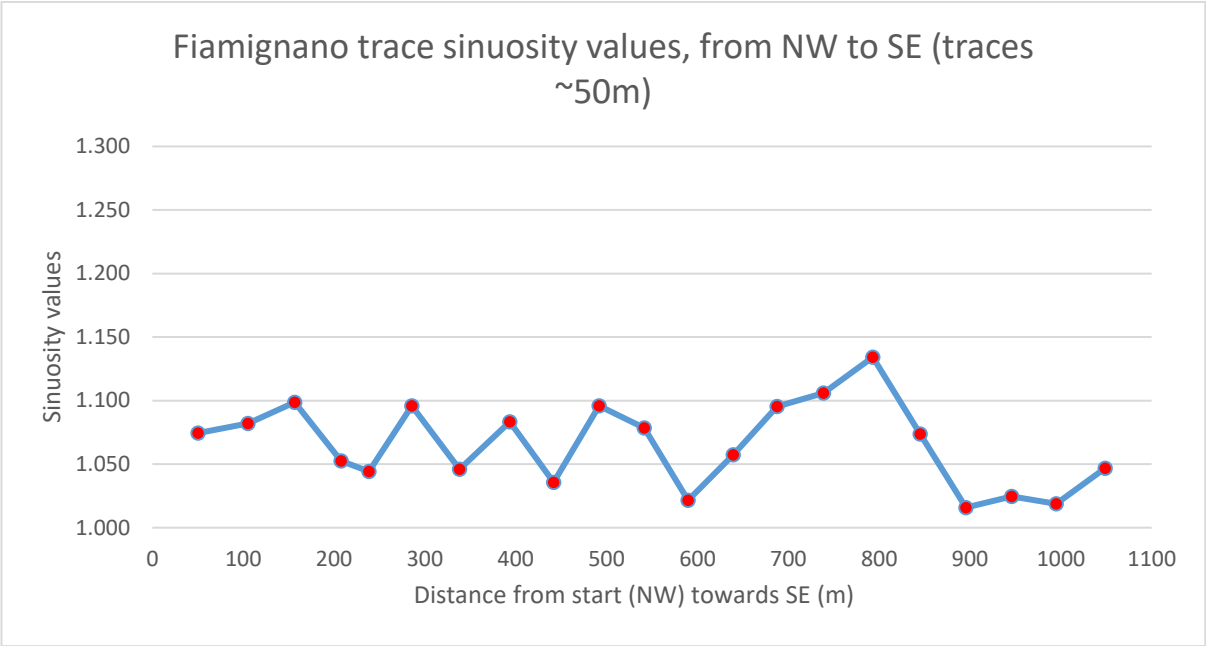

Figure 39 *Sinuosity value profile of LiDAR derived fault traces for Fiamignano fault from NW to SE s, traces ~50 m length*

4.3.4 Magnola fault

The mapped traces from LiDAR data picked in sections of ~115 m total 1031 m (against mapped traces through Google Earth of 6065 m (Magnola A) and 3277 m (Magnola B), and an overall fault length of 9633 m). The weighted average sinuosity using LiDAR data is 1.030, against Google Earth sinuosity figures of 1.143 (A) and 1.337 (B). As noted above, the Google Earth figures are above the norm, whereas the LiDAR data section is well below the norm, and it does not therefore appear representative of the fault at length. The quality of the LiDAR images for this fault do not permit a meaningful examination at smaller scale. The traces may not, therefore, reflect the variation in smaller scale sinuosity values seen with the other faults. **Figure 40** below shows the variation in sinuosity. The section runs from 368113, 4665571 to 369116, 4665106 from NW to SE. Average strike and dip is 279/57 SW.

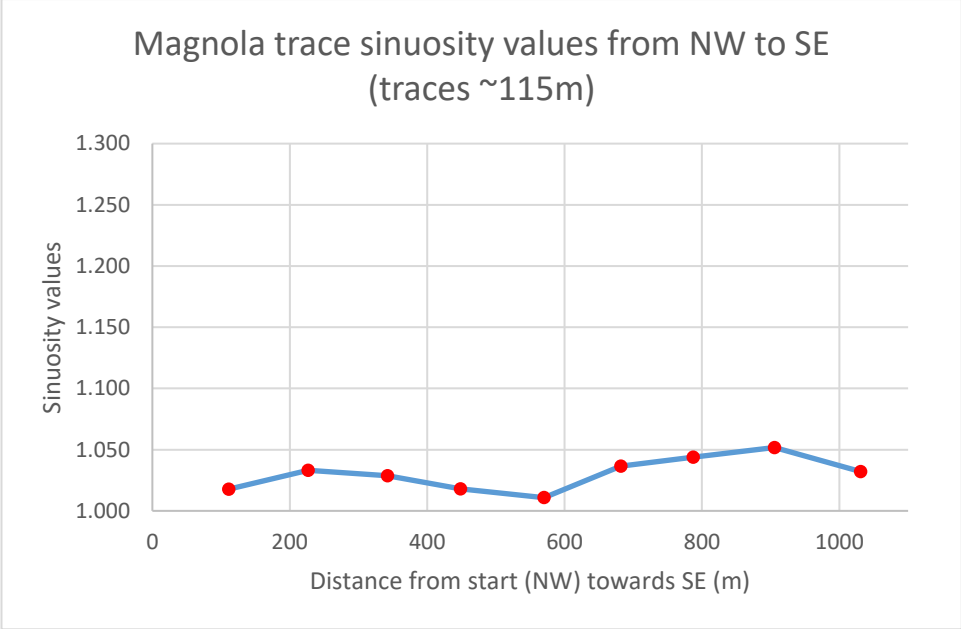

Figure 40 *Sinuosity value profile of LiDAR derived fault traces for Magnola fault from NW to SE, traces ~115 m length*

4.3.5 Parasano fault

The mapped traces from LiDAR data for the Parasano fault total 1997 m using individual sections of ~60 m length (against mapped traces through Google Earth of 6966 m, and an overall fault length of 6950 m). The weighted average sinuosity using LiDAR data is 1.062, against a Google Earth sinuosity figure of 1.061. **Figure 41** below shows the variation in sinuosity from NW to SE at this scale. The traces run from 391434, 4650739 to 393340, 4649466. Average strike and dip is 307/57 SW.

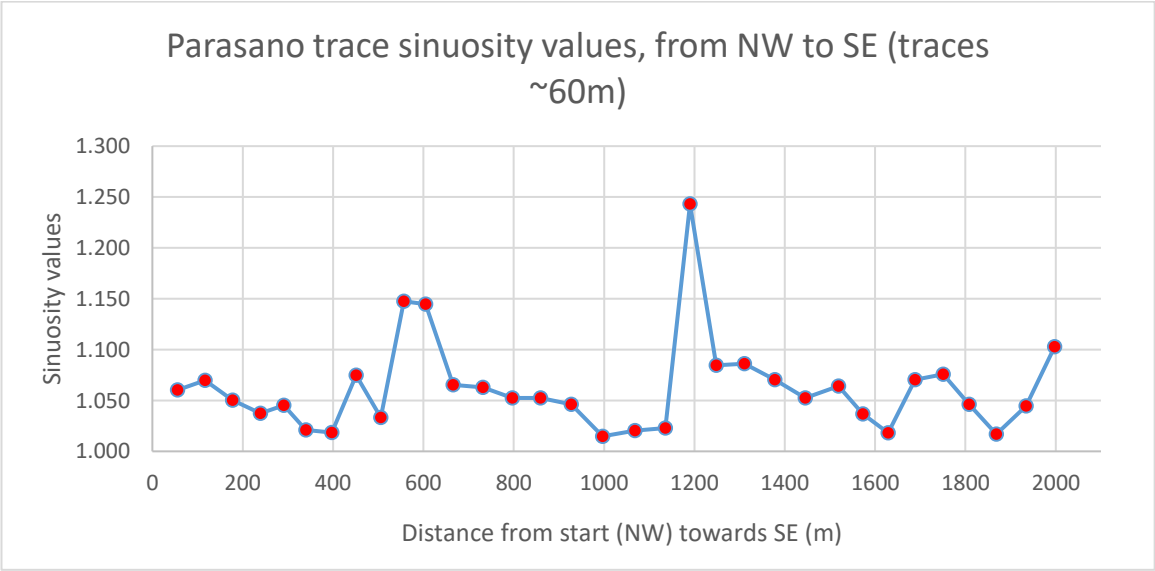

Figure 41 *Sinuosity value profiles of LiDAR data derived traces for Parasano fault from NW to SE, traces ~60 m length*

4.4 Comparison of results from projected traces with non-projected traces

As noted above at 2.4, work by Biasi and Wesnousky (2016, 2017) did not make allowance for topographical effects on the sinuosity values (or "squirrel" as analysed in those studies). Whilst this approach seems to have been adopted due to the large scale nature of their investigations, and the lack of field data, the lack of accounting for topography may have a bearing upon the accuracy of the resulting sinuosity values. Therefore, it is instructive to compare the results from the projected traces against those which rely solely on measurements taken in map view.

Figure 42 below plots against each other the sinuosity values calculated using respectively the non-projected and projected method for the Google Earth derived traces. **Appendix E** identifies the difference in value by individual traces. Of the 85 traces, 58 (68.2%) show greater sinuosity values using the non-projected method, with the remainder (27 traces, 31.2%) showing the opposite (none of the figures was identical at 4 decimal places). Where the non-projected figure is greater than the projected figure, the mean difference in sinuosity values is 0.017. Where the projected figure is greater than the non-projected figure, the mean difference is 0.020. Because of this discrepancy in values, the overall mean difference in sinuosity values is 0.006 (non-projected>projected).

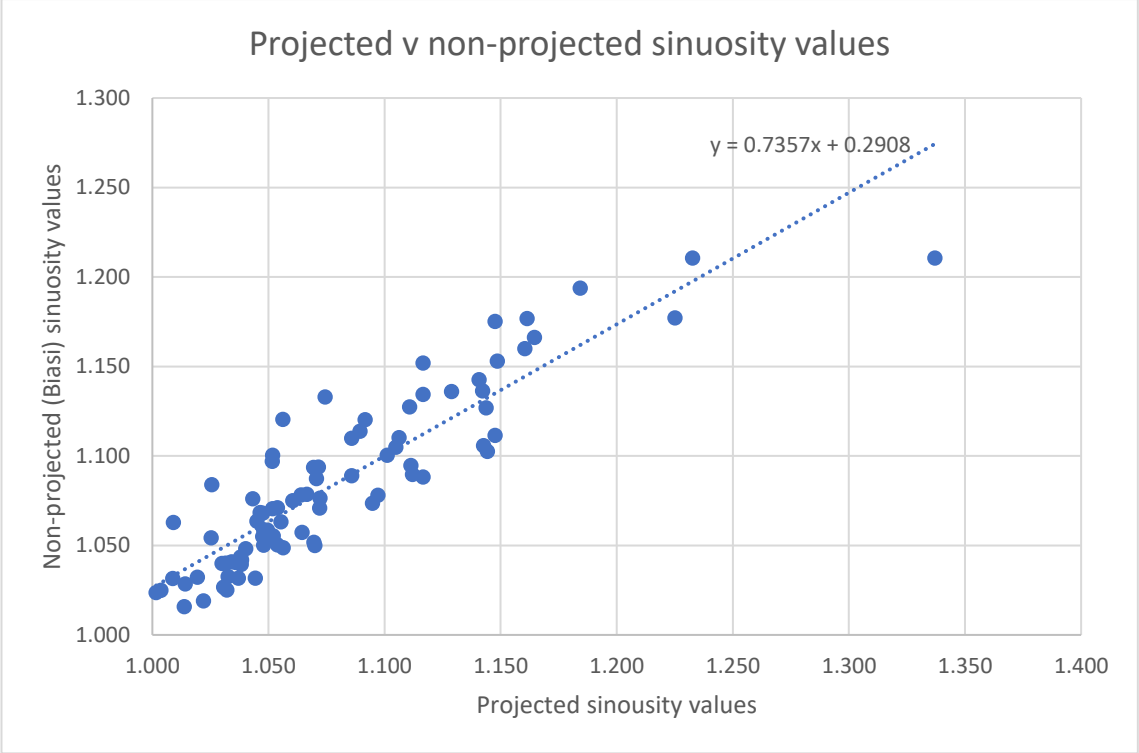

Figure 42 *Comparison of projected v non-projected sinuosity values*

The average strike and dip of faults where the sinuosity values of non-projected traces are greater than the projected traces is 313/58 SW. In the reverse situation, the average strike and dip is 301/52 SW. These compare to average figures of 311/55 SW from the 28 faults. This suggests that the strike and dip figure produced where non-projected trace sinuosity values are greater than projected trace sinuosity values is more in line with the regional average, and in the reverse case more atypical.

Whether the values are higher using the respective methods seems to be dependent upon, inter alia, the dip used for the projection. An example of a trace where the value obtained using projection is higher than the non-projected value is Barete A (projected sinuosity value 1.148, non-projected value 1.111). However, as Table 4.2.2 above shows, if a dip of 55^{o} is used, rather than the cosmogenic site dip value of 39^{o}, the value changes to 1.111 (the same as the non-projected value). If the dip is increased to 65^{o}, the sinuosity value is 1.103 (lower than the value using the Biasi and Wesnousky approach). Another example is Sulmona B, with a projected sinuosity value of 1.232 against a non-projected value of 1.177. If the dip figure of 50^{o} is changed to 70^{o}, the projected sinuosity value is 1.168 (lower than the non-projected value). Some configurations of strike, dip, and

curvature therefore seem to smooth out sinuosity when projection is not used, although the majority have the opposite effect.

4.5 Identification of fracture patterns

4.5.1 Campo Felice fault

75 results for dip and dip azimuth are obtained using the VRGS software for the Campo Felice Fault, converted to strike and dip of the fracture plane. Unsurprisingly, the results show a predominance of strike parallel to the overall strike bearing of the fault. In contoured stereonet[11] form of poles to planes (**Figure 43**), the results show two sets of fractures. One set shows a predominance of planes striking ~140/320° with dips varying between one group of near vertical dips (dipping both SW and NE), and another at ~40-65° (dipping towards the SW). The latter can probably be disregarded as representing the fault scarp itself. A second, less prominent set has a strike of ~045/225°, with dips to the SE of either near vertical, or ~45°.

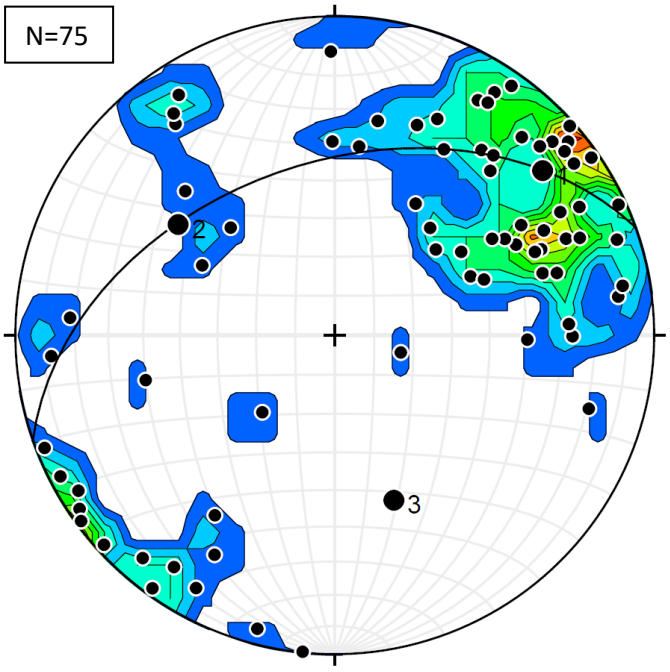

Figure 43 *Contoured Stereonet (at 1% contours) of poles to fracture planes (N = 75) derived from VRGS software for Campo Felice fault, showing cylindrical best fit circle*

[11] Stereonets prepared using Stereonet version 10.1.6, from Rick Allmendinger

4.5.2 Fiamignano Fault

Similar results are shown for the Fiamignano fault. From 77 dips and azimuths the contoured stereonet of poles to planes (**Figure 44**) shows one set of fractures striking towards ~130/310°, with dips varying between one group of near vertical dips (primarily SW, but also NE), and another at ~45-55° (dipping towards the SW). Again, the latter group can probably be disregarded. A second, less prominent set has a strike of ~040/220°, with near vertical dips to the SE and NW.

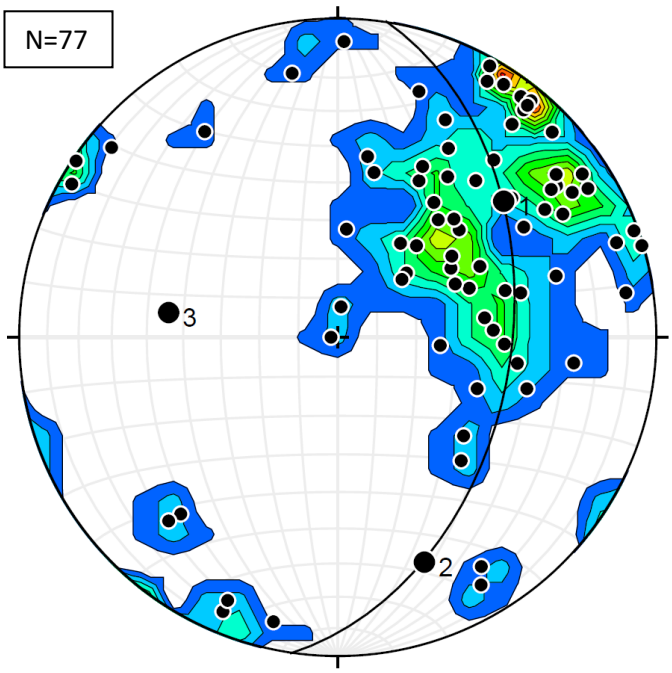

Figure 44 *Contoured Stereonet (at 1% contours) of poles to fracture planes (N = 77) derived from VRGS software for Fiamignano fault, showing cylindrical best fit circle*

The fieldwork dataset of fracture measurements is relatively sparse (15 measurements). However, a contoured stereonet of fracture measurements (**Figure 45**) is consistent with two sets of fractures dipping steeply to the SW at a strike of between ~130-140/310-320° and near vertically to the NE and SW at a strike of ~040/220°.

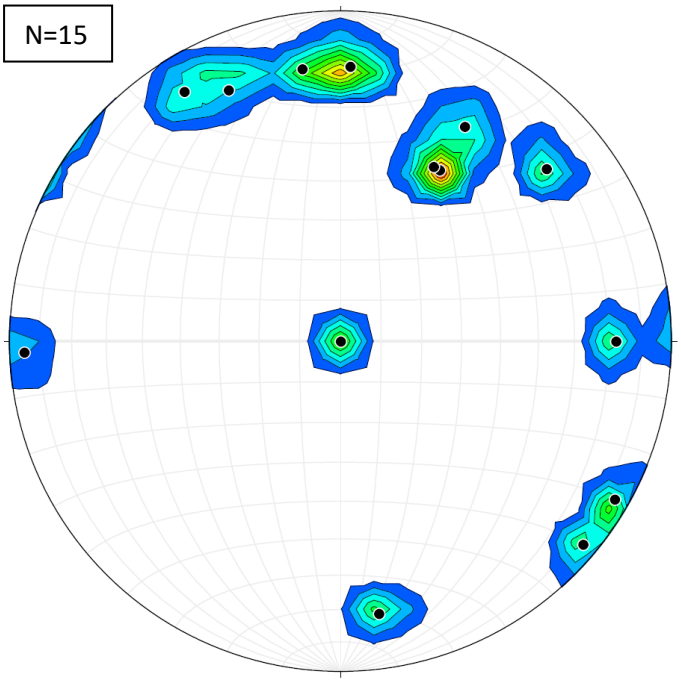

Figure 45 *Contoured Stereonet (at 1% contours) of poles to fracture planes (N = 15) derived from field work data for Fiamignano fault.*

Photos taken during fieldwork suggest that the near vertical fractures at ~040^{o} are cross-cut by the near vertical fractures at ~130^{o} - see **Figure 46** below.

Figure 46 *Photo of Fiamignano Fault scarp, at 034445/4681920 taken on 10 July 2017, showing near vertical cracks across scarp striking ~310^{o}, cross-cutting near vertical cracks up slope, trending ~040^{o}, scale ~4 m across photo, looking NW.*

4.5.3 Parasano Fault

The results for the Parasano fault (from 75 dips and azimuths) are shown as poles to planes on contoured stereonet (**Figure 47**). The stereonet shows one set of fractures with a strike of ~150/330^{o}, with dips varying between one group of near vertical dips (exclusively SW), and another at ~50-60/230-240^{o} (dipping towards the SW). Again, the latter group can probably be disregarded. A second, less prominent set has a strike of ~050/230^{o}, with near vertical dips to the SE and NW.

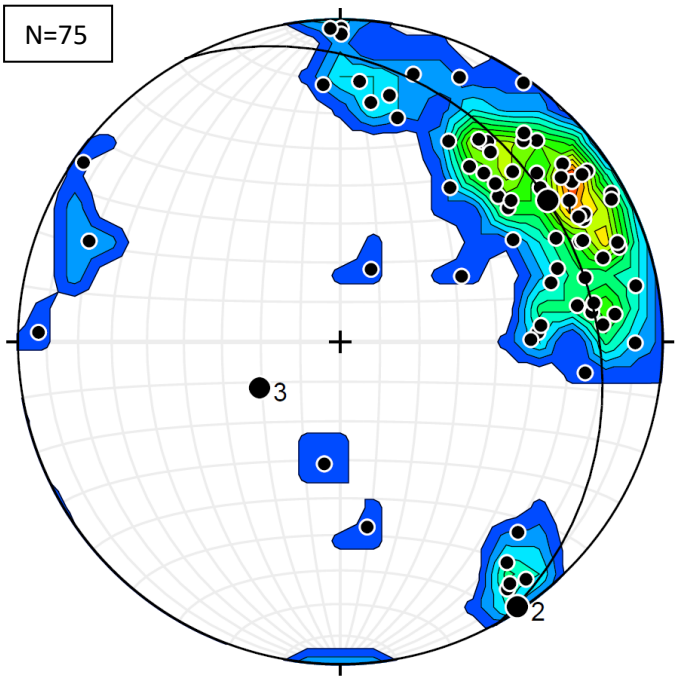

Figure 47 *Contoured Stereonet (at 1% contours) of poles to fracture planes (N = 75) derived from VRGS software for Parasano fault, showing cylindrical best fit circle*

4.6 Identification of local topographical features relating to more sinuous LiDAR trace segments.

4.6.1 Campo Felice fault

Among the more sinuous LiDAR traces from the Campo Felice fault are those between CF 1.28 and CF 1.32, which peak at 1.038 (CF 1.29), 1.039 (CF 1.30), and 1.283 (CF 1.31). **Figure 48** below shows those traces imported into Google Earth. The highest value (CF 1.30), shown in red, derives from a linkage between two stretches of the fault scarp which deviate very substantially from the trend of the fault. In the case of CF 1.29 the trace appears to have stepped to the right along the line of a gulley which continues both above

and below the slip, which trends SW-NE at ~056°. In the case of CF 1.31 the step appears to be to the left, along a less pronounced gulley (continuing above the fault scarp), trending SW-NE at ~ 055°. Similar gullies or features can be seen to the left side of the picture, above the fault scarp. NB the view is tilted to the NNE.

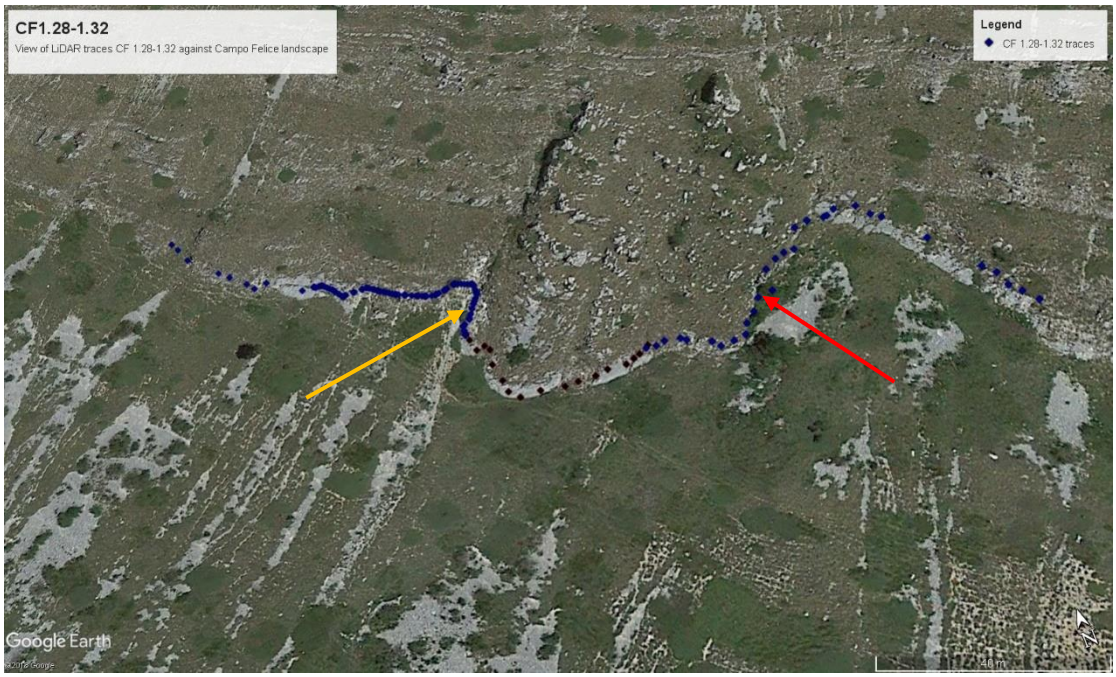

Figure 48 *LiDAR image-derived traces CF 1.28-1.32 exported to Google Earth as .kml from .dxf files, showing relationship of more sinuous parts of trace to local topography, rotated to face NNE. CF 1.30 shown in red, others in blue. Area of deviation at CF1.29 highlighted by yellow arrow, deviation at CF1.31 by red arrow*

Other notably sinuous segments are CF 1.18 (sinuosity value 1.454), CF 1.21 (1.261) and CF 1.22 (1.869). Those are all shown within the context of CF 1.17 to 1.23 (**Figure 49,** below). In this case, the view is tilted to the NE. The deviation from strike seems to be driven by similar features. The deviation in the case of CF 1.18 relates to an apparent step to the left along the line of a generally SW-NE trending gulley, both above and below the fault scarp, at ~050°. The most pronounced deviation from strike (CF 1.22) involving an apparent step to the left movement spanning both sides of a SW-NE trending gulley (above and below the fault scarp) at~054°. To the W of that, at CF 1.21, the movement is dextral, along the line of what appears to be a short-lived gulley at ~016°, which does not extend above the fault scarp. Other gullies above the fault scarp which do not appear to alter the strike of the traces are largely uniformly at ~055°.

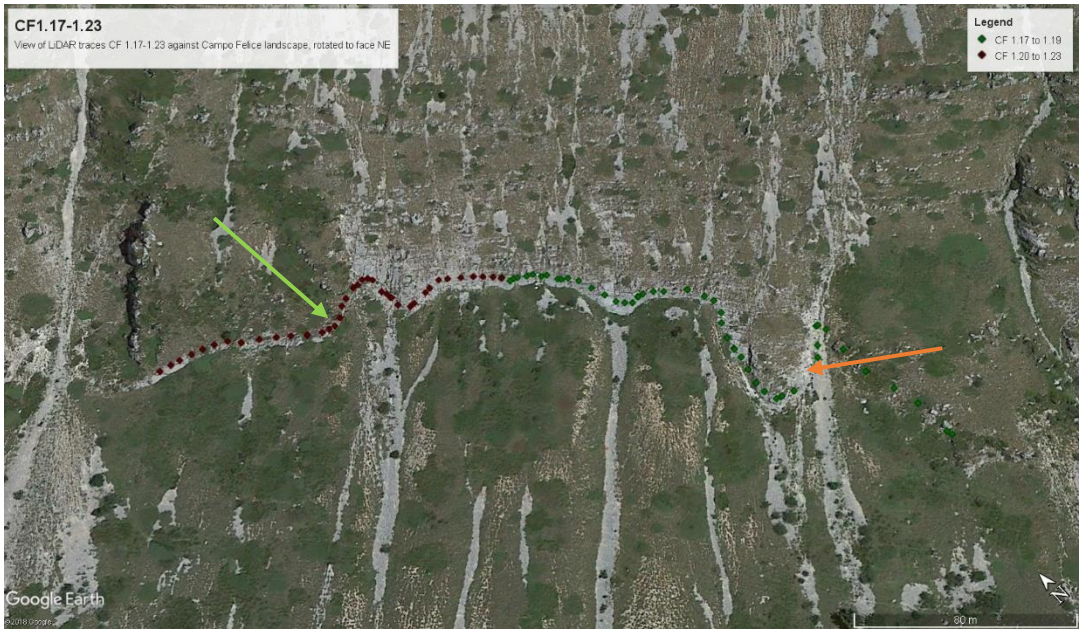

Figure 49 *LiDAR image-derived traces CF 1.17-1.23 exported to Google Earth as .kml from .dxf files, showing relationship of more sinuous parts of trace to local topography, rotated to face NE. CF 1.17-1.19 shown in red, others in green. Area of deviation at CF 1.18 highlighted by green arrow, deviation at CF 1.21 by orange arrow*

The relative position of both of the above to the Google Earth derived fault traces for the Campo Felice fault is shown in **Figure 50.**

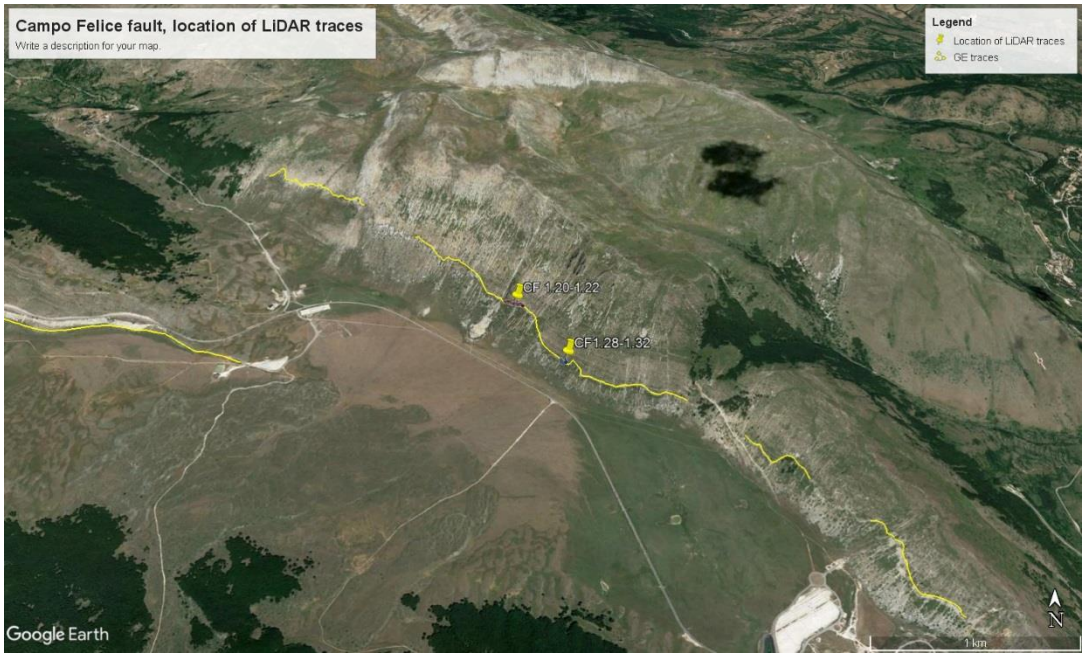

Figure 50 *Location of LiDAR image-derived traces in relation to Google Earth-derived traces for Campo Felice fault (marked by yellow pins).*

4.6.2 Fiamignano Fault

The sinuosity values for the Fiamignano have few notable highs. The highest value is 1.134, seen at Fiam 36. **Figure 51** below shows this (left of centre), as part of what is an otherwise unremarkable sequence of values of 1.106, 1.134, 1.074 and 1.016 (Fiam 35-38). At Fiam 36 the scarp takes what appear to be two steps to the left away from the normal strike (which at this point is ~270^{o}), at an angle of nearly zero degrees. There is no obvious local reason for the abrupt changes. Gullies further E and W of this point trend ~030-040^{o}.

Figure 51 *LiDAR image-derived traces Fiamignano 35-38 exported to Google Earth as .kml from .dxf files, showing relationship of more sinuous parts of trace to local topography. Areas of deviation at Fiam 36 marked by light blue arrows.*

The relative position of Fiam 35-38 to the Google Earth derived Fiamignano fault trace is shown in **Figure 52**, below, marked by yellow pin.

Figure 52 *Location of LiDAR image-derived traces in relation to Google Earth-derived trace for Fiamignano fault.*

4.6.3 Parasano Fault

As noted above, the LiDAR fault trace from the Parasano Fault does not produce any notable sinuosity figures. The exception appears to be Para 1.20, where a sinuosity value of 1.243 is shown (against neighbouring values of 1.023 (Para 1.19) and 1.084 (Para 1.21)). This is shown exported to Google Earth in **Figure 53** below, tilted towards the NNE. Again, the deviation from strike appears to be associated with a gulley which continues below the fault scarp, but not significantly above it. The gulley trends towards the NNE, at ~030^{o}, and the predominant movement appears to be a step to the left. The scarp itself is less obvious on Google Earth. Few gullies in this part of the Parasano fault extend appreciably into the footwall, which is closer to the top of the slope than in the case of Campo Felice, and therefore the topography of the footwall is possibly more influenced by glacial erosion.

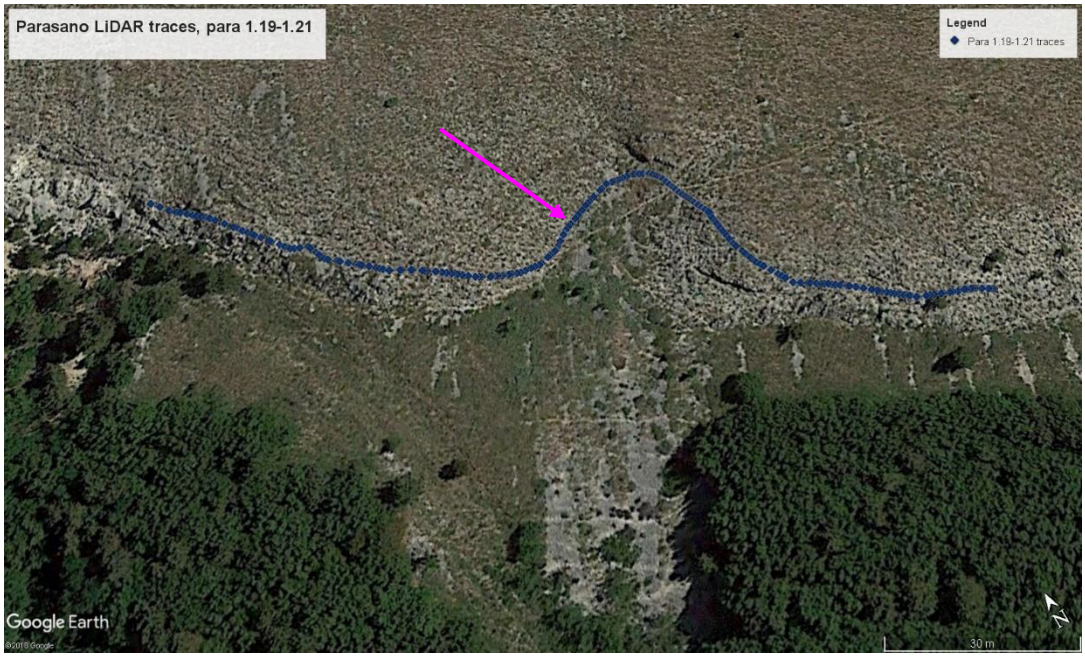

Figure 53 *LiDAR image-derived traces Parasano 1.19-1.21 exported to Google Earth as .kml from .dxf files, showing relationship of more sinuous parts of trace to local topography, rotated to face NNE. Area of deviation at para 1.20 marked by pink arrow.*

The relative position of Parasano 1.19-1.21 to the Google Earth derived Parasano fault traces is shown in **Figure 54**, below.

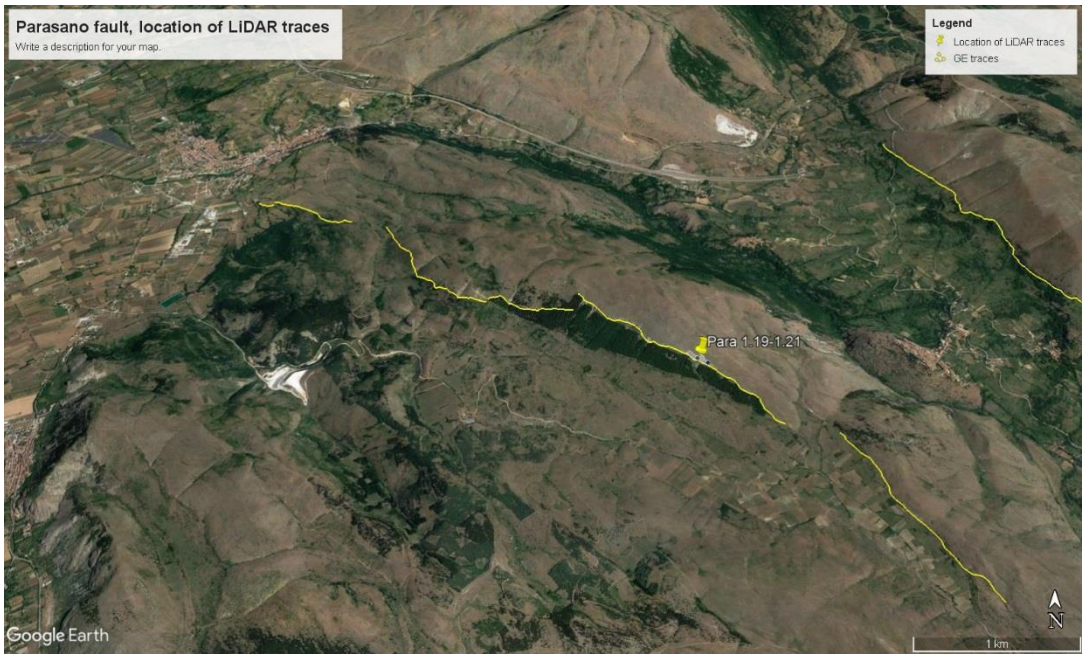

Figure 54 *Location of LiDAR image-derived traces in relation to Google Earth-derived traces for Parasano fault (marked with yellow pin).*

4.7 Summary of results for Google and LiDAR traces

4.7.1 Google Earth traces

The expected relationships between sinuosity and fault length, and slip rate for the whole fault length Google Earth traces do not appear strongly from the results, and are inconclusive, even when the traces are narrowed down to the "longer traces" subset, which should be more representative of the overall faults. There seems to be some moderate correlation between increasing projected trace length and sinuosity values, however this result should be treated with caution, as projected trace length depends upon whether a trace is sufficiently visible in Google Earth to be picked - the relationship may be a reflection only of the possible increased visibility of a sinuous part of a fault trace.

The results show that increasing length of fault reduces both the sinuosity values seen, and their variability (**Figure 25**), supporting the expected smoothing out of fault traces with further movement, particularly in the centre of a fault. The overall conclusion is not supported by an analysis of "middle" and "end" traces, where the values suggest that the sinuosity of "end" traces is significantly lower than "middle" traces when outliers are removed. However, the population of "end" traces is sufficiently small that this may not be significant.

4.7.2. LiDAR traces

As expected, the sinuosity results for the LiDAR traces (at <100 m scale) show increased variability compared to the Google Earth traces. There are both more low values shown, and much higher values. This is unsurprising, as the scale observed both allows for relatively straight sections, where there is no deviation from strike, and also localised major deviations which produce high values. The along-strike profiles produced enable localised high sinuosity values to be identified, and studied in the context of Google Earth images for those areas. In most cases, the deviations from strike seen in the form of side-stepping in the fault traces seem to match up with localised features (often shown in gullies in the footwall), which in turn match with fracture patterns seen. This suggests that the deviations (and sinuosity) seen at this scale are the result of localised inherited structures, typically striking ~SW-NE.

4.7.3 Anomalies

The Google Earth traces highlight the anomalous values for two faults, Magnola, and Tre Monti, both of which deviate from the local average strike, in the latter case substantially. Magnola produces much higher sinuosity values than other faults, and Tre Monti a much wider spread, including some high values. An analysis of sinuosity values by strike (**Figure 28**) suggests that there is correlation between lower sinuosity values and strikes around the regional average, or clockwise from that strike. This suggests that, where faults follow the strike line of the current regional extensional regime, sinuosity values are lower, whereas where fault strikes deviate towards the line of previous extensional regimes (oriented more towards SW-NE, ie anticlockwise from the current regime) sinuosity values increase.

Chapter 5 Results/Analysis – Coulomb Stress Modelling

5.1 Method applied to Coulomb Stress transfer modelling

The theory behind Coulomb Stress modelling is explained in the Methodology section, above (section 3.6). The receiver faults modelled are Fiamignano, Magnola, Parasano, San Sebastiano, and Tre Monti. Their location relative to each other in the Apennines is shown in the DEM at **Figure 55** below.

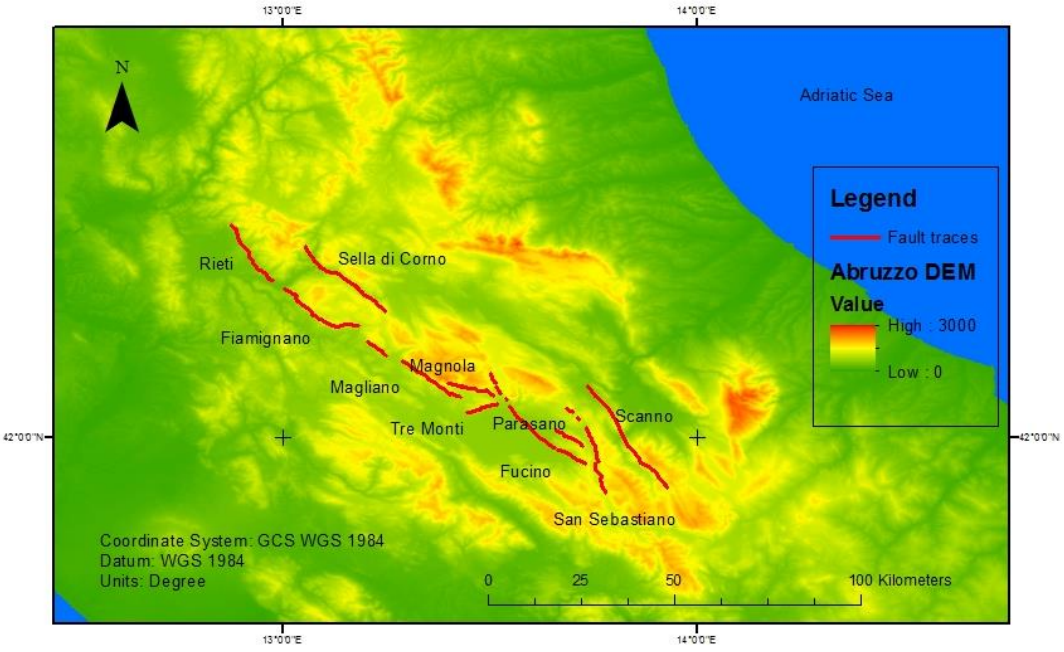

Figure 55 *DEM of central Apennine region showing relative location of receiver faults modelled using Coulomb Stress modelling (with place marks), also showing source faults modelled.*

The selection of faults combines two faults (Fiamignano, and Parasano) which are close to the regional strike average of 311° (from the overall fault strike figures for the 28 faults data taken from the GR 2016 spreadsheet, which produce an average strike and dip of 311/55 SW), and three faults (Magnola, San Sebastiano and Tre Monti) which are at variance to the regional trend. The respective overall strikes are Fiamignano 311°, Magnola 290°, Parasano 308°, San Sebastiano 336°, and Tre Monti 248°. The dips used in the models are taken from the GR 2016 spreadsheet, as are overall lengths of the faults. The faults chosen for modelling also include all those for which LiDAR data is available, except Campo Felice, where no suitable source faults were identified for modelling.

The data used for the source faults are also taken primarily from the GR 2016 spreadsheet. In the case of the Fiamignano fault as receiver fault, the Sella di Corno fault is modelled as the principal source fault. This fault does not appear on the GR 2016 spreadsheet, so overall strike (308^{o}) and length is taken from the trace in the Abruzzo GE .kml file. Dip is taken as being the regional average (55^{o}), and slip calculated by averaging slip by fault length across the GR 2016 spreadsheet data (which produces 0.56mm of slip per metre of fault length over 15,000 years). The Rieti Fault is also modelled, data taken again from the trace in the Abruzzo GE .kml file rather than the GR 2016 spreadsheet. The trace has an overall strike of 331^{o}, and length of 17 km. Dip is taken as the regional average, and slip estimated from average slip by fault length.

For the Magnola fault as receiver fault, the source faults modelled are Magliano dei Marsi (Magliano) and Fucino (or Gioia dei Marsi). Magliano does not appear on the GR 2016 spreadsheet, so the same approach is adopted as with Sella di Corno for Fiamignano, producing a strike of 310^{o}. The data for Fucino come primarily from the GR 2016 spreadsheet. However, given the length of the fault compared to its neighbours, and apparent variation in strike over distance, it is modelled as a fault of 20 km length, with a strike of 312^{o}, but with overall slip from the GR 2016 spreadsheet.

For the Parasano fault as receiver fault, the source faults modelled are Fucino and San Sebastiano. The data for the latter come from the GR 2016 spreadsheet. The data for Fucino are amended as in the case of Magnola (above), but in this case with 25 km fault length and strike of 316^{o}.

For the San Sebastiano fault as receiver fault, the source faults modelled are Fucino, Parasano, and Scanno-Frattura (Scanno). All data is from the GR 2016 spreadsheet, with an alteration for Fucino applied as for Parasano (in this case 25 km fault length and strike of 322^{o}).

A plan showing the simplified geometries of the receiver faults, with their neighbouring faults is at **Figure 56** below.

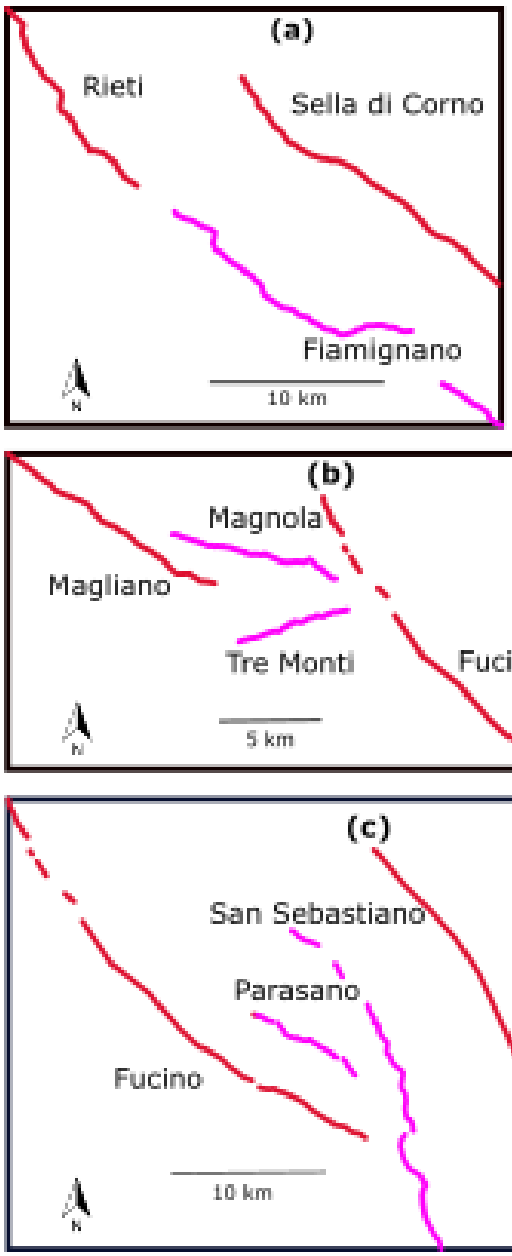

Simpified geometries of traces of (a) Fiamignano, (b) Magnola and Tre Monti, and (c) Parasano and San Sebastiano with neighbouring faults

Figure 56 *Simplified geometries of source and receiver faults modelled.*

Models are run in the first instance without tapering in the source fault. In addition, at 15 ka an alternative model is run with tapering with depth of the source fault along strike, and down dip. An example of a tapered source fault from the USGS Coulomb 3.3 User Guide is at **Figure 57** below.

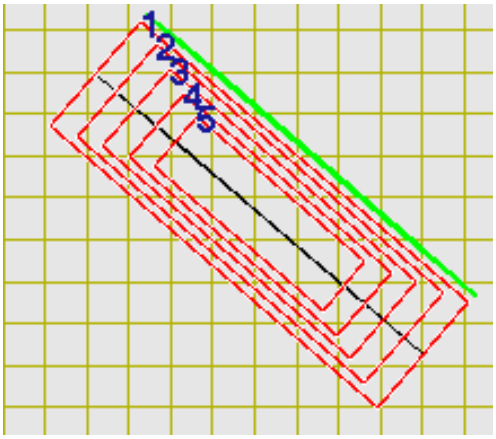

Figure 57 *Example of tapered source fault slip, from USGS Coulomb 3.3 User Guide, with nested rectangles, adjustable along strike and down dip, designed to remove unrealistic stress concentrations at the edge of a fault, showing 5 nested patches.*

The tapering intervals applied by source fault (from edges along strike) are:

- Fucino, 5 x 4 km patches along strike, 5 x 1 km down dip;
- Magliano, 5 x 3 km patches along strike, 5 x 1 km down dip;
- Magnola, 5 x 2 km patches along strike, 5 x 1 km down dip;
- Parasano, 5 x 1 km patches along strike, 5 x 1 km down dip;
- Rieti, 5 x 3 km patches along strike, 5 x 1 km down dip;
- San Sebastiano, 5 x 2 km patches along strike, 5 x 1 km down dip;
- Scanno, 5 x 4 km patches along strike, 5 x 1 km down dip;
- Sella di Corno, 5 x 4 km patches along strike, 5 x 1 km down dip.

In the cases of the Fiamignano, Parasano and Tre Monti faults, further models have been run to model individual segments within each of those faults as respectively source and receiver faults. Those are described in more detail in the individual results sections (by receiver faults) below.

In each case, the Coulomb Stress change output models are shown with coordinates based upon an arbitrary origin. Save where indicated, the source fault in each case is numbered 1, the receiver fault(s) 2 and above. The bold green line represents the surface trace, the red box the fault plane, and (where shown) the black line the depth modelled.

A positive Coulomb shear stress change of > 50 bar (5 MPa) is taken as being the threshold for likely kinematic effect between the source and receiver fault (although the existing stress state of the receiver fault is not known).

5.2 Fiamignano

5.2.1 Geometry of Fiamignano fault

The Fiamignano fault shows apparent sinuosity on the surface, with significant deviations in strike both towards the NW end and more centrally. The traces from the Abruzzo GE .kml file, which are not continuous, are shown in **Figure 58** below. The trace picked for the purpose of the analysis of sinuosity, as projected in MOVE, appears in **Figure 59** below, providing a sinuosity value of 1.148 (one of the highest values at that scale), although this represents only ~30% of the fault trace. With an overall strike of 311°, the Fiamignano fault matches the regional average. However, within the trace there are significant deviations. From the NW end, after starting on a strike bearing of ~310°, the trace deviates towards a bearing of 010° before resuming its previous bearing. At about the midpoint of the trace, it then takes an anticlockwise turn towards 255°, before turning to ~270°. The final (SE) section is also at a strike of ~310°. The unmapped "gap" between the segments suggests a missing link with an overall strike bearing of ~330°.

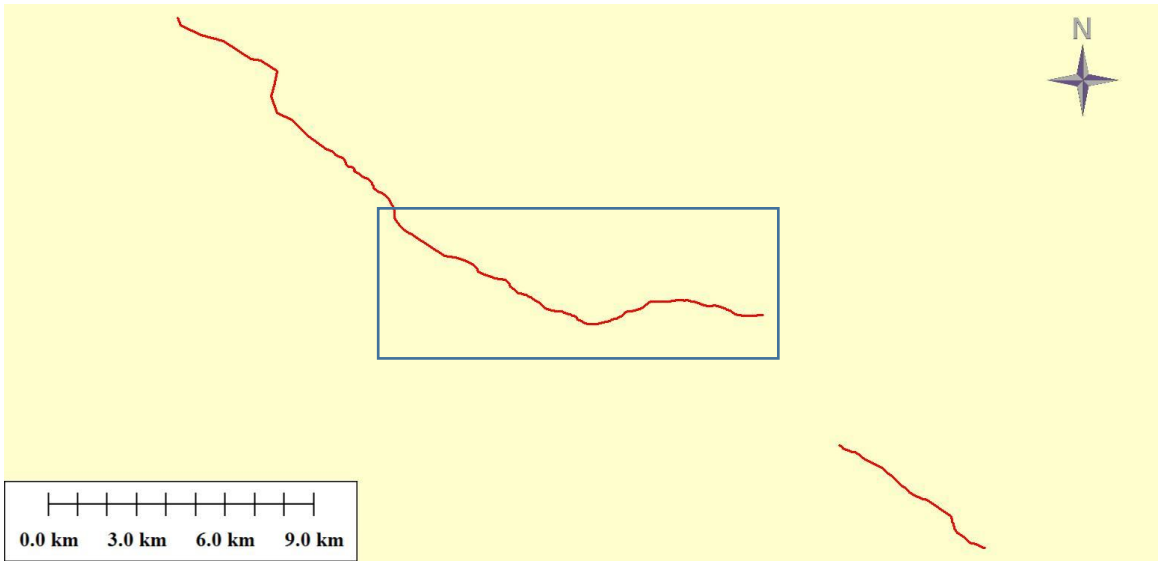

Figure 58 *Map view Abruzzo GE .kml file fault trace profile for Fiamignano fault, box showing area covered by projected trace in Figure 59 below.*

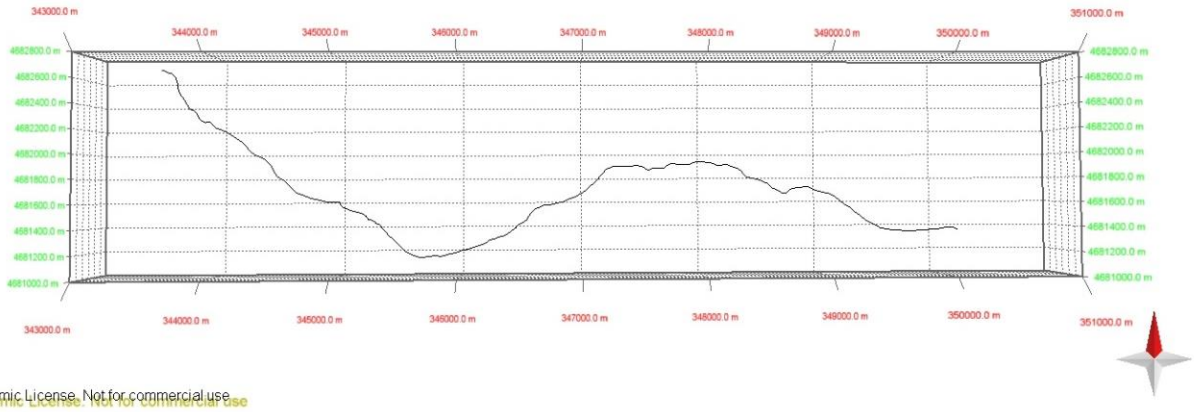

Figure 59 *Google Earth fault trace profile for Fiamignano fault (projected in MOVE).*

The source faults modelled for the Fiamignano fault are the Sella di Corno fault, up dip to the NE and broadly parallel (at 317^{o} overall strike) to the Fiamignano fault (311^{o} overall strike), and the Rieti fault, which continues the trend of the Fiamignano fault (at the same overall strike of 311^{o}) ~3 km to the NW end of the Fiamignano fault.

At 15 ka (which is when both maximum slip and fault length apply), the total seismic moments calculated are 7.17 Mw (Sella di Corno), and 7.18 Mw (Rieti). The changes in Coulomb Stress in each case over time are explained more fully in **Appendix G.**

5.2.2 Sella di Corno fault as source fault to Fiamignano

The Coulomb Stress models for Sella di Corno show almost exclusively negative change in Coulomb shear stress, or limited positive change in Coulomb shear stress from that fault to Fiamignano as the receiving fault. It is only at ~15 ka that the positive change in Coulomb shear stress at surface approaches 30-40 bar. **Figure 60** shows a largely uniform spread of positive change in Coulomb shear stress along much of the length of the Fiamignano fault at the surface level, particularly towards the NW end. At 5 km depth the change in Coulomb shear stress remains negative. However, both faults are modelled as projections from straight lines, and transposing the Coulomb stress change result as a stress contour map onto the Abruzzo GE .kml file fault traces, only the central and NW end of the trace exceed 25 bar, with the SE end between 0 and 25 bar. It is therefore unlikely that down-dip movement on the Sella di Corno fault has any significant impact upon the Fiamignano fault.

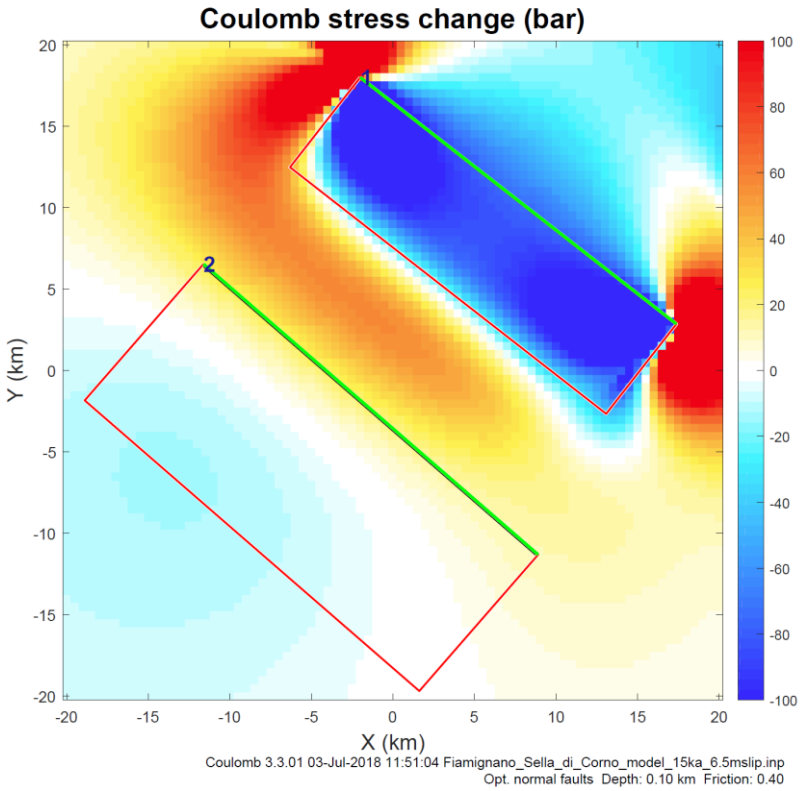

Figure 60 *Coulomb Stress model output for Sella di Corno (source) (1) and Fiamignano (receiver) (2) faults, variable and constant length models shown at 0.1 km depth (surface), result at 15 ka.*

5.2.3 Rieti fault as source fault to Fiamignano

In the case of the Rieti fault, over time the positive change in Coulomb shear stress transfer from the SE end of the Rieti fault impacts upon the NW end of the Fiamignano fault. **Figure 61** below shows the position at 15 ka at surface. Both at surface and at depth the positive change in Coulomb shear stress exceeds 50 bar, with the positive change being greater at the surface. On the constant length model, over time the positive change in Coulomb shear stress takes place over an increasing length of the NW end of the Fiamignano fault. The variable length models show increased impact from ~9 ka. **Figure 62** shows the contour map of the change in Coulomb shear stress superimposed on the Abruzzo GE .kml file traces at 15 ka. The dividing line where the stress change exceeds 50 bar coincides approximately with the deviation of the trace from a strike of ~310^{o} towards ~010^{o}.

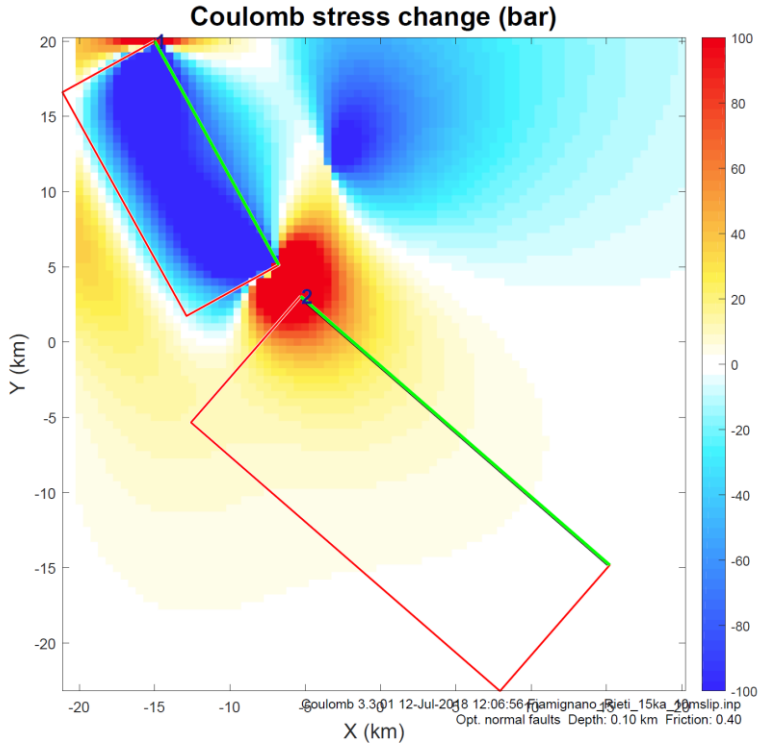

Figure 61 *Coulomb Stress model output for Rieti (source) (1) and Fiamignano (receiver) (2) faults, variable and constant length models shown at 0.1 km depth (surface), result at 15 ka.*

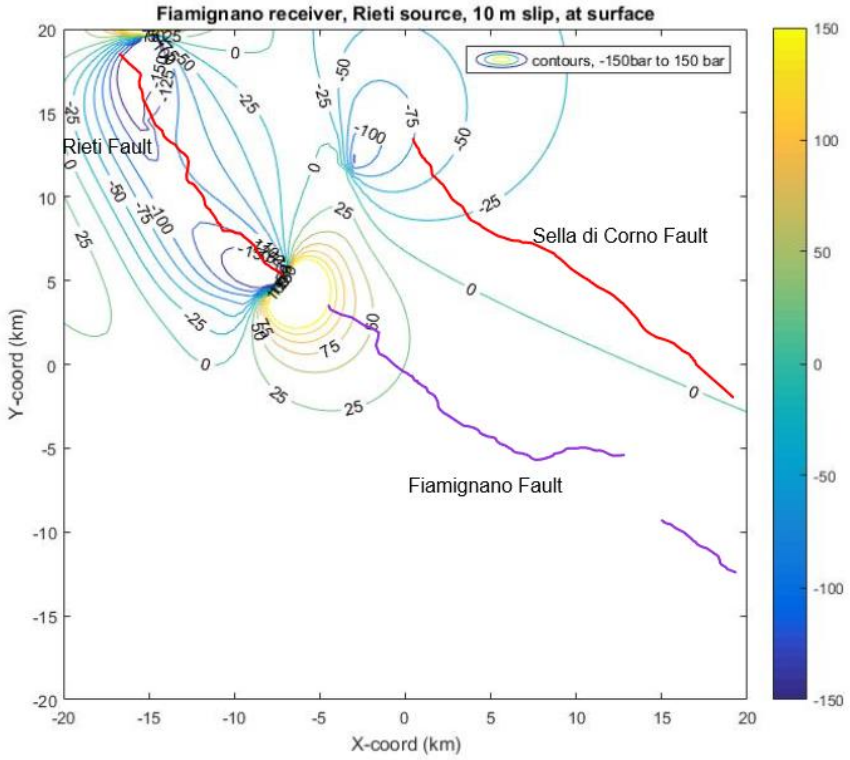

Figure 62 *Coulomb Stress model output for Rieti (source) and Fiamignano (receiver) faults, at 0.1 km depth (surface) shown as a stress contour map superimposed upon the Abruzzo GE .kml file traces for those faults.*

5.2.4 Fiamignano fault as combined source and receiver fault segments

An alternative approach to modelling Coulomb Stress transfer is to treat the Fiamignano fault as a combination of source fault segments at a strike of ~310^{o}, and linking segments as being receiver faults in the form of possibly reactivated existing structures which then provide hard links to the tips of the segments as receivers. As part of the trace is missing in the Abruzzo GE .kml file traces (towards the SE) this is difficult to model over the whole fault. However, a model of 4 contiguous segments (from NW) of source segment A, 3 km at 310^{o} strike, receiver fault B, 1.5 km at 0^{o} strike, source segment C, 14 km at 310^{o} strike, and receiver fault D, 3 km at 270^{o} strike approximates to the Abruzzo GE .kml file trace up to the "missing gap". The angle between source and receiver fault strike is 40^{o}/40^{o} (mean 40^{o}) in both cases (between A and B, and C and D). The underlap between A and C is ~0.96 km, the separation ~1.15 km. The underlap between C and the tip of D (and the assumed start of another strike-parallel segment) is ~1.92 km, the separation ~1.61 km.

In this model the tips of source and receiver faults are assumed to be contiguous, in the absence of evidence of overlap on the ground. Slip is assumed to be proportionate to slip on the whole fault (18.2 m over length of 27.2 km), and therefore 2 m on source fault segment A, and 9.1 m on source fault segment C. The change in Coulomb shear stress for each is modelled separately. The same parameters for regional stress are applied as described in 5.1 above. The result at 15 ka for A (representing 6.27 Mw of stress transfer) is **Figure 63**, and for C (7.15 Mw) is **Figure 64.** Fault depth is shown as 4 km.

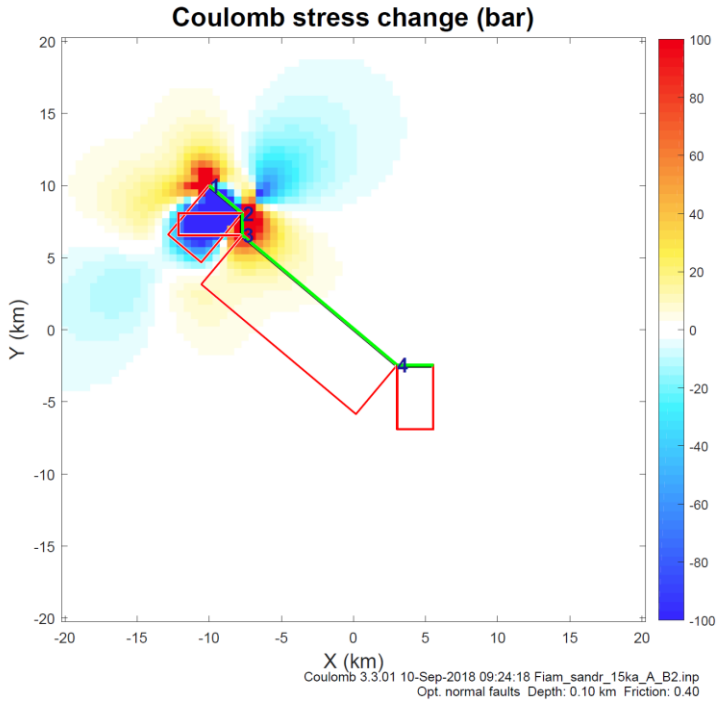

Figure 63 *Coulomb Stress model output for Fiamignano A (source) (1) and Fiamignano B, C and D (receiver) (2 to 4) faults, at 0.1 km depth (surface) at 15 ka.*

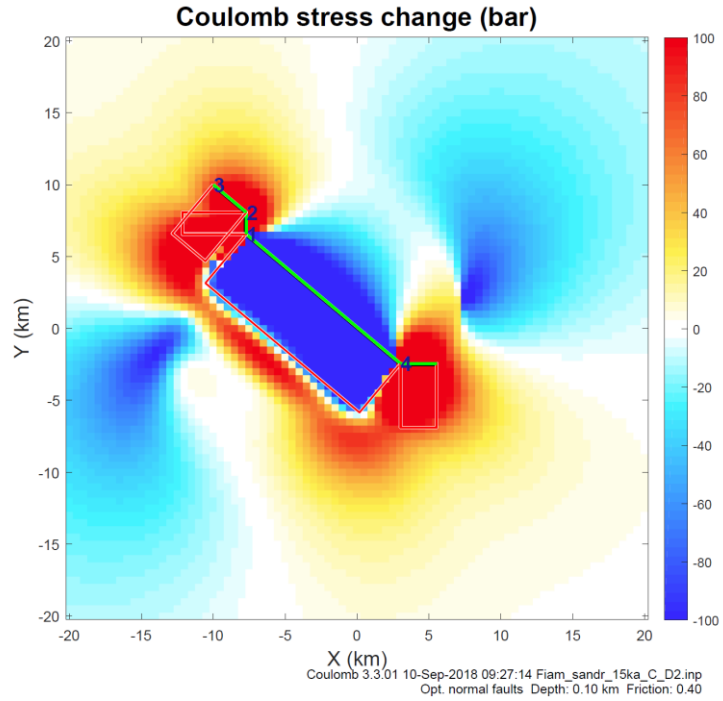

Figure 64 *Coulomb Stress model output for Fiamignano C (source) (1) and Fiamignano D (4), B and A (receiver) (2 and 3) faults, at 0.1 km depth (surface) at 15 ka.*

At the surface, a positive change in Coulomb shear stress of ~100 bar is seen from A to B, and from C to both B and D.

5.2.5 Summary and possible interpretation of results for Fiamignano

The Fiamignano fault has an overall bearing of ~310^{o} (very close to the average strike of the 28 faults of 311^{o}). The overall bearing is the result of a series of clockwise and anticlockwise deviations, which effectively cancel each other out over the length of the fault, but which give the fault trace an overall high sinuosity value. As a potential source fault, the Sella di Corno fault does not cause a positive Coulomb shear stress change >50 bar over the course of 15 ka. The Rieti fault does, but only over the last ~4 km of the fault at its NW tip. That section includes part where the strike is ~310^{o} (at the far NW, where the change is ~75-100 bar), and a section where the strike rotates clockwise towards ~010^{o} (further SE where the change is lower, but still >50 bar). It is possible that the change in strike at that point is the result of reactivation of a pre-existing structure trending NNE-SSW caused by movement on the Rieti fault over time, or by the reactivation of along strike parallel segments (which in turn reactivate pre-existing structures trending NNE-SSW).

If the Fiamignano fault is considered as a series of source fault segments at ~310^{o}, with "receiving" linkages between the source segments, then (considering the NW half of the fault), the positive Coulomb shear stress change on each of the 2 receiving linkages exceeds ~80 bar. The angle between source segment strike and receiving fault strike is ~40^{o} in both cases. This would suggest that the receiving faults in both cases are hard linkages in the form of fault bends (following Hodge et al, 2018), with the possible trigger for initial movement of the segment furthest to the NW coming from movement on the parallel, along strike Rieti fault (ibid). Therefore, the overall sinuosity of the fault may arise from the hard linkages between fault segments in the form of fault bends.

5.3 Magnola

5.3.1 Geometry of Magnola fault

The Abruzzo GE .kml file trace for the Magnola fault shows little sinuosity along most of its initial length (from the NW end). From roughly the midpoint, however, there are noticeable changes in strike from ~290^{o} to ~270^{o}, back to ~290^{o}, reverting to ~270^{o}, then 250^{o} and eventually changing to ~310^{o} towards the SE end. These changes result in the high sinuosity values recorded for the projected traces of 1.143 (A) and (in particular)

1.337 (B). The latter incorporates the clockwise change of strike from ~270° to ~310°. The Abruzzo GE .kml file trace appears at **Figure 65**, the projected traces at **Figure 66.**

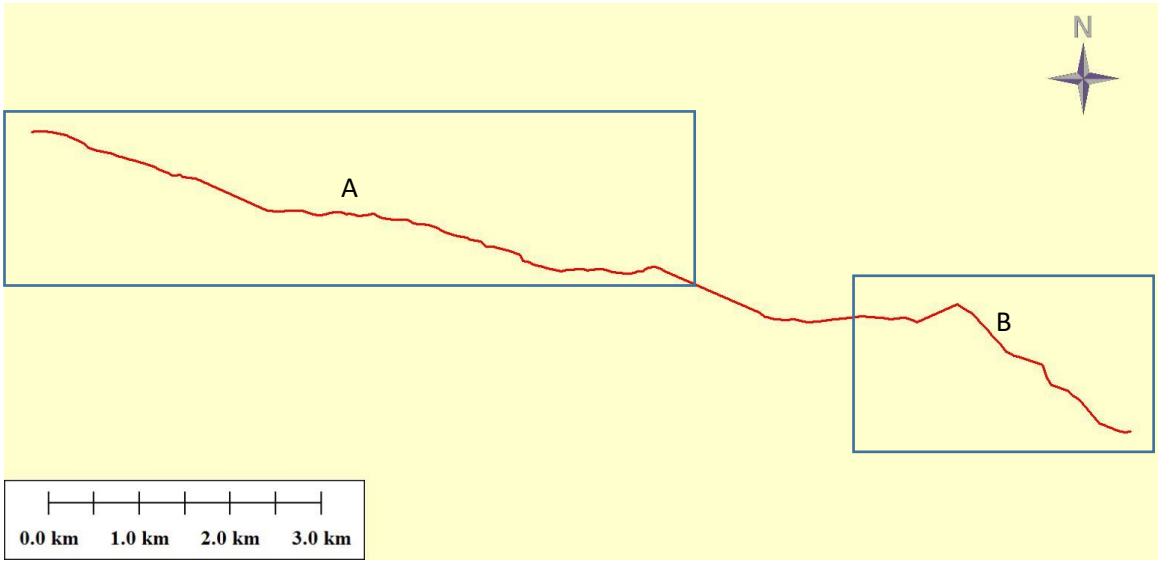

Figure 65 *Map view Abruzzo GE .kml file fault trace profile for Magnola fault, boxes showing areas covered by projected traces in Figure 66 below.*

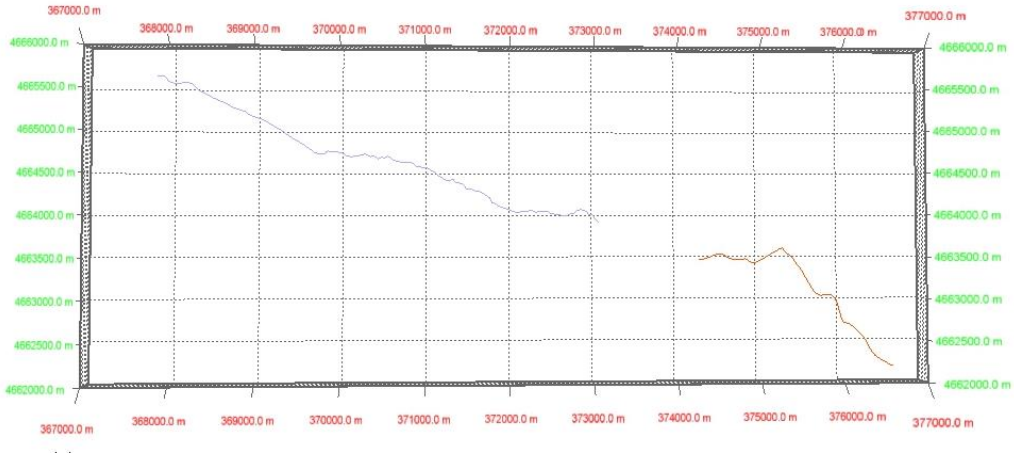

Figure 66 *Google Earth fault trace profile for Magnola fault (projected in MOVE).*

The Magnola fault is unusual, regionally, in having an overall strike of 290°. The source faults for the Magnola fault are at this point more typical of regional trends (nearer 311°). Those are Fucino (up-dip from Magnola to the NE, overall strike of the segment modelled 322°) and Magliano (down-dip to the SW, overall strike 310°). Fucino has the greater slip over 15 ka (15 m) compare to Magliano's 8.6 m.

At 15 ka, the total seismic moments calculated are 7.36 Mw (Fucino), and 7.11 Mw (Magliano). A more detailed description of the changes in Coulomb shear stress over time and applying different models of fault growth is in **Appendix G**.

5.3.2 Fucino fault as source fault to Magnola

The Fucino fault's influence on the Magnola fault in Coulomb shear stress change is predominantly negative. However, at the NW end of the Fucino fault over time there is an increasing degree of positive change in Coulomb shear stress at the surface which reaches ~50 bar at the 12-15 ka stage. The SE end of the Magnola fault only experiences negative change in Coulomb shear stress from slippage on the Fucino fault. A tapered model of the source fault shows greater positive stress transfer (~75-100 bar) across a wider area of the NW end of the receiver fault. The non-tapered model of the position at the surface at 15 ka is shown at **Figure 67.** At depth, there is only negative change in Coulomb shear stress.

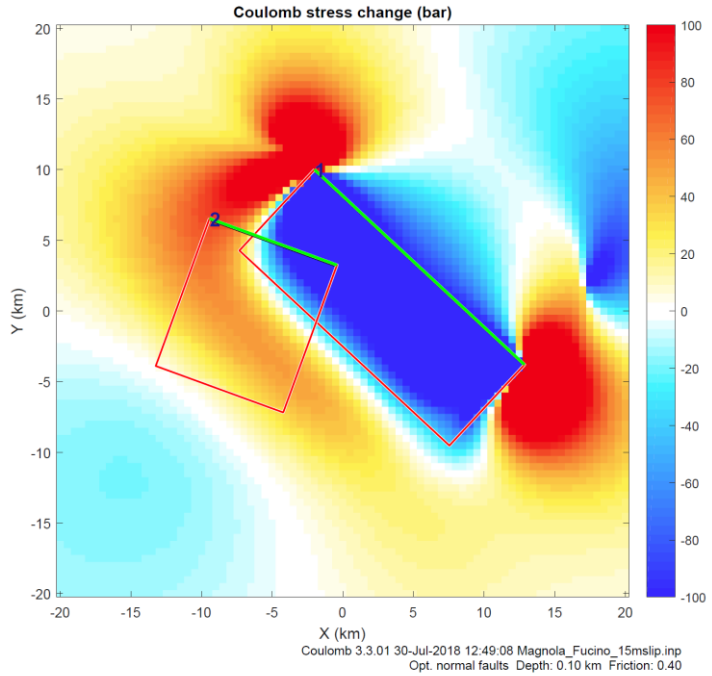

Figure 67 *Coulomb Stress model output for Fucino (source) (1) and Magnola (receiver) (2) faults, variable and constant length models shown at 0.1 km depth (surface), result at 15 ka.*

5.3.3 Magliano fault as source fault to Magnola

When the Magliano fault is modelled as the source fault, positive change in Coulomb shear stress also occurs towards the NW end of the Magnola fault. The separation of the location of the positive change in Coulomb shear stress varies with time on the variable model, but approaches ~50 bar at the surface from an early stage. On the constant length model, the position remains static, with the amount of change in Coulomb shear stress increasing over time. On both models, the result at 15 ka is positive change in Coulomb

shear stress of ~50 bar at the surface (**Figure 68**), just to the NW of the centre of the fault. **Figure 69** shows the result as a stress contour map superimposed upon the Abruzzo GE .kml file traces. A tapered model of the source fault produces a higher positive change in Coulomb shear stress at 15ka (~75-100 bar) over a wider area.

The positive change in Coulomb shear stress at the surface is coupled with positive change in Coulomb shear stress at depth.

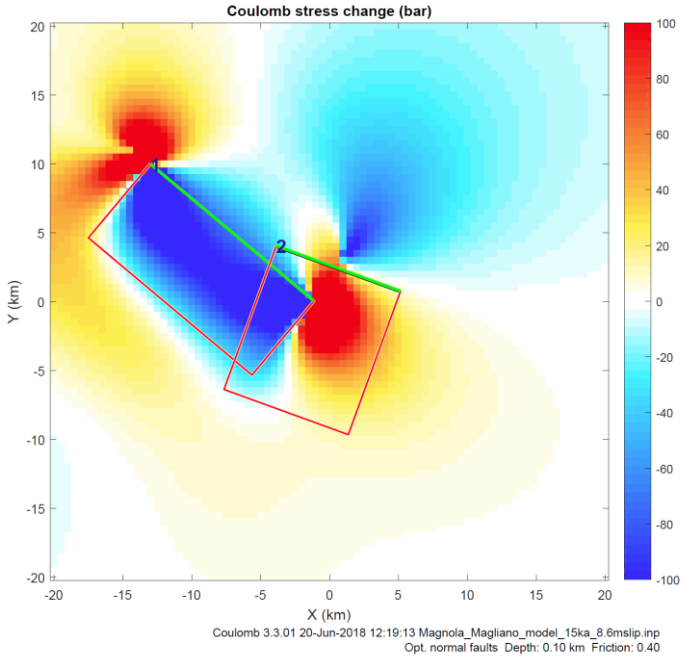

Figure 68 *Coulomb Stress model output for Magliano (source) (1) and Magnola (receiver) (2) faults, variable and constant length models shown at 0.1 km depth (surface), result at 15 ka.*

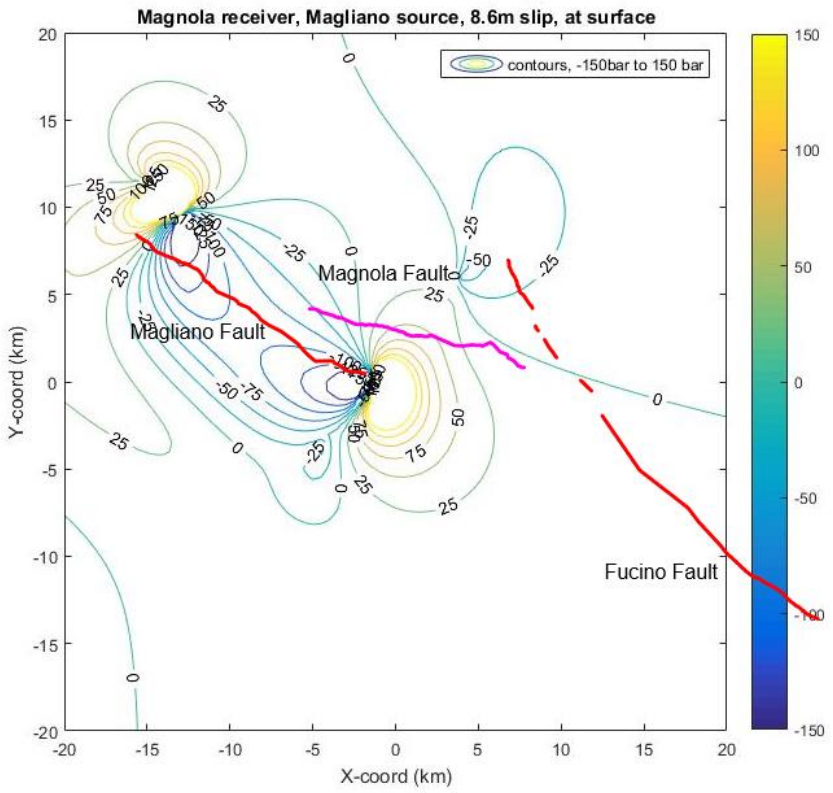

Figure 69 *Coulomb Stress model output for Magliano (source) and Magnola (receiver) faults, at 0.1 km depth (surface) shown as a stress contour map superimposed upon the Abruzzo GE .kml file traces for those faults.*

5.3.4 Combined effect of Magliano and Fucino source faults

At the surface, the faults are not linked. At depth, given the relatively narrow separation between them, it may be that the faults are linked, and the Magnola fault could therefore be a hard linkage between the source faults (Fucino and Magliano). Its geometry would suggest that it might be a breached relay ramp, possibly a reactivated feature from a pre-existing structure. If so, then the tips of the fault overlap, and the Magnola fault tips would not join to those tips.

The degree of overlap between the faults is not easily measured, as it is likely to depend upon the shape of the fault at depth. On the surface, the overlap between the tips of the Fucino and Magliano faults is ~0 km (± 2 km), and the separation ~8-10 km . Both overlap and separation are difficult to assess accurately because of the geometries and variations involved.

Although not separately modelled, the combined effect of the positive change in Coulomb shear stress from Fucino and Magliano could be ≥ 100 bar positive change in Coulomb

shear stress from the towards the NW end of the Magnola Fault, to beyond the half way point (the end of the positive change in Coulomb shear stress in excess of 50 bar possibly coincides with the change in strike at the SE end from ~270^{o} to ~310^{o}). However, the combined effect of the two changes in Coulomb shear stress requires more knowledge of actual slip histories, and more complicated modelling than is attempted in this study.

5.3.5 Summary and possible interpetation of results for Magnola

Two features stand out on first review of the Magnola fault traces. First, the overall strike of ~290^{o} is ~20^{o} anticlockwise from the regional norm (310^{o}). Second, although much of the traces show relatively little sinuosity, the high sinuosity value of 1.337 for the Magnola B trace is the result of a significant shift of strike clockwise of ~40-60^{o}, ending with a strike at the SE tip which matches the local norm.

Modelling neighbouring faults as source faults, the Fucino fault is the source of positive Coulomb shear stress change on the Magnola fault of ~50-75 bar over ~4 km at its NW end, but only when slip has fully accumulated. The highest values of positive Coulomb shear stress change occur towards the centre of the fault. The remainder of Coulomb shear stress change resulting from movement on the Fucino fault is negative (as it is at depth). The Magliano fault also imparts positive Coulomb shear stress change of ~50 bar at the area around the centre of the fault (but only extending ~1 km).

At the surface, the three faults do not appear to be linked. However, the map view configuration of the faults (**Figure 69**) would suggest that there is a link at depth from the Magnola fault to the others, by way of a developing breached ramp which does not connect with the fault tips of the other faults. The Fucino and Magliano fault over/underlap by some ~0 km ±2 km, with a separation of ~8-10 km (they are not parallel, so the calculations are inexact). It is also not easy to calculate the degree of difference between the receiving and source fault strikes (α, in Hodge et al, 2018) with accuracy, as the strikes change. One possible assessment of the geometry is that the NW section of the Fucino fault closest to the Magnola fault has a strike of ~335^{o}, the Magnola fault (other than the far SE end) has a strike of ~284^{o}, and the SE section of the Magliano fault has a strike of ~318^{o}, giving α values of respectively 51^{o} and 34^{o} (mean 43^{o}). With separation exceeding overlap, and an α value of ~45^{o}, the result would fit within the modelled preferred link geometry of a breached relay ramp from Hodge et al (2018). This

could take the form of either a new structure, or a reactivated older structure as result of positive Coulomb shear stress change resulting from movement on the neighbouring source faults.

This would leave unexplained the divergence seen at the far SE tip of the Magnola fault. However, as that follows the regional norm for fault strike, and is beyond the modelled area of positive Coulomb shear stress change, a possible explanation is that it is a shorter fault segment in line with the current regional extensional regime, essentially parallel to the neighbouring larger faults, to which the relay ramp has now linked. The sinuosity value of the trace could therefore be a result of the joinder of two separate structures resulting from different extensional regimes.

5.4 Parasano

5.4.1 Geometry of Parasano fault

The Abruzzo GE .kml file traces for the Parasano Fault are not continuous, reflecting what appear to be linkages at depth between fault segments which are less obvious at surface level, and several changes in strike between those segments. Two segments include sections with a strike of ~320^{o} (C and F). Three others are at ~280-290^{o} (A, B, and D, plus the remainder of C). An intermediate segment (E) has a strike of ~310^{o}. Individually, the sinuosity values of the projected traces are not exceptional (ranging from 1.038 (B) to 1.105 (C)). However, the change in strike between the segments shows more variability. The Abruzzo GE .kml file traces are shown in **Figure 70** below, and the projected traces in **Figure 71.**

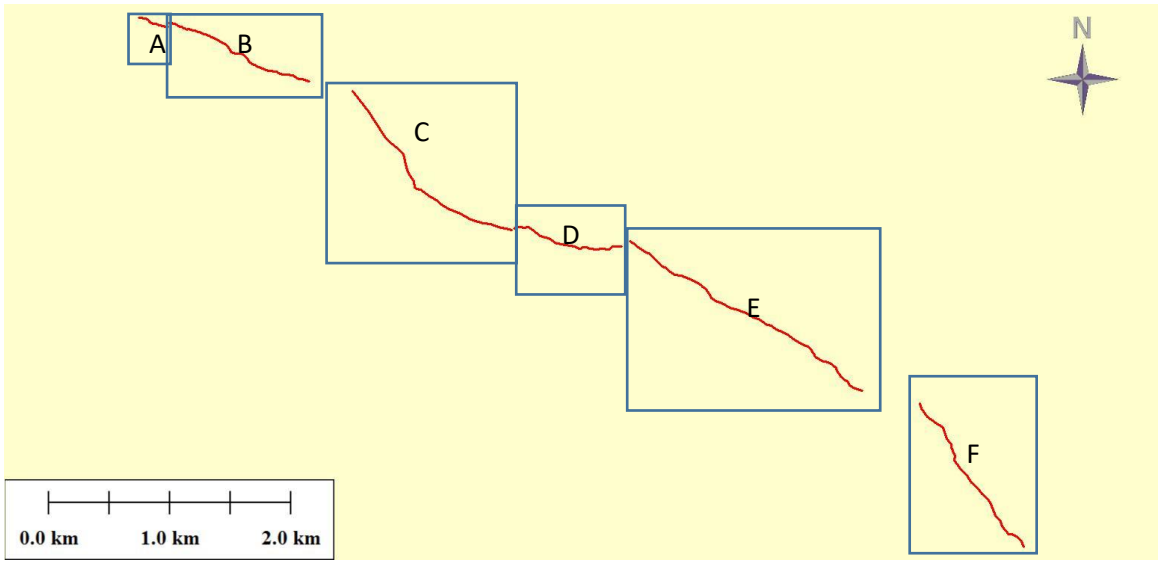

Figure 70 *Map view Abruzzo GE .kml file fault trace profile for Parasano fault, boxes showing areas covered by projected traces in Figure 71 below.*

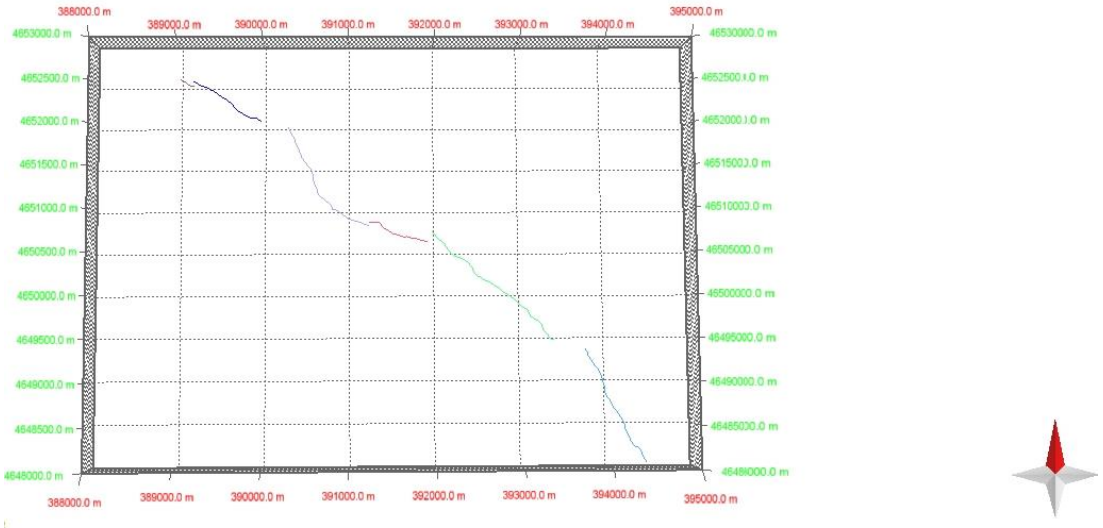

Figure 71 *Google Earth fault trace profile for Parasano fault (projected in MOVE).*

Two primary source faults are modelled for the Parasano Fault, Fucino and San Sebastiano. Both are considerably longer faults than the Parasano Fault. The Fucino fault shows greater slip (15m) than the Parasano fault (4.2m) over the last 15 ka. The Fucino fault is down-dip from the Parasano fault, to the SW. Although the San Sebastiano fault is up-dip, the slip involved is smaller (11.2m).

At 15 ka, the total seismic moments calculated are 7.43 Mw (Fucino), and 6.88 Mw (San Sebastiano). A more detailed description of the changes in Coulomb shear stress over time and applying different models is in **Appendix G**.

5.4.2 Fucino fault as source fault for Parasano

Using a variable length model, a small positive change in Coulomb shear stress from slippage on the Fucino fault is seen at the far SE end of the fault, at surface at 9 ka (<25 bar). However, at 15 ka, there is no positive change in Coulomb shear stress (**Figure 72)**, and there is little variation with depth. The change in Coulomb shear stress from the Fucino fault to the Parasano fault is almost exclusively negative using the constant length model.

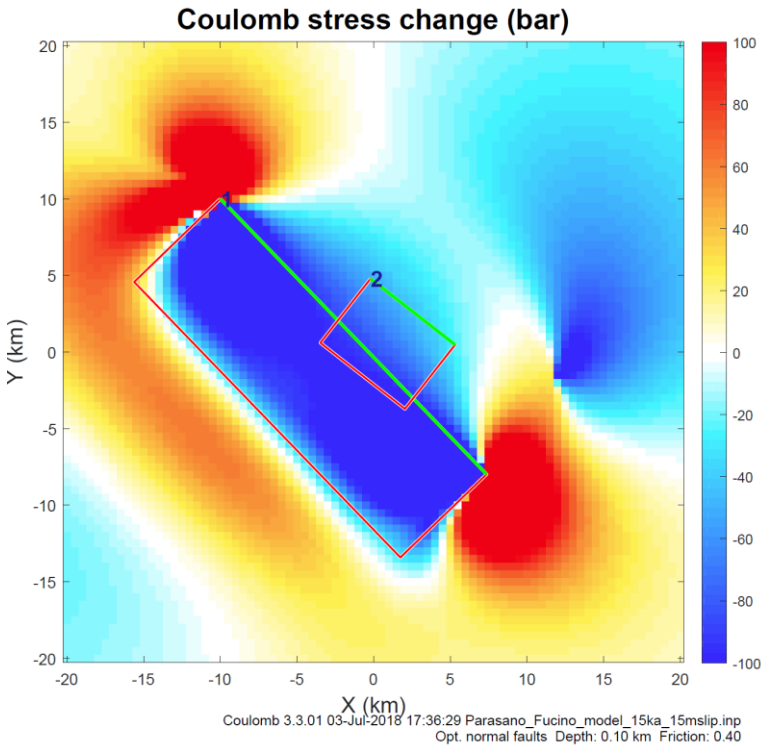

Figure 72 *Coulomb Stress model output for Fucino (source) (1) and Parasano (receiver) (2) faults, variable and constant length models shown at 0.1 km depth (surface), result at 15 ka.*

5.4.3 San Sebastiano fault as source fault for Parasano

Modelling the San Sebastiano fault as the source fault, by 12 ka there is a positive change in Coulomb shear stress at the surface towards the centre of the Parasano fault approaching 25-30 bar.

At 15 ka the positive change in Coulomb shear stress at the surface in the middle section of the fault is ~40-50 bar (**Figure 73**), with negative change in Coulomb shear stress towards the SE. Using a tapered model eliminates the negative change at the SE, and reduces the degree of positive change in Coulomb shear stress. There is relatively little

change in Coulomb shear stress at depth, with a small amount of positive change to the NW end of the fault, and negative change to the SE end.

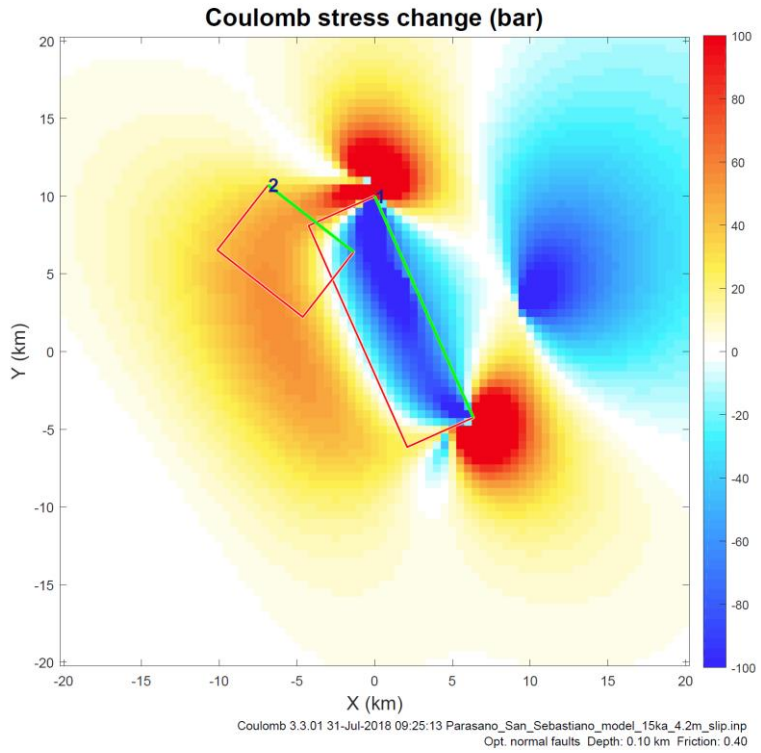

Figure 73 *Coulomb Stress model output for San Sebastiano (source) (1) and Parasano (receiver) (2) faults, variable and constant length models shown at 0.1 km depth (surface), result at 15 ka.*

Superimposing a stress contour map of the Coulomb Stress model results upon the Abruzzo GE .kml file traces (**Figure 74** below) shows the sensitivity of the modelling to the positioning of the NW end of the source fault. The model has been run using the "main" body of the San Sebastiano fault as the source, and not the shorter, more isolated segments to the NW. If those had been included in the model, any change in Coulomb shear stress would have been limited to the far NW end of the Parasano fault, and at a lower value than shown.

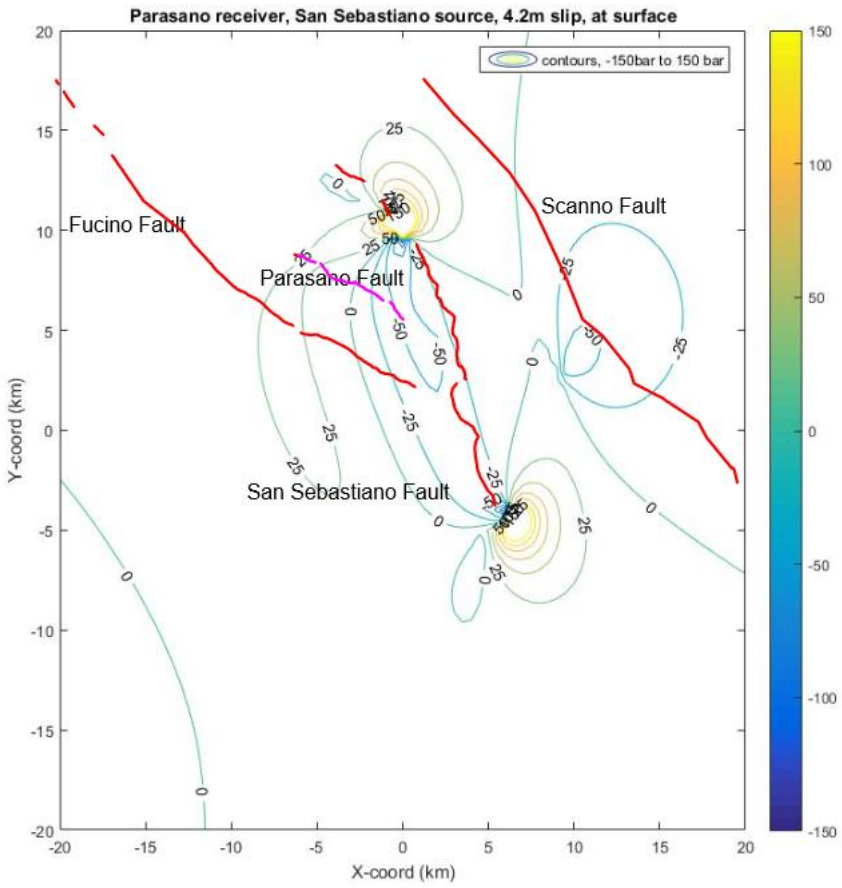

Figure 74 *Coulomb Stress model output for San Sebastiano (source) and Parasano (receiver) faults, at 0.1 km depth (surface) shown as a stress contour map superimposed upon the Abruzzo GE .kml file traces for those faults.*

5.4.4. Parasano fault as source and receiver fault segments

As noted above, the fault traces show a number of changes in strike. One of these, the anticlockwise change from ~320^{o} to ~280^{o}and subsequent clockwise change back to ~310^{o} between the segments labelled C, D and E in **Figure 70** above has been identified by Faure Walker et al, 2009 as a breached relay ramp, with the relay (D and part of C) exhibiting less displacement at the surface than the other segments. The NW tip of segment E overlaps the tip of segment D. Therefore, it is likely that segments C and E have acted as source fault segments for what was probably a pre-existing structure as a receiver fault. This is modelled (from NW) as a source fault segment of 2 km length with strike of 320^{o}, a receiver fault of 0.75 km length bearing 276^{o} and a second source fault segment of 1.5 km length bearing 310^{o}. The source fault segments are modelled separately for the purposes of Coulomb Stress change, assuming a degree of slip proportionate to the slip on the whole fault (7.9m) - for the first source fault this amounts

to 2.8m, for the second 2.1m. Other parameters are as for the other Coulomb Stress models, although fault depth is shown as 4 km.

The results of the modelling show a positive change in Coulomb shear stress to the relay segment (D and part of C) from both the sources segments. **Figure 75** shows the change in Coulomb shear stress at the surface from the C segment ((1) in that figure), at 15 ka, and **Figure 76** the change in Coulomb shear stress from the E segment ((1) in that figure), the former being 6.17 Mw in magnitude, the latter 6.01 Mw. In both cases the change in Coulomb shear stress on the whole of the receiver segment ≥ 100 bar.

The underlap between the tips of the source segments is ~0.62 km (although that maybe a maximum, as at least one of the tips extends further, beyond the joining point with the relay). The separation is ~0.42 km. The angles between the relay and the respective source segments (α) (as identified in Hodge et al, 2018, see 2.6 above) are ~34°/44° (mean 39°).

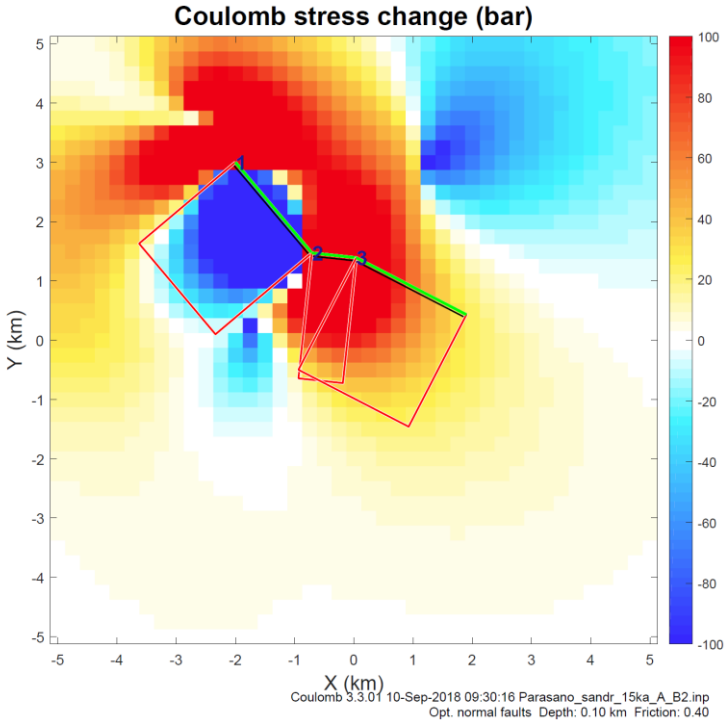

Figure 75 *Coulomb Stress model output for Parasano source fault segment at 320° (1), onto receiver segment at 276° (2), also showing third segment at 310° (modelled as further receiver fault here) (3).*

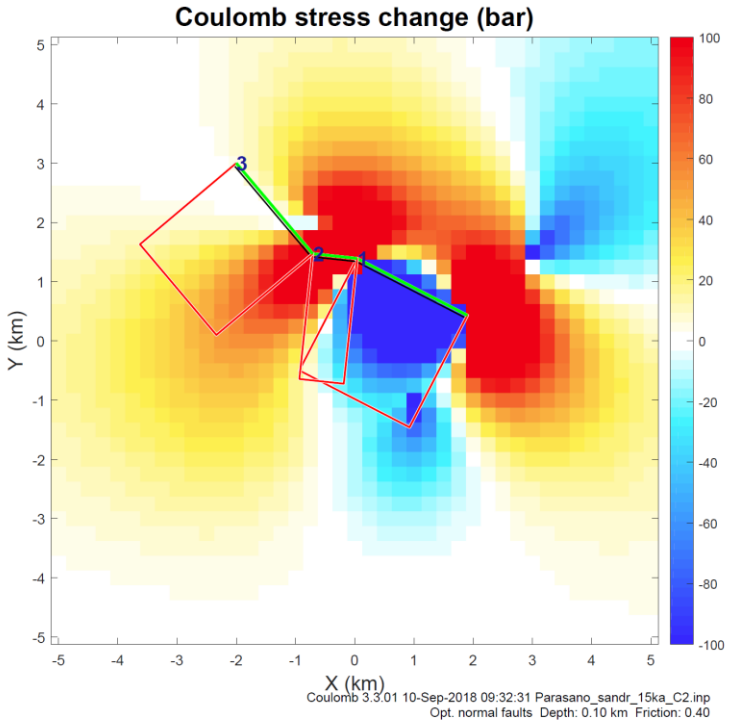

Figure 76 *Coulomb Stress model output for Parasano source fault segment at 310^o (1), onto receiver segment at 276^o (2), also showing third segment at 320^o (modelled as further receiver fault here) (3).*

5.4.5 Summary and possible interpretation of results for Parasano

The traces for the Parasano fault seen at the surface are not continuous, and exhibit a number of changes of strike. The sinuosity values for the traces may not be a proper reflection of the sinuosity of the fault as a whole, as there are changes in strike between the sections (such as between B and C, and between D and E in **Figure 70**) which are not counted for sinuosity purposes (as the traces are not continuous). The overall effect is of a fault which is more sinuous than the sum of the fault trace values.

Its geometry compared to its neighbours is also complicated, as it is broadly parallel to the Fucino fault at the point where they overlap (Parasano at ~309^o, Fucino at ~307^o), but significantly different from the San Sebastiano fault (at ~340^o), which effectively cuts across it at its SE end. It is also potentially influenced by slip on the larger Scanno fault, to the NE, beyond San Sebastiano. Models of Coulomb Stress change show no significant positive stress change from movement on the Fucino fault. Although there is some positive Coulomb shear stress transfer change from movement on the San Sebastiano

fault, principally towards the NW end of the Parasano fault (depending substantially on how the model is set up), it does not appear to exceed 50 bar.

If the sections of the Parasano fault which have a bearing of ~130-140^{o} are modelled as source fault segments of 2 and 1.5 km length respectively, and the intervening section as receiver, the model shows positive Coulomb shear stress change of ≥100 bar from each source fault onto the intervening section. This is unsurprising, as that section has already been identified as a breached relay ramp in Faure Walker et el, 2009. However, the result confirms that the sinuosity seen here is likely to be a result of the fault growth through Coulomb shear stress change and activation/reactivation of a linking section.

5.5 San Sebastiano

5.5.1 Geometry of San Sebastiano fault

San Sebastiano fault lies between, and sub-parallel to, 3 neighbouring faults, Scanno (up-dip to the NE), Parasano and Fucino (both down-dip to the SW). San Sebastiano's overall strike is 336^{o}, deviating by 25^{o} clockwise from the regional average strike of 311^{o}. Scanno also differs from the average in a clockwise direction, by 19^{o} (at an overall strike of 330^{o}).

The sinuosity values obtained for the projected traces for San Sebastiano are not among the highest (A = 1.071, B = 1.052, C = 1.101 and D = 1.036). However, a comparison between the Abruzzo GE .kml file trace (**Figure 77**) and projected traces (**Figure 78**), shows that the projected traces do not cover one of the apparently more sinuous part of the trace towards the SE end of the fault, where (from the NW) the trace veers towards a strike of ~020^{o}, then back towards ~320^{o} before resuming its overall bearing.

Trace A has a strike of ~300^{o}, with little variation in strike. Trace B has an overall strike of ~335^{o}, but within that varies between 320^{o} and 360^{o}. Trace C has an overall strike of ~340^{o}, but within that there is regular switching of strike (initially ~310^{o} then ~010^{o}, back to ~350^{o}, then ~360^{o}, ~310^{o} and finally ~360^{o} again). Trace D has an overall strike of ~345^{o}, but starts at ~010^{o}, before changing to ~350^{o} and finishing at a strike of ~330^{o}.

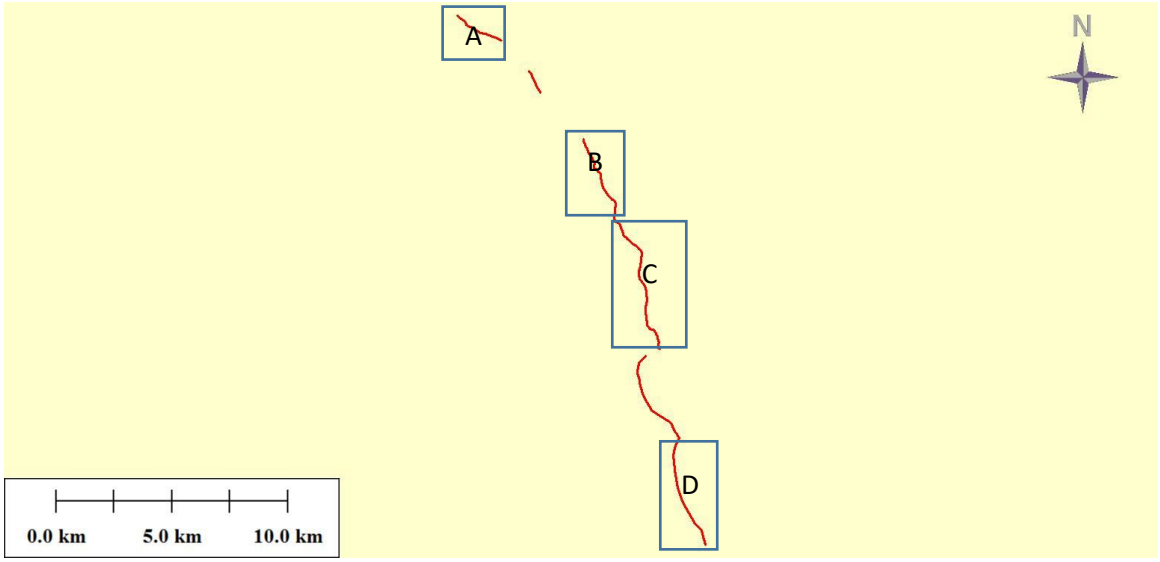

Figure 77 *Map view Abruzzo GE .kml file fault trace profile for San Sebastiano fault, boxes showing areas covered by projected traces in Figure 78 below.*

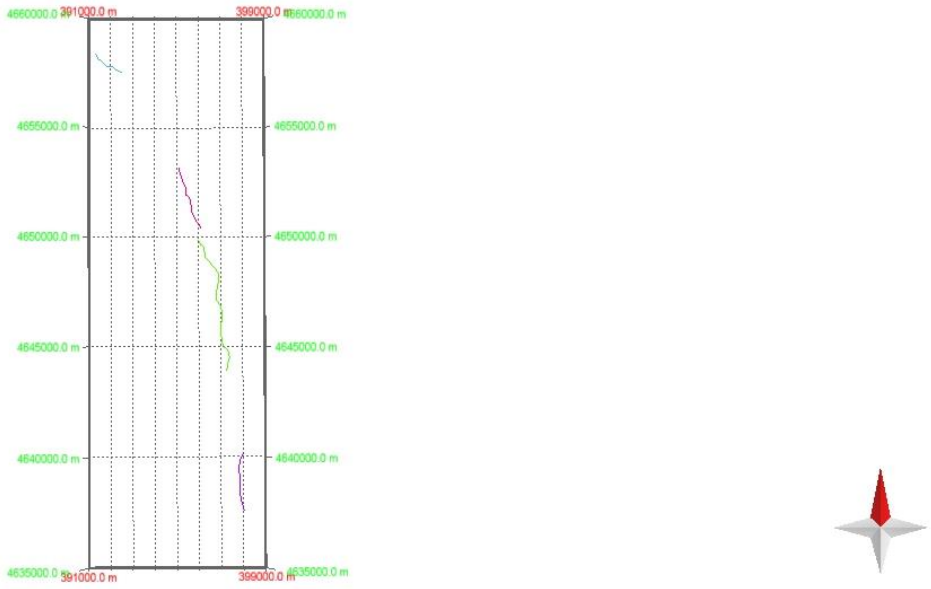

Figure 78 *Google Earth fault trace profile for San Sebastiano fault (projected in MOVE).*

Fucino, Parasano and Scanno faults are modelled as source faults. In the case of Fucino, Parasano is also shown as a receiver fault (2 in the figure below, where San Sebastiano is 3). At 15 ka, the total seismic moments calculated are 7.43 Mw (Fucino), 6.90 Mw (Parasano) and 7.44 Mw (Scanno). A more detailed description of the changes in Coulomb shear stress over time and applying different models is in **Appendix G**.

5.5.2 Fucino fault as source fault for San Sebastiano

When the Fucino fault is modelled as the source fault, a positive change in Coulomb shear stress towards the SE end of the San Sebastiano fault develops relatively quickly (at 6-9 ka). In the case of the variable length model the focus of the principal positive change in Coulomb shear stress migrates towards the SE over time (**Figure 79** shows the position at 15 ka) reaching ~50 bar. Using a tapered source model produces a higher positive change in Coulomb shear stress (~75-100 bar) over an extended area. At depth there is a small amount of positive change in Coulomb shear stress (~10 bar) over a restricted area at the SE end of the fault.

Given the change in strike in the fault traces, rather than the straight lines and uniform strike assumed in the models, superimposition of the stress contour map on the Abruzzo GE .kml file traces (**Figure 80**) suggests that the positive change in Coulomb shear stress may be over a wider area of the fault, and at a greater scale (possibly up to ~75-100 bar at the surface, and ~25 bar at depth). The area covered appears to coincide with the areas of greater sinuosity identified above (Trace C and the "gap" between Traces C and D).

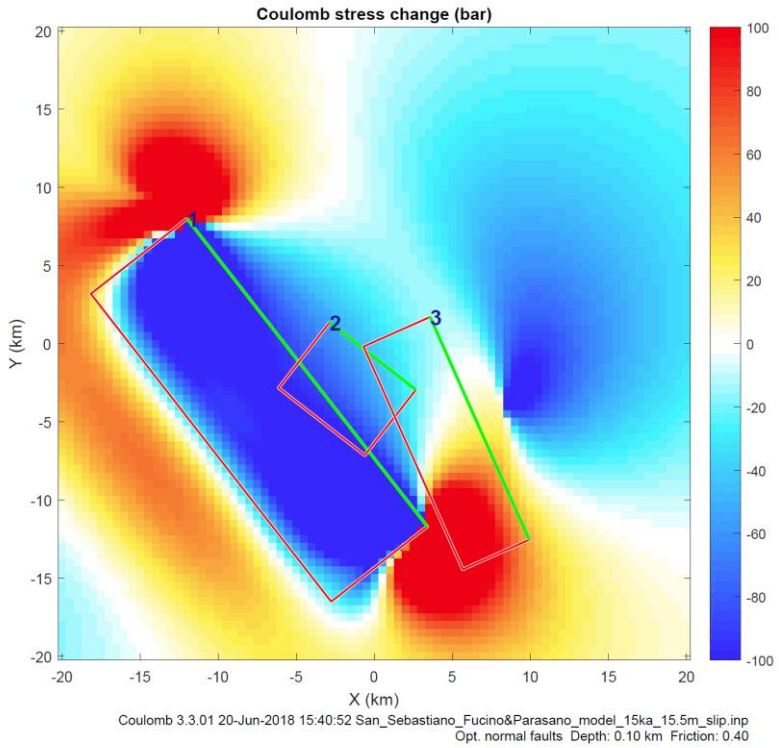

Figure 79 *Coulomb Stress model output for Fucino (source) (1) and San Sebastiano/Parasano (receiver) (2 and 3) faults, variable and constant length models shown at 0.1 km depth (surface), result at 15 ka.*

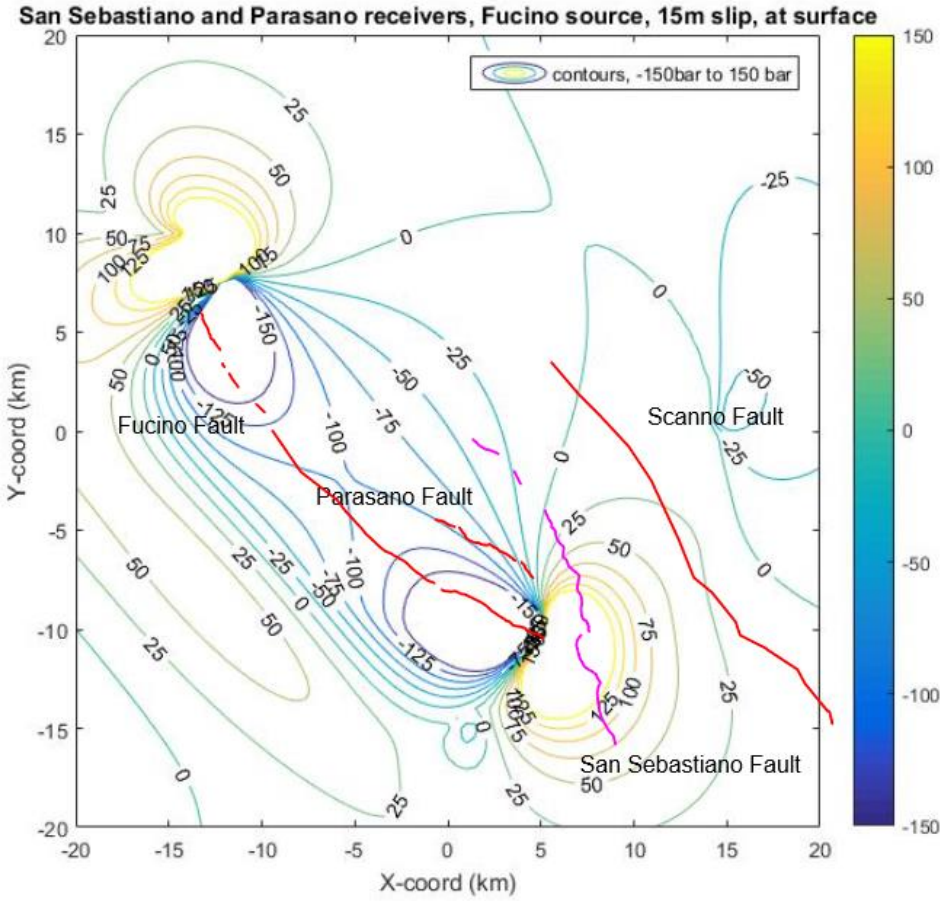

Figure 80 *Coulomb Stress model output for Fucino (source) and San Sebastiano/Parasano (receiver) faults, at 0.1 km depth (surface) shown as a stress contour map superimposed upon the Abruzzo GE .kml file traces for those faults.*

5.5.3 Parasano fault as source fault for San Sebastiano

When the Parasano fault is modelled as the source fault, a positive change in Coulomb shear stress is shown at ~6 ka. The focus of the change in Coulomb shear stress varies slightly depending upon whether the varied length model or constant length model is adopted. The positive change in Coulomb shear stress at the surface is ~25 bar at that stage, towards the NW from the middle point of the fault. At 15 ka the positive change in Coulomb shear stress at surface is ~100 bars (**Figure 81**), covering most of the NW half of the San Sebastiano fault. Using a tapered model for the source fault (Parasano) increases the scale and extent of the positive change in Coulomb shear stress, so that the NW half of the San Sebastiano fault experiences a positive change in Coulomb shear stress in

excess of ~ 100 bar. At depth (5 km) the change in Coulomb shear stress is mainly negative.

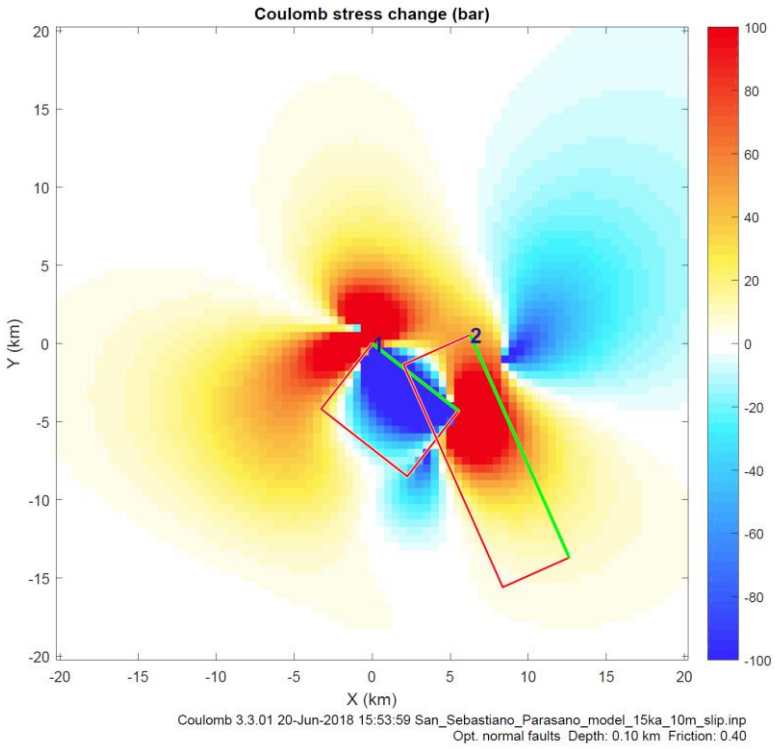

Figure 81 *Coulomb Stress model output for Parasano (source)(1) and San Sebastiano (receiver) (2) faults, variable and constant length models shown at 0.1 km depth (surface), result at 15 ka.*

5.5.4 Scanno fault as source fault for San Sebastiano

Modelling the Scanno fault as the source fault shows relatively little positive change in Coulomb shear stress on the San Sebastiano fault. On the variable length model (but not on the constant length model), a small amount of positive change in Coulomb shear stress (~10 bar) is seen at the surface at ~6 ka towards the NW end of the fault (the positioning depends upon the modelling of how the fault grows over time). However, by 15 ka, the change in Coulomb shear stress both at the surface and at 5 km depth is negative – see **Figure 82** (surface)**.**

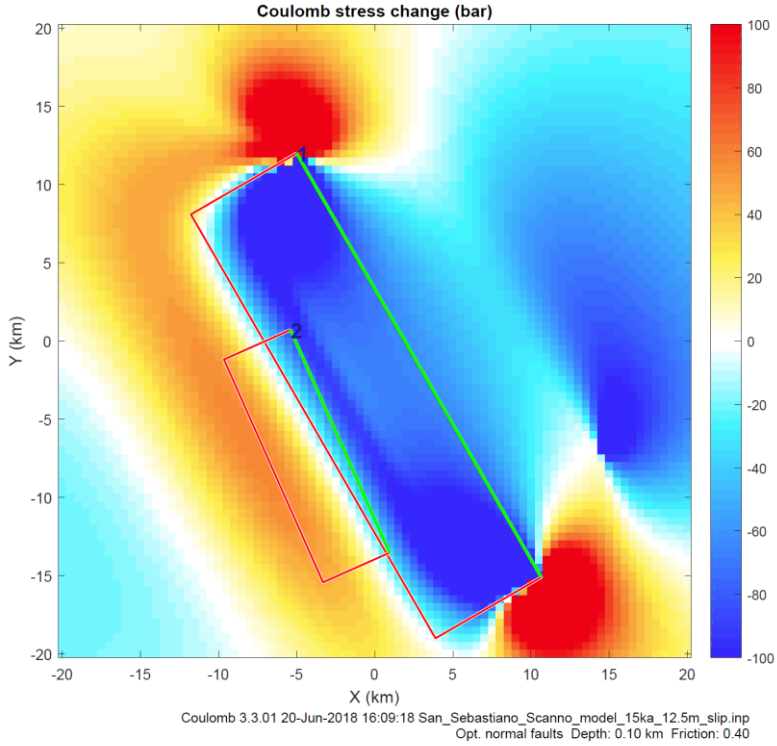

Figure 82 *Coulomb Stress model output for Scanno (source) (1) and San Sebastiano (receiver) (2) faults, variable and constant length models shown at 0.1 km depth (surface), result at 15 ka.*

5.5.5 Summary and possible interpretation of results for San Sebastiano

As with Parasano, San Sebastiano's trace sinuosity values do not full reflect its complexity. Some of the more pronounced changes of strike are not recorded in the traces picked. It is also geometrically located between a number of neighbouring faults (notably Scanno and Parasano) which have rather different overall strikes (San Sebastiano's strike overall is ~340^{o}) (see **Figure 80**).

The Coulomb stress models for San Sebastiano show positive Coulomb shear stress change from movement on the Fucino fault possible exceeding 100 bar towards the centre to SE end of the San Sebastiano fault (the area where there is greatest deviation within the San Sebastiano trace). Modelling Parasano as the source fault yields positive Coulomb shear stress change of ~100 bar, covering most of the NW section of the San Sebastiano fault. Scanno, however, is not a source of significant positive stress change, except some possible change of ~20 bar at the NW end of the San Sebastiano, which could conceivably act together with the effect of slippage on the Parasano fault (depending upon how and when slip actually occurred over 15 ka).

An explanation for the deviation of the San Sebastiano fault from regional norms of strike, and its comparatively convoluted changes in strike may lie in its being subjected to differing sources of positive Coulomb shear stress change at opposite ends. There may be a suggestion from the fault traces of some fault bend linkage between segments within traces B and C. However, given the many changes of strike even within those traces, this has not been modelled here.

5.6 Tre Monti

5.6.1 Geometry of Tre Monti fault

The strike of the Tre Monti fault is unusual, regionally, being ~248^{o} overall. As **Figure 83** below (Abruzzo GE .kml file traces) shows, within that overall figure, there are significant changes of strike. Within segments C and D, and between segments D/E and E/F strikes of ~270-280^{o} are interspersed with strikes nearer to ~240^{o}. Overall, the picture is of considerable variability, and that is also borne out by the sinuosity values obtained using the projections in MOVE (**Figure 84**) which are respectively A = 1.038, B = 1.014, C = 1.097, D = 1.160, E = 1.233, and F = 1.064. As noted at paragraph 4.1 above, this represents the biggest variation in sinuosity figures among the faults studied.

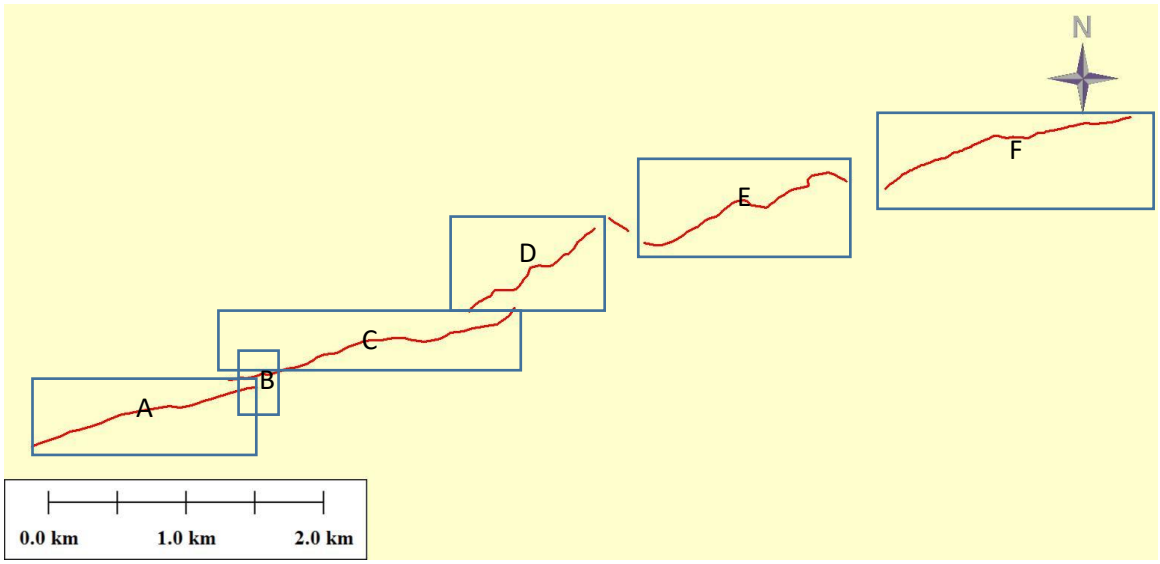

Figure 83 *Map view Abruzzo GE .kml file fault trace profile for Tre Monti fault, boxes showing areas covered by projected traces in Figure 84 below*

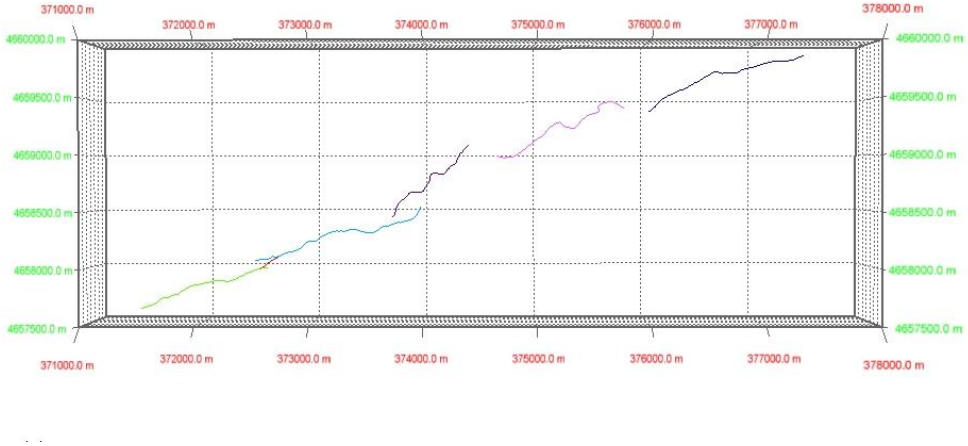

Figure 84 *Google Earth fault trace profile for Tre Monti fault (projected in MOVE).*

Three source faults are modelled for Tre Monti. The Fucino fault is obliquely up dip of the Tre Monti fault, to the NE. The Magliano fault is obliquely up dip to the NW. The Magnola fault is more directly up dip, to the N.

At 15 ka, the total seismic moments calculated are 7.37 Mw (Fucino), 7.11 Mw (Magliano) and 7.12 (Magnola). A more detailed description of the changes in Coulomb shear stress over time and applying different models is in **Appendix G**.

5.6.2 Fucino fault as source fault for Tre Monti

With the Fucino fault modelled as source, a positive change in Coulomb shear stress on the Tre Monti fault at the surface starts at ~6 ka on both the variable and constant length models, with the far W end of the Tre Monti fault experiencing a positive change in Coulomb shear stress of ~25 bar, increasing to ~30-40 bar at 15 ka (**Figure 85**). Using a tapered model produces a result of greater change in Coulomb shear stress approaching ~80 bar at the surface, over a wider spread area (but still confined to the far W of the Tre Monti fault). Other parts of the fault experience a negative change in Coulomb shear stress. At depth (5 km) the position is exclusively negative.

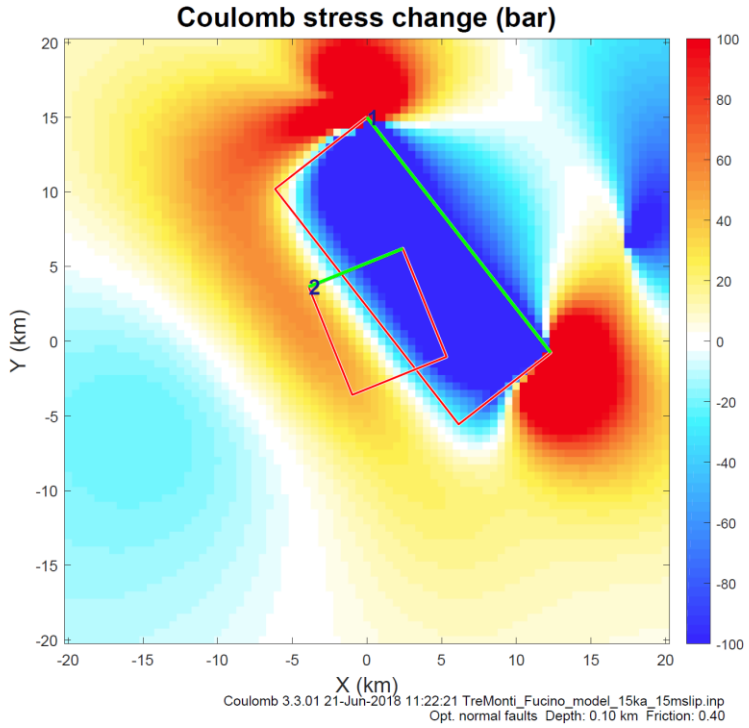

Figure 85 *Coulomb Stress model output for Fucino (source) (1) and Tre Monti (receiver) (2) faults, variable and constant length models shown at 0.1 km depth (surface), result at 15 ka.*

5.6.3 Magliano fault as source fault for Tre Monti

The variable length model for the Magliano fault as the source fault produces a positive change in Coulomb shear stress of ~20 bar at the surface towards the W end of the Tre Monti fault from ~9 ka. The constant length model produces a higher result (~40 bar) over a wider area, and the area of positive change in Coulomb shear stress extends beyond the centre point of the fault. By 15 ka the change in Coulomb shear stress on the Tre Monti fault is entirely positive (**Figure 86**), although only the W end of the fault experiences a positive change in Coulomb shear stress above ~50 bar. At depth, the change in Coulomb shear stress at 15 ka is also positive, although with lower values, confined to a smaller area to the far W of the Tre Monti fault.

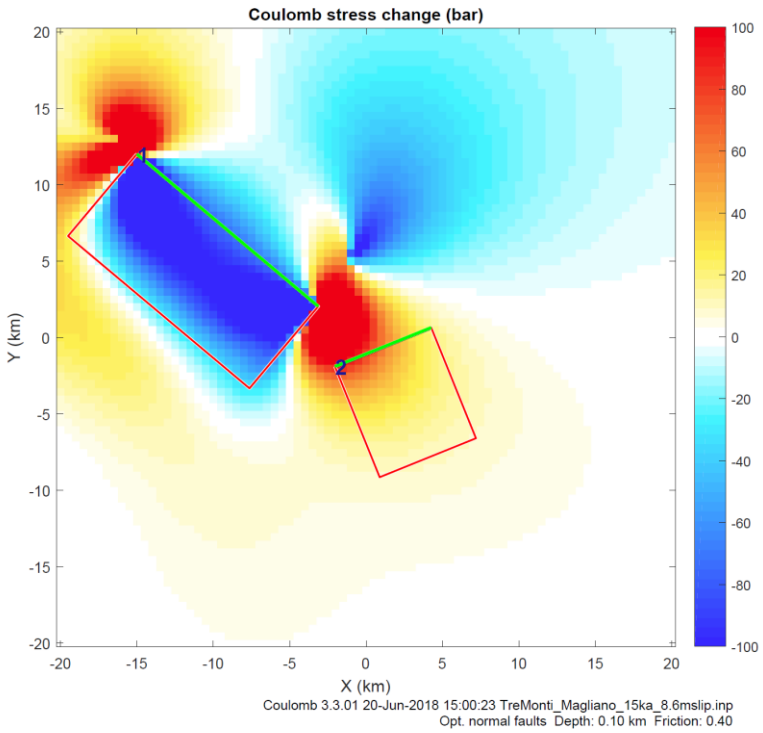

Figure 86 *Coulomb Stress model output for Magliano (source) (1) and Tre Monti (receiver) (2) faults, variable and constant length models shown at 0.1 km depth (surface), result at 15 ka.*

5.6.4 Magnola fault as source fault for Tre Monti

Using the Magnola fault as the source fault, the model shows positive change in Coulomb shear stress at the E end of the Tre Monti fault, starting to be significant at ~6 ka. The variable length model at the surface produces positive values of ~20 bar at the E half of the fault. The constant length model produces a higher result (up to ~40-50 bar) over a similar area. In both cases, the W end of the fault experiences a negative change in Coulomb shear stress. At 15 ka, at the surface, the divergence between the respective ends of the fault is more marked, with the E end experiencing a positive change in Coulomb shear stress in excess of 100 bar, and the W end similar values for negative stress (**Figure 87**). A tapered source fault model produces slightly higher values of positive change in Coulomb shear stress. At depth (5 km) the change in Coulomb shear stress is positive across the fault (biased slightly towards the W end), with values exceeding ~75 bars W from the mid-point of the Tre Monti fault.

The discrepancy between E and W ends of the Tre Monti fault can be seen clearly superimposing the stress contour map onto the Abruzzo GE .kml file traces (**Figure 88**).

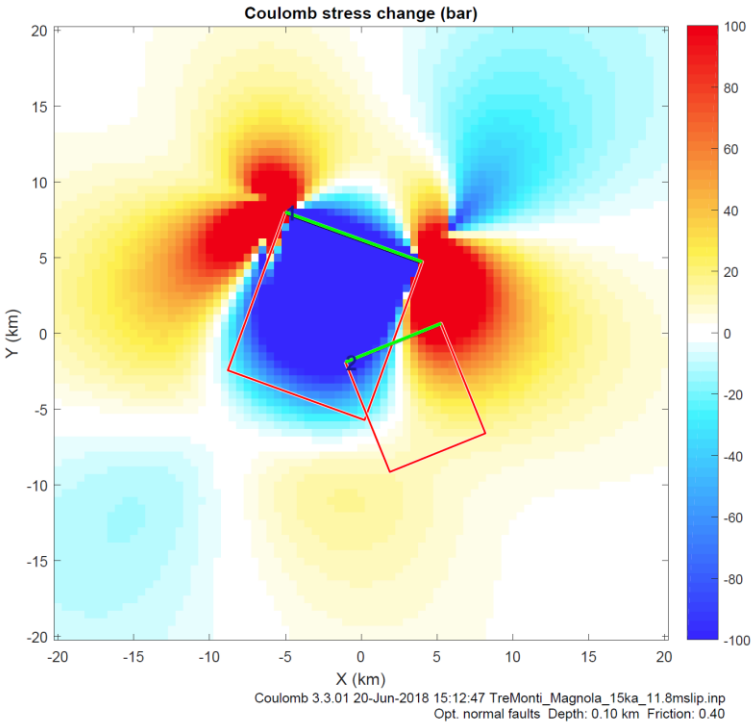

Figure 87 *Coulomb Stress model output for Magnola (source) (1) and Tre Monti (receiver) (2) faults constant and variable length models shown at 0.1 km depth (surface), result at 15ka.*

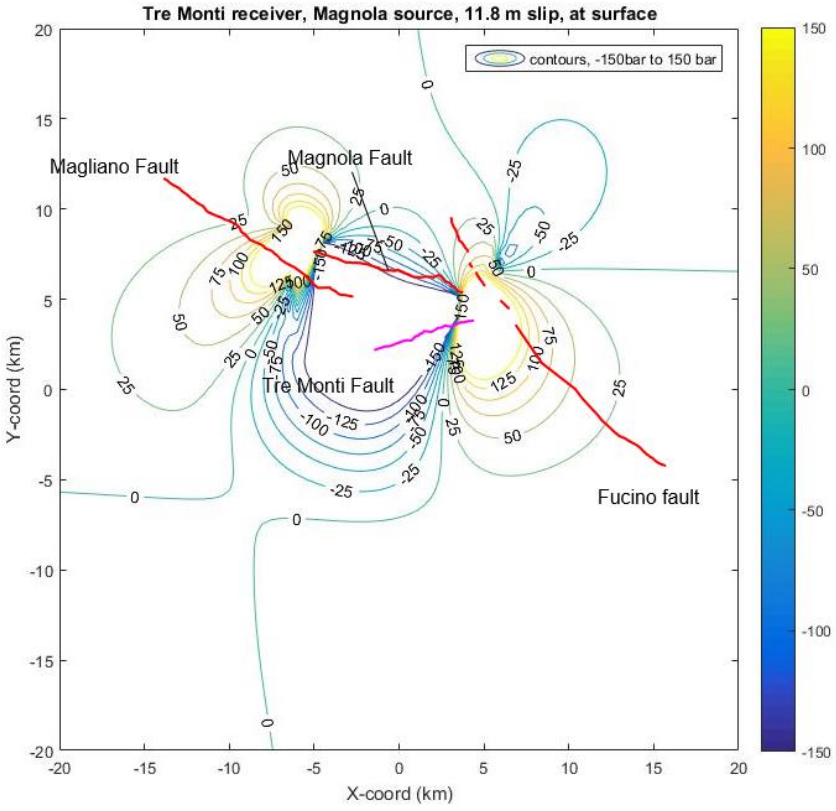

Figure 88 *Coulomb Stress model output for Magnola (source) and Tre Monti (receiver) faults, at 0.1 km depth (surface) shown as a stress contour map superimposed upon the Abruzzo GE .kml file traces for those faults.*

5.6.5 Tre Monti Fault as source and receiver fault segments

Tre Monti's position between and at an angle exceeding 60° to two larger scale faults (Fucino and Magliano) suggests that it might form some type of hard linkage between them, perhaps at depth. However, it does not have a significant degree of strike-slip movement (the slip vector azimuth shown in the GR 2016 spreadsheet measured in previous research is almost at right angles to the strike), and its geometry as a linkage is difficult to square with the geometry of the Magnola fault, which forms a more natural normal fault linkage between the two larger faults.

It is, however, apparent on the ground, and in the "strands" mapped in earlier research that there are a number of overlaps between segments, suggesting that the Tre Monti fault is itself a combination of fault segments (sources) linked by hard linkages (receivers) in the form of either fault bends or relay ramps. A plan view of the Abruzzo GE .kml file traces including the "strands" is at **Figure 89**.

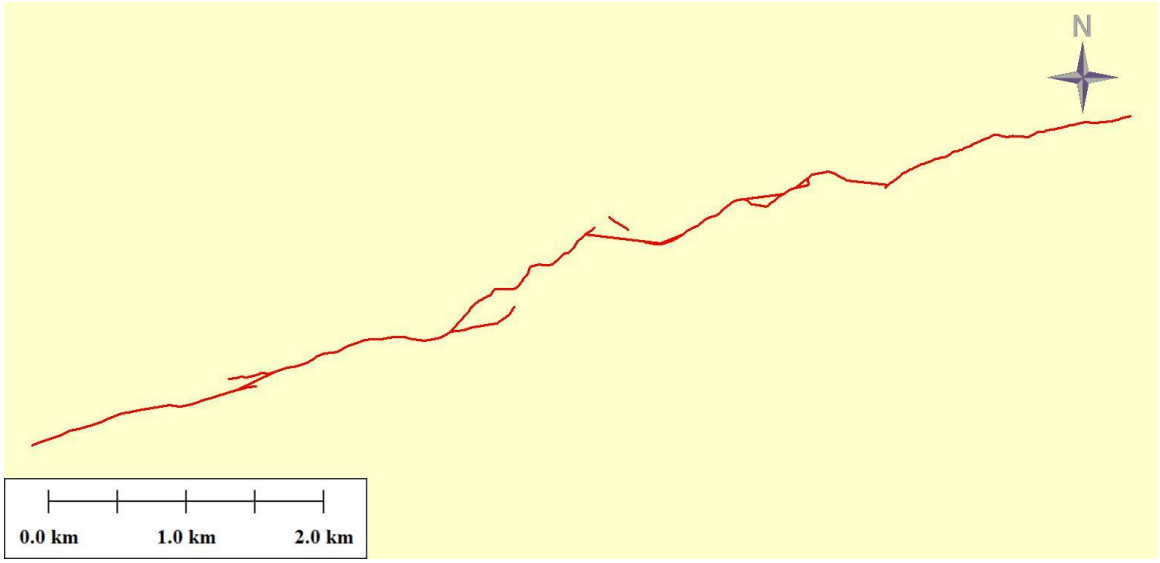

Figure 89 *Map view Abruzzo GE .kml file fault trace profiles for Tre Monti fault, including "at depth" and "strands" traces*

One of the overlaps is at the ENE end of segment D, another between the NE end of segment E and the SW end of segment F. This, and the comparative difficulty in picking the traces linking segments D, E and F together (suggesting less obvious fault scarps from smaller movement) would suggest that the segments with strikes nearer to 060°could be the source segments, and the segments between them (with strikes nearer to 090-100°) the receiver segments (at least at this part of the fault – it could arguably be the other way round further WSW).

Modelling proportionate slip of 1.3 m, 1.3 m and 1 m respectively on segments (from WSW) of 1.1 km (at a strike of 047°), 1 km (strike of 058°) and 0.75 km (strike of 058°) linked by segments of 0.5 km (at a strike of 100°) and 0.4 km (strike of 107°) results in positive change in Coulomb shear stress of ≥80 bar onto the receiving links in each case. **Figures 90, 91, and 92** show the change in each case individually, all shown at the surface. Parameters used are as for the other models, although fault depth is shown as 4 km.

Using the numbering in these figures, the separation between 2 and 3 is ~0.4 km, and the underlap ~0.3 km. Between 4 and 5 the separation is ~0.57 km and the underlap ~0.49 km. The angles between source and receiver (α) are 53°/42° (mean 48°) between 2 and 3, and 49°/49° (mean 49°) between 4 and 5.

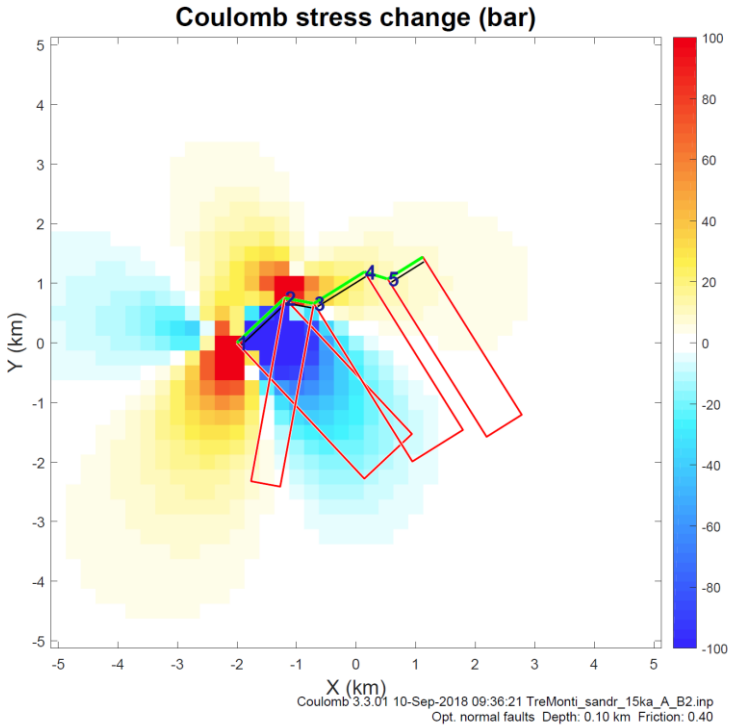

Figure 90 *Coulomb Stress model output for Tre Monti fault segments modelling 1.1 km segment at strike of 047° as the source fault segment (1) onto receiver segments (2 to 5) at 0.1 km depth (surface).*

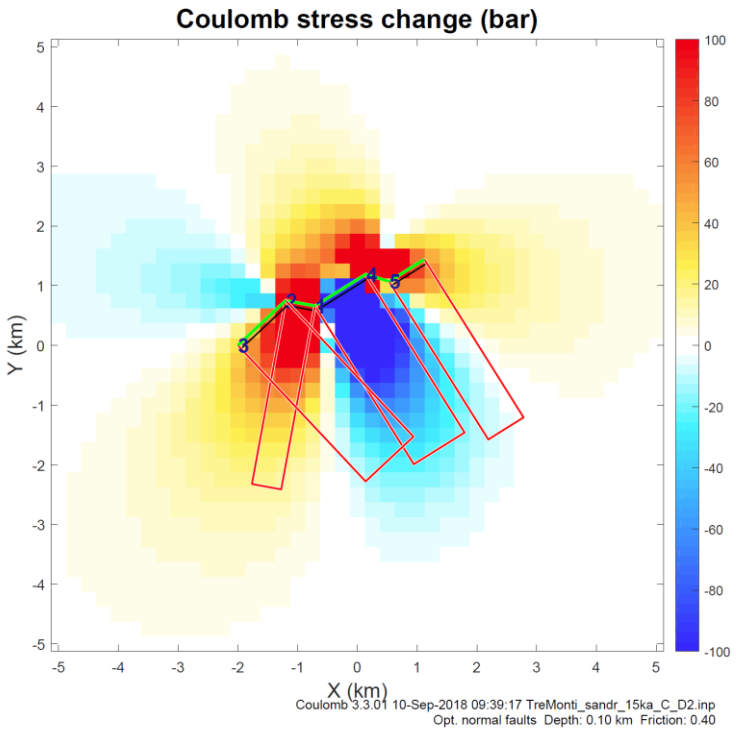

Figure 91 *Coulomb Stress model output for Tre Monti fault segments modelling 1.0 km segment at strike of 058º as the source fault segment (1) onto receiver segments (2 to5) at 0.1 km depth (surface).*

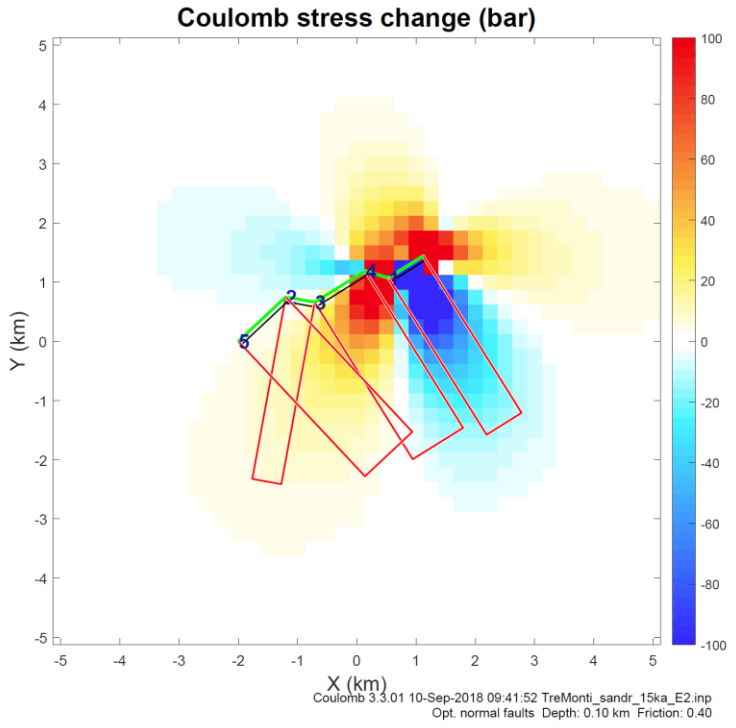

Figure 92 *Coulomb Stress model output for Tre Monti fault segments modelling 0.75 km segment at strike of 058º as the source fault segment (1) onto receiver segments (2 to 5) at 0.1 km depth (surface).*

5.6.6 Summary and possible interpretation of results for Tre Monti

As **Figure 89** shows, the traces for Tre Monti need to be considered in the context of overlapping segment tips. The overall strike of the fault is ~248^{o}, which is ~120^{o} clockwise from the regional norm. It too is located in an area of complicated geometries, down dip from possible source faults to the NW, N and NE (Magliano, Magnola and Fucino faults respectively).

Modelling the Fucino fault as source fault suggests positive Coulomb shear stress change at the W end of the Tre Monti fault of in the region of ~30-40 bar (although negative at the E end). The Magliano fault also is a source of positive stress change, exceeding 50 bar at the W end of the Tre Monti fault, but generally positive by 15 ka along the whole of the Tre Monti fault. The Fucino fault is a source of positive stress change exceeding 100 bar at the E end of the Tre Monti fault (although negative at the W end).

The Tre Monti fault does not obviously represent a hard or soft linkage between any of the other faults, unlike Magnola. It does, however, lend itself to an analysis of internal linkage between source segments at ~055^{o} (SW-NE and shorter receiving linkages at ~105^{o} (WNW-ESE), or possibly the other way around. The more prominent scarp from the former suggests that they might be the more natural source faults, possibly equating to a pre-existing extensional structure trending roughly SW-NE.

The Coulomb stress models showing three of the SW-NE fault segments as the source segments show positive stress change on each of two linking segments ≥ 80 bar. The mean α angles involved are 48^{o} and 49^{o} respectively. For the segments modelled (but not elsewhere in the fault), there is a degree of underlap between the fault tips. This is broadly similar to the amount of separation between the source segments, although precise measurement is difficult with non-parallel and varying strikes (and the probability that the trace seen at the surface does not extend as far as the trace at depth). Values of this sort would put the fault within the area of cross-over between expected fault bend and breached ramp in the Hodge et al, 2018 study. A possible explanation for the variations in sinuosity seen within the Tre Monti fault might be that different linkages apply, with differing angles at various parts of the fault.

In summary, the sinuosity of the Tre Monti traces at fault length scale may be caused by slippage on sub-parallel source fault segments following the line of previous SW-NE structures linking through hard linkages (fault bends and/or breached relay ramps) which follow the line of more recent extensional structures. The source of the initial slippage on the fault segments may have been accumulated slippage on one or more of the neighbouring faults to the N of Tre Monti.

Chapter 6 Discussion

6.1 Reliability of data and methods

6.1.1 Google Earth traces

The study involves an analysis of 85 traces from 28 normal faults at the level of Google Earth trace picking, ranging in length from a few hundred metres to in excess of 10 km, and 121 traces from sections of 4 normal faults at the level of LiDAR trace picking with traces between ~60 m and ~110 m in length. This would be expected to be a sufficiently wide sample basis to identify observable trends within the data, and differences between the datasets.

It is, however, apparent that the data derived from this exercise needs to be treated with caution on a number of grounds. The Google Earth exercise relies on observation of surface features in the form of fault scarps which are often not clear, potentially obscured by vegetation, and possibly subject to erosion or sedimentation. At larger scale, in picking fault traces it is possible to make a general prediction as to how the scarp continues when partially obscured. However, as the purpose of this study is to investigate sinuosity and the reasons for it, such predictions have largely been avoided unless obvious. As already noted within the Methodology, this means that ends and bends of faults are often poorly resolved and therefore under-represented in the fault traces analysed. In a number of cases, the fault scarp visible at the surface and "picked" as traces (compared to the "length at depth" data in the GR 2016 spreadsheet, which assume a continuous fault linked at depth) is only a small percentage of the total fault length. Those traces are therefore less useful and reliable as a source of data than those where a larger percentage is picked. Where the "longer" traces are considered (those which in total amount to >5 km mapped for the fault in question, exceeding 50% of the fault length at depth figure, of which there are 30 identified), the underlying problem of incompleteness of the traces persists. While this might be curable to some extent by extensive field work, this is not practicable in this study.

Reliance on data from the GR 2016 spreadsheet also introduces its own uncertainties, among which is the use of the slip vector azimuth and dip from the cosmogenic ^{36}Cl sites to construct the plane used for the projection of the fault traces. The data itself may well

be an accurate record from careful and diligent field work, and the mean values derived are an average from many measurements. However, a record taken over one relatively small stretch of the fault is not necessarily going to be representative of the fault plane where a given trace is picked for that fault. Even with largely en échelon normal fault segments there are significant divergences in strike within individual faults (as can be seen, for example, from the map views in **Figure 56** in 5.1 above, sometimes by as much as ~50^{o}). A typical dip of ~55^{o} degrees can also vary significantly (not least where the strike of the fault deviates from the regional norm and hard linkages such as fault bends or breached relays are involved).

Slip rates in the GR 2016 spreadsheet are also derived from the cosmogenic ^{36}Cl site investigations, and do not necessarily represent the slip rate in all parts of the fault – the significant differences between the Roberts and Michetti (2004) figures and the GR 2016 spreadsheet figures suggest that the slip rates may vary considerably (and in any event would be expected to vary with distance from the fault tips, and with changes in strike). Hard linkages such as fault bends or breached relays will also have a substantial impact upon the slip rates in those areas, e.g, Wilkinson et al (2014).

6.1.2 LiDAR traces

Caution needs also to be applied to the LiDAR derived traces. The LiDAR images are significantly clearer than the Google Earth images, but introduce their own difficulties – at the scale of a trace section totalling ~50 m with perhaps 12 points picked, is a particular point a tree or a bend in the fault scarp? As an example, an initial pick of a ~60 m trace section for the Fiamignano fault produced an anomalous sinuosity value of > 1.4, but on further examination (comparing the LiDAR images to the Google Earth images for the same section, which showed vegetation), a revised value of 1.1 was found. Also, the areas covered by the LiDAR data are only a small, generally central, part of the faults in question, and therefore not representative of the faults as a whole.

6.1.3 Effect of use of alternative data

Analysing the Roberts and Michetti (2004) slip rates against sinuosity values for a limited number of traces (13) produces a result which suggests that sinuosity decreases with increasing slip rate, whereas the GR 2016 spreadsheet values show the opposite. However, the population is very small, and both results are in any event not statistically

robust. The Roberts and Michetti R^2 value is 0.0718 (R = 0.27), and the "all traces" R^2 value for the GR 2016 spreadsheet data is 0.0248 (R = 0.16), both well below the critical value of R of ~0.50 for which the correlation would be strong.

Replacing the slip vector azimuth and dip with alternative values for 6 sample traces (**Table 4.2.2** and **Figure 36** above) shows that relatively little changes when alternative figures are substituted in deriving a value for sinuosity using the "projection" method to eliminate the effects of topography. Standard deviation figures vary from 0.001 to 0.030, but there is little pattern in the variation, and the smallest range of sinuosity values using various alternative figures (0.077) is obtained using cosmogenic site values for slip vector and azimuth (the approach taken in this study). This would suggest that, at least, using the slip vector azimuth and dip figures in the "projection" method is not obviously wrong, and may be the most consistent approach.

6.1.4 Projected traces v map view approach

Is the "projection" method, aimed at eliminating the effects of topography on sinuosity, necessarily a better way of analysing sinuosity than the Biasi and Wesnousky (2016) and (2017) map view method? Biasi and Wesnousky's approach to determining "squirrel" appears to have been dictated by a pragmatic approach where, looking at a variety of faults at much greater scale, without field data, the authors settled for map view as being acceptable. On the face of it, however, it must lead to distortions where topography exaggerates (or smooths out) apparent sinuosity as the fault scarp follows the topography. The comparison between the two approaches using the Google Earth derived traces (4.4 above) shows that in more than two-thirds of cases, the non-projected approach produces higher sinuosity values than the projected approach, which is perhaps as expected. The remaining cases where the opposite is true are not necessarily anomalies – they may instead reflect that in certain cases the topography has smoothed out sinuosity in map view, and removing the smoothing effect increases sinuosity values. The examples given in paragraph 4.4 of the Barete A and Sulmona B traces demonstrate how changes in dip of the fault plane can alter whether the effect of topography is to smooth out or exaggerate sinuosity.

6.1.5 Coulomb Stress model parameters and assumptions

The Coulomb stress models have all been computed using straight lines for the faults, and a planar fault plane. Neither of these is representative of nature, and Faure Walker et al (2009), Wilkinson et al (2014) and Mildon et al (2017) all caution against the use of planar models to model sub-surface strain transfer between fault segments. In addition, various generalised assumptions have been made in order to present relatively simple models. Length, strike, slip and relative geometries of the faults are taken from a mixture of data in the GR 2016 spreadsheet, and using the measuring tool in Google Earth to approximate the degree of overlap/underlap between the fault tips. Generalisations are also used to set many of the parameters in the Coulomb 3.3.01 software, such as regional stress, seismogenic depth, co-efficient of friction, and depth of calculation.

The respective models of fault growth (constant length versus variable length) over the ~15 ka since the last glaciation also make assumptions about the growth of the faults and amount of slip over that period, which are generalisations – it is known, for example, that for some faults in the SW of the area (including those modelled, such as Magnola), there has been little movement over the last 5 ka (Palumbo et al 2004, Schlagenhauf et al 2011, and Cowie et al 2017), whereas the models all assume slip evenly spread at 3 ka intervals over 15 ka, and (in the case of the variable length model, growth from a starting point of ~ half the current fault length at depth figure from the GR 2016 spreadsheet).

In some of the cases modelled (such as the San Sebastiano fault as a source fault, to the Parasano fault as receiver fault), the area of the receiver fault where there is a significant change in Coulomb shear stress varies substantially depending upon exactly how the fault growth is modelled, or where the fault tip of the source fault is placed over time. Where the stress contour map has been superimposed upon the Abruzzo fault .kml file traces, the differing effects of the varied geometry seen on the ground can be compared to the straight line model, and in a few cases (such as the Fucino fault as source fault for the San Sebastiano receiver fault) there are visible differences.

In each case, single source fault movement has been modelled separately, and modelling of combinations of source faults has not been attempted.

Therefore, the Coulomb Stress modelling exercise is certainly imprecise. However, the Coulomb Stress modelling approach has been adopted to give a general idea of the likely areas of Coulomb stress change in excess of 50 bar for the purposes of assessing sinuosity and its causes, not for a precise calculation of the exact change of Coulomb stress at a particular point, and more complicated modelling across a number of source and receiving faults is impractical in a study of this kind.

Whilst there are some variations shown between the effects using the straight line fault models and the fault trace geometry, in most cases those are not significant compared to the overall picture seen. In all cases, a tapered model for source faults has also been shown alongside the more simplified "slab" model at 15 ka, as a check to see if a more complicated model might produce a significantly different result. In some cases, there is a variation in the extent of stress change (usually, the stress change is greater with the tapered model), and some difference in the location on the receiver fault. The models are shown in **Appendix F**, set against the non-tapered model at 15 ka. However, the extent of the differences is not thought to be material for the relatively broad scale conclusions reached here, and the tapered models are themselves the product of an estimation of possible geometries, so are not necessarily a more accurate representation of the source fault's behaviour.

6.2 Data relationships

6.2.1 Google Earth traces

At the whole fault scale, it is expected that there should be some degree of correlation between sinuosity values (the degree to which a fault trace deviates from a straight line) and other known variables, such as strike, fault length, slip rate, and the position of a trace section within a fault. However, in terms of statistically relevant relationships between sinuosity values and other parameters, the analysis has shown surprisingly little correlation. The sinuosity values for the Google Earth derived traces do not show any particular linear statistical link to length of fault (or trace), nor slip rate. The same applies to both "all traces" and "longer traces" (see 3.1 above for definition).

An R^2 value of 0.10 would give a value for R (the coefficient of multiple correlation) of 0.33, which would suggest a weak/moderate correlation. There are only two R^2 values

recorded in excess of 0.10, one of which is the adjusted comparison of sinuosity values against trace length for the "longer traces" (omitting the results for the Magnola fault) where there is an R^2 figure of 0.1727 (**Figure 34** in 4.1 above). That would give an R value of 0.4156. Even that is not particularly statistically impressive against a critical R value of >~0.50 which would suggest a strong correlation. Trace length as a factor also needs to be treated with caution, as it is primarily a function of the visibility of the fault scarp, not derived directly from any particular attribute of the fault itself. Therefore, this result should probably be regarded as insignificant in establishing a relationship with sinuosity values.

The other R^2 value in excess of 0.10 is the value shown when sinuosity is compared to overall strike (0.635), which would suggest a strong correlation between declining sinuosity and a strike towards 360^o. However, **Figure 28** demonstrates that the link is between lower sinuosity values for faults with a strike of the average of 311^o, or clockwise from that value, with faults with a strike anticlockwise of that value showing either more variable values or higher values. Although the results are distorted to some extent by the results for the Magnola and Tre Monti faults (see 6.2.2. below), this does seem to be potentially statistically significant.

A scatter-plot of the results for sinuosity values against fault length show non-linear decreasing variability as length increases and lower standard deviation values (**Figure 24** in 4.1 above). This suggests that sinuosity is smoothed out as fault length increases, which is as expected.

If the anomalous results for Magnola are omitted, then the "end" longer traces are less sinuous than the "middle" longer traces. This is an unexpected result, as the middle traces might be expected to represent the effect of multiple slips, which would smooth out earlier sinuosity. However, the population is small (particularly in relation to "end" traces), so this result needs to be treated with caution.

There is little difference in the spread of sinuosity values between the "all traces" and "longer traces" results (the latter are in any event included within the former) (see histograms at **Figures 23 and 30** respectively). The mean values for sinuosity are almost identical between the two groups (1.079 for "all traces", and 1.076 for "longer traces").

6.2.2 Outlier results

The histograms (**Figures 23 and 30**) highlight the abnormality of the results for two faults, Magnola and Tre Monti. The former produces the highest average sinuosity values (Magnola A at 1.143 and Magnola B at 1.337). The latter produces the widest range of sinuosity values (from 1.014 to 1.233).

Why do the Google Earth sinuosity values for the Magnola and Tre Monti faults stand out as outliers, compared to the other faults (see **Figure 28** above)? The position of the two faults is discussed in more detail below in 6.3. However, in short, the difference seems to be related to their geometry, and geometrical relationship to other neighbouring faults. They are noticeably different in strike from the regional trend (the average strike and dip for the 28 faults is 311/55), and from their neighbours. For the Magnola fault, the overall strike of the fault is 290^{o}, and dip at the Palumbo (2004) cosmogenic site is 42^{o}. For the Tre Monti fault, the overall strike is 248^{o} and dip 52^{o}.

While Tre Monti is unique in its strike among the 28 faults studied, Magnola's overall strike is not significantly different from some of the other faults studied, such as Assergi (288^{o}) and Campo Felice (296^{o}). Those faults also produce sinuosity values for some of their traces which are among the highest - Assergi (which, like Tre Monti, has a wide spread of results) has sinuosity values of 1.161 and 1.184 (traces 2 and 3), and Campo Felice 1.165 (trace 1B). Those three traces, with Magnola B (1.337) and Tre Monti E (1.233) make up five of the top six values obtained (the exception being Sulmona, strike 334^{o}, sinuosity value 1.225).

The strikes of all of these four faults are anticlockwise of the regional average of ~310-320^{o}, the Tre Monti fault in particular trending towards SSW-NNE. The anticlockwise variance brings the faults closer to the previous extensional stress regime, which left inherited structures trending broadly SW-NE. The current extensional regime will clearly control the preferred orientation for any propagation, and in line with other inherited NW-SE structures. A fault trending more in line with the current regional extensional pattern could be expected to propagate through linkage of parallel segments along strike (Hodge et al 2018), and therefore to produce a trace which should be less sinuous. However, for a fault trace deviating from the regional regime, the minor WSW-ENE and SSW-NNE structures (whilst otherwise acting as barriers to fault propagation), could be

reactivated as transfer faults or segments between en échelon faults or fault segments (see Pizzi and Galadini (2009) and Pizzi and Scisciani (2000)), particularly in left-stepping (anticlockwise) situations. The Tre Monti fault in particular seems to be an example where the minor structures may have had a significant part to play in its evolution, and the sinuosity seen at the surface. The central traces from the Tre Monti fault at surface (C and D) are shown in **Figure 93** below, set against possible inherited structures, to show how the traces could have evolved and be influenced by such structures.

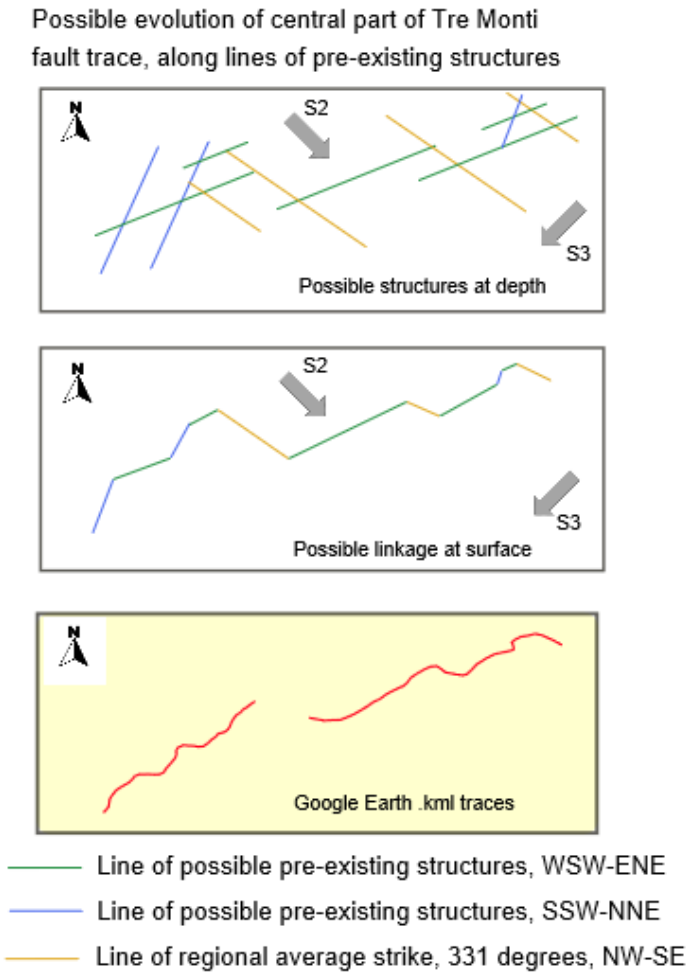

Figure 93 *Cartoon illustrating possible development of central parts of Tre Monti fault, along lines of pre-existing structures, blue lines possible WSW-ENE structures, green lines possible SSW-NNE structures, yellow lines present day extensional fault average strike. Red traces are Abruzzo GE .kml file traces Tre Monti C and D*

6.2.3 Comparison of Google Earth and LiDAR traces

The sinuosity values for the smaller scale (< 100 m) traces are expected to be more variable than the whole fault length traces, and to be more influenced by localised

features such as fracture patterns. It might be expected that the sinuosity values of the smaller scale traces would cover a wider range of values, as the effect of more varied localised sinuosity would be smoothed out over longer fault traces.

The LiDAR derived traces produce a range of results for sinuosity values (see histogram at **Figure 37** above) which are similar to the Google Earth values (histogram at **Figure 23**), despite the difference in scale. The mean sinuosity value for the LiDAR derived traces is 1.087, which is slightly higher than the "longer traces" mean sinuosity value of 1.076, but not significantly so. The reasonable degree of similarity suggests that there is relatively little difference between mean values taken from a small, central, section of the fault (the LiDAR derived traces) and those taken from a wider spread of the fault trace.

By individual fault, for the Campo Felice fault the weighted average sinuosity value for the LiDAR traces is 1.117, and for the Google Earth traces the average is 1.112. The comparable figures for the other faults are for Fiamignano 1.066 v 1.061, for Magnola 1.030 v 1.143/1.337, and for Parasano 1.062 v 1.061. The LiDAR data for Magnola happen to cover an area where there is little sinuosity, and which is not representative of the fault as a whole (see **Figure 65** above), so the differences there are unsurprising. The other values are remarkably similar – particularly in the cases of the Fiamignano and Parasano faults, where the LiDAR traces cover a relatively small proportion of the faults compared to the Google Earth traces.

The range for the LiDAR derived traces includes both a greater number of low (<1.05) sinuosity values, and values in excess of the highest values seen in relation to the Google Earth derived traces, appearing to confirm the hypothesis as to the greater and more variable spread of results for the smaller traces sinuosity values.

6.2.4 Effect of pre-existing structures at small scale

Local features including pre-existing structures reflected in fracture patterns are hypothesised to be a primary control on sinuosity values at small scale. The data analysed at the smallest scale in this study (with traces <110 m in length) is not extensive, but nevertheless seems to give a reasonable indication of the extent to which localised features are influenced by pre-existing structures, notably fracture sets pre-dating the more recent normal faulting. The co-planar features identified through the use of the

VRGS software for each of the Campo Felice, Fiamignano, and Parasano faults suggest patterns of near vertical fractures along similar bearings (primarily SW-NE), with a corresponding set of near vertical fractures bearing NW-SE (see **Figures 43 to 45** in 4.5 above).

Previous researchers such as Pizzi and Galadini (2009) and Civico et al (2017) identified extensional pre-existing structures trending NNE-SSW and ENE-WSW in the context of neighbouring fault systems, subsequently cross-cut by WNW-ESE trending faulting. Vitale et al (2012) identified fracture patterns at the surface following the same trends, with near vertical fractures trending NNE-SSW and WNW-ESE.

Field evidence suggests the same subsequent cross-cutting relationship as identified by Civico et al (2017).

Importing the LiDAR derived fault traces into Google Earth gives the LiDAR traces context, and enables the sinuosity seen to be matched to features on the ground (although with reservations about the 30 m resolution of the SRTM images). This is examined for the more obviously sinuous elements of the profiles identified for three of the faults, Campo Felice (two locations), Fiamignano and Parasano. The profile for the Magnola fault does not reveal any notable change in sinuosity, and the traces for that fault are in any event less detailed (at ~110 m) than the traces for the other faults (at ~50-60 m), reflecting the quality of the images.

The images for both Campo Felice and Parasano (**Figures 48, 49 and 53**) suggest side-stepping of the fault trace along lines consistent with near vertical fractures trending SW-NE and SSW-NNE respectively, also reflected by the gullies seen in the footwalls both where the slippage has occurred, and elsewhere in that vicinity, linked by small-scale bends in the scarp trace. The slippage does not appear to be uniformly in any one direction (left-stepping or right-stepping), but from the limited data available the apparent deviations appear to be consistent with small scale sinuosity being influenced by the pre-existing structures represented in the fracture patterns. This is not necessarily borne out in the case of the Fiamignano fault, where the apparent deviation in the LiDAR derived traces does not fit with that pattern. However, the Google Earth image (**Figure 51**) suggests that the LiDAR derived traces might be inaccurate at this point due possibly

to misidentifying vegetation as fault scarp, and that the deviation of the fault trace is actually closer to the SW-NE direction seen with the other faults. Field work would hopefully be able to resolve that issue with greater certainty, and it is to be noted that the footwall above the traces at that point appears to be cut by gullies trending SSW-NNE at ~030-040^{o}.

This dataset is small (only 4 locations in total are investigated in this way). However, the data suggests that pre-existing structures (reflected in local topographical features) may exert a control over surface sinuosity at the scale of < 100 m. This could perhaps be the result of fault tips propagating upwards as the faults grow, and being deflected at the surface along pre-existing fractures or lines of weakness. Further work in the field and/or more extensive LiDAR datasets would be required to test this hypothesis further.

6.3 Coulomb Stress modelling at whole fault length scale

The analysis of sinuosity at fault scale using Coulomb Stress modelling involves two strands at different scales: one to investigate the likely impact of neighbouring faults as source faults leading to shear stress change which may in turn be reflected in deviations in fault strike seen at surface; the other is to investigate whether the internal sinuosity of a particular fault as seen at the surface may be related to linking of fault segments during the growth of the fault over the last ~15 ka. Positive stress transfer exceeding 50 bar (5 MPa) is taken as the starting point for likely activation or reactivation of a receiver fault or fault segment.

As noted above, modelling Coulomb stress change in this way inevitably involves some generalisation and approximation. Even with approximate geometries and known attributes such as regional stress, slip rate and strike and dip of the faults, the faults (or segments) are modelled as projected planes from straight lines at the surface, when in nature they are not. Fault slip is assumed at regular intervals over ~15 ka, when that is highly unlikely in practice, and in this study more complicated modelling of the cumulative effect of multiple source faults has not been attempted.

Even with these uncertainties, the modelling shows that elements of sinuosity at the whole fault scale can often be explained by reference to the geometry of neighbouring

faults, and the likely areas of positive Coulomb shear stress change resulting from movement on those faults.

At the smaller of the two scales, in some cases such as Fiamignano, Parasano and Tre Monti, much of the sinuosity of the traces can be attributed to the formation of hard linkages between fault segments within the fault in the form of fault bends or breached relay ramps (the sinuosity is the result of the previous geometry between the fault segments and either reactivated older structures or new structures which are now linked). The initial trigger for movement of the source segments may in turn be movement on a neighbouring fault (as in the case of Fiamignano, where movement on the Rieti fault may have triggered movement on the segments at the NW end of the Fiamignano fault).

At the larger scale, in other cases such as Magnola, the fault itself appears to be part of a developing linkage between other neighbouring faults, in the form of either a new structure or a reactivated older structure. The anomalously high trace sinuosity value for Magnola seen using Google Earth picking (Magnola B) appears to be linked to a possible linkage of pre-existing structures, at a point where the modelled stress change resulting from movement on neighbouring faults changes from positive to negative.

The geometries involved with the possibly reactivated older structures appear to coincide with structures found in previous research (in particular SW-NE trending extensional structures cross-cut by subsequent NW-SE trending extensional structures – Pizzi and Galadini (2009), Pizzi and Scisciani (2000) and Civico et al (2017)). The geometries of linkages between fault segments appear consistent with models computed in Hodge et al (2018).

The scale and approximations involved in the Coulomb Stress modelling mean that there is relatively little useful insight into models of fault growth. Both constant length and variable length source faults have been modelled for each fault, and are explained in more detail in **Appendix F.** However, the principal difference shown between the two models is the location of the stress change on the receiving fault. At 15 ka the position is the same on both models, as the fault has reached its fullest extent as seen at the surface. In most cases, 15 ka is also the time at which any positive stress change is at its greatest. In some cases, such as the model of the Fucino fault as the source fault for the Parasano fault,

there is some early positive stress change which develops into negative stress change by 15 ka, but the early positive stress change is insignificant, and its effect in the development of the receiver fault is indistinguishable.

The interpretation of the Fiamignano, Parasano and Tre Monti faults as being instances of developing hard linkages between en échelon fault segments is more consistent with a constant length model.

6.4 Implications of research for seismic hazard evaluations

Sinuosity of surface fault traces is a characteristic which is measurable at different scales in the great majority of faults in an active tectonic regime such as the Apennines. Where variations in sinuosity help to improve the understanding of the factors which have led to those variations, those can assist in seismic hazard evaluation in such areas. Although inconclusive in some of its results, this research shows that characterising sinuosity can be helpful in identifying the respective roles of larger scale features (such as the geometric location of a fault relative to neighbouring faults, and its bearing relative to regional strike) and smaller-scale heterogeneous features (such as fracture patterns, which might in turn reflect inherited structures), in the geomorphology of the fault trace. With further research, as identified below, an understanding of how sinuosity of a fault trace varies with scale could represent a useful tool in the armoury of a structural geologist engaged in seismic hazard evaluation.

6.5 How might the findings of the research apply to other fault systems?

The lithology of the fault system studied is almost exclusively carbonates. The system is an active one and faults within the system are still developing, even if some (to the SW) may be temporarily less active than others (Cowie et al 2017). The faults studied are exclusively normal faults, predominantly en échelon. It is unlikely, therefore, that the findings would necessarily be replicated in more mature, and more complicated fault systems (perhaps with a greater degree of strike slip movement). Therefore, while providing some insight into the sinuosity seen in this active, and important fault system, this study's wider usefulness might be limited to similar systems elsewhere, or to faults elsewhere within the same Apennines system. A system with different lithologies is likely to present an opportunity for study of the effect of sinuosity of different rock competences, which was not the case here. A more mature system would present

different challenges – possibly more developed linkages between fault segments, for example, but with more erosion.

6.6 Suggestions for further research.

The use of Google Earth and LiDAR datasets, whilst not without its difficulties, has at least enabled a relatively large sample of faults (28) to be analysed in this study. It is considered that at least a similar size sample of faults would need to be examined in any subsequent study to be able to identify any relationships. This means that, although fieldwork would undoubtedly improve some of the accuracy of the results, it is not a realistic proposition over such a large scale if that is the primary aim of any further study. A possible alternative could be the use of higher resolution topography data if available, perhaps combined with automatic fault trace picking if that could be designed to be sufficiently reliable.

As noted above, the faults scarps studied here are relatively new, and the system is still active. That has its advantages, in terms of visibility, lack of erosion of the scarp, and a fixed reference point of ~15 ka since slip is recorded in the geomorphology. However, it also has potential disadvantages in terms of the maturity of the faults, with the sinuosity seen effectively a current (and evolving) position on faults with different slip histories, rather than a fully evolved one. If this study were to be repeated elsewhere, the challenge would be to find a mature system, but where the scarp remains sufficiently visible through remote study to be capable of producing useful results (implying an area with relatively little erosion). Google Earth data is ubiquitous, although not of uniform resolution. However, LiDAR or higher resolution satellite data would also be needed to complete the picture.

Investigating systems with differing lithologies (either between systems, or within one system) could be informative in comparing results between lithologies, and also in assessing the effects on sinuosity of mechanical stratigraphy where the lithologies are contiguous. Again, the challenge would be to identify appropriate systems where data are available.

A comparison between the sinuosity results obtained from normal and strike-slip faulting would also potentially be informative. However, that would also be challenging, firstly in identifying locations where the sinuosity in the fault trace derived from strike slip

movement could be identified on the surface, and secondly in being able successfully to differentiate between the effects of strike-slip and normal fault movement (one rarely being present without the other to some degree).

Fieldwork could be helpful if the purpose of a further study were to investigate localised features that could contribute to sinuosity seen at small scale. The localised results used here have been informative for the purposes of seeking to understand why sinuosity seen at the smaller scale is different from sinuosity at larger scale. However, a wider study of small scale sinuosity on its own, which realistically would not cover more than small segments of perhaps a few faults, is not expected to yield results which would help inform understanding of fault growth.

Chapter 7 Conclusions

This study investigates the morphology of fault traces seen at the Earth's surface in a new way compared to previous research. It incorporates new remote sensed datasets which give better definition of the fault traces than in previous studies. The method used includes a technique to eliminate the distorting effects of topography, previously largely ignored. It considers a relatively homogeneous set of normal faults with comparable characteristics, rather than a range of types of faults whose characteristics are not readily comparable. The approach studies the sinuosity of fault traces at a variety of scales, rather than concentrating solely on one scale. It therefore represents a different approach from previous work, which could be expected to provide insight into what factors control sinuosity at the scales studied.

The results are, in many cases, as expected. Stress interaction between neighbouring faults and between en échelon segments within a fault appear to be the main controls on trace sinuosity at the whole fault scale. At the whole fault scale, sinuosity appears to be smoothed out over time, with repeated slip, particularly in the more central parts of the fault trace, where slip has been greatest.

At smaller scale, sinuosity is more variable and values are spread over a wider range than at the whole fault scale. Local features such as pre-existing fractures or weaknesses appear to be a principal control over deviation at a scale of < 100 m, and sinuosity at that scale is apparently not much influenced by the factors controlling sinuosity at the whole fault scale.

The linear correlations between sinuosity values and fault length and slip rate respectively are at best weak. This would perhaps be more surprising for fault length than for slip rate, but a scatterplot of fault length values demonstrates that there is a non-linear overall relationship in which sinuosity values decline and are less variable with increasing fault length. Slip rate values need to be treated with some caution, as a single slip rate has been applied across a fault's length, when that is unlikely to be the case in practice. Therefore, the absence of a relationship in this study might not be conclusive.

Deviance from the current regional stress pattern appears to be a possibly significant factor in controlling sinuosity at the whole fault level. Anticlockwise deviance from the

regional stress pattern appears to coincide with an increase in sinuosity values in a number of cases. The data in this respect highlight two faults, Tre Monti and Magnola and perhaps not too many inferences should be drawn from only two examples. However, the data from the Assergi and Campo Felice faults, which also strike anticlockwise from the regional average, help to reinforce that trend. The anticlockwise variance brings the faults closer to the previous extensional stress regime, which left inherited structures trending broadly SW-NE. The current extensional regime will clearly control the preferred orientation for any propagation, and in line with other inherited NW-SE structures. However, the minor WSW-ENE and SSW-NNE structures (whilst otherwise acting as barriers to fault propagation), could be reactivated as transfer faults or segments between en échelon faults or fault segments, particularly in left-stepping (anticlockwise) situations. Therefore, the deviation of strike towards an anticlockwise direction might be an indication of areas where the more minor structures have played a relatively large role in controlling the propagation direction of the faults in question. The Tre Monti fault appears to be the clearest example of that effect in the faults studied.

Understanding the relationship between the factors controlling sinuosity at varying scales has a potential impact upon seismic hazard evaluation in seismically active areas where those effects can be observed at differing scales (such as in the study area of the Apennines in Italy). This study shows the importance of considering a variety of scales when characterising the sinuosity observed in the fault trace.

List of Appendices (on separate CD)

Appendix A - Data extracted from 2016 Gerald Roberts spreadsheet

Appendix B - Fault traces data spreadsheet, all traces from Google Earth

Appendix C - Spreadsheet of Longer traces from Google Earth

Appendix D - Spreadsheet showing data used in comparison of throw rate values between Roberts and Michetti, 2004 and FW 2016 spreadsheet

Appendix E - Comparison of sinuosity values for Google Earth fault traces using projected or non-projected methods (reducing or preserving the effects of topography)

Appendix F - LiDAR fault trace data

Appendix G - Change in Coulomb shear stresses over time and on differing models of fault growth

References

Allmendinger, R. W., Cardozo, N., and Fisher, D., 2012, Structural geology algorithms: Vectors and tensors in structural geology: Cambridge University Press

Anderson, H., Jackson, J., 1987, Active tectonics of the Adriatic Region, *Geophysical Journal International* 93, (1987) issue 3, 937-983

Biasi, G. P., and Wesnousky, S.G., 2016, Steps and Gaps in Ground Ruptures: Empirical Bounds on Rupture Propagation, *Bulletin of the Seismological Society of America*, (2016) Vol 106, no 3, 1110-1124

Biasi, G.P., and Wesnousky, S.G., 2017, Bends and Ends of Surface Ruptures*, Bulletin of the Seismological Society of America* (2017) Vol 107 no 6, 2543-2560

Bubeck, A., Wilkinson, M., Roberts, G.P., Cowie, P.A., McCaffrey, K.J.W., Phillips, R., Sammonds, P., 2015, The tectonic geomorphology of bedrock scarps of active normal faults in the Italian Apennines mapped using combined ground penetrating radar and terrestrial laser scanning, *Geomorphology* 237 (2015) 38-51

Cardozo, N., and Allmendinger, R.W., 2013, Spherical projections with OSXStereonet: Computers & Geosciences, v. 51, p. 193 – 205, doi:10.1016/j.cageo.2012.07.021

Candela, T., Renard, F., Schmittbuhl, J., Bouchon, M., Brodsky, E.E., 2011, Fault slip distribution and fault roughness, *Geophysical Journal International* (2011) 187, 959-968

Childs, C., Watterson, J., and Walsh, J. J., 1995, Fault overlap zones within developing normal fault systems, *Journal of the Geological Society*, vol 152, (1995), 535-549

Civico, R., Sapia, V., Di Giulio, G., Villani, F., Pucci, S., Baccheschi, P., Amoroso, S., Cantore, L., Di Naccio, D., Hailemikael, S., Smedile, A., Vassallo, M., Marchetti, M., Pantosti, D., 2017, Geometry and evolution of a fault-controlled Quaternary basin by means of TDEM and single-station ambient vibration surveys: The example of the 2009 L'Aquila earthquake area, central Italy, *Journal of Geophysical Research: Solid Earth* 122, 2236-2259

Cowie, P.A., et al, 2017, Orogen-scale uplift in the central Italian Apennines drives episodic behaviour of earthquake faults, *Scientific Reports*, 2017, 1-10

Faure Walker, J.P., Roberts, G.P., Cowie, P.A., Papanikolaou, I.D., Sammonds, P.R., Michetti, A.M., and Phillips, R. J., 2009, Horizontal strain-rates and throw-rates across breached relay zones, Central Italy: Implications for the preservation of throw deficits at points of normal fault linkage, *Journal of Structural Geology* 31, (2009) 1145-1160

Faure Walker, J.P., Roberts, G.P., Cowie, P.A., Papanikolaou, I., Michetti, A.M., Sammonds, P., Wilkinson, M., McCaffrey, K.J.W., Phillips, R.J., 2012, Relationship between topography, rates of extension and mantle dynamics in the actively-extending Italian Apennines, *Earth and Planetary Science Letters* 325-326, (2012) 76-84

Faure Walker, J. P., Visini, F., Roberts, G., Galasso, C., McCaffrey, K., Mildon, Z., 2019, Variable Fault Geometry Suggests Detailed Fault Slip-Rate Profiles and Geometries Are Needed for Fault-Based Probabilistic Seismic Hazard Assessment (PHSA), *Bulletin of the Seismological Society of America*, Vol 109, no 1, pp 110-123

Fossen, H. (2016), *Structural Geology (2nd Edition),* Cambridge, Cambridge University Press

Giraudi, C., Frezzotti, M., 1997, Late Pleistocene Glacial Events in the Central Apennines, Italy, *Quaternary Research, 48*(3), 280-290

Guerriero, V., Iannace, A., Mazzoli, S., Parente, M., Vitale, S., Giorgioni, M., 2010, Quantifying uncertainties in multi-scale studies of fractured reservoir analogues: Implemented statistical analysis of scan line data from carbonate rocks, *Journal of Structural Geology* 32 (2010), 1271-1278

Guerriero, V., Vitale, S., Ciarcia, S., Mazzoli, S., 2011, Improved statistical multi-scale analysis of fractured reservoir analogues, *Tectonophysics* 504 (2011), 14-24

Gupta, A., Scholz, C.H., 1998. Utility of elastic models in predicting fault displacement Fields, *Journal of Geophysical Research* 103 (B1), 823-834

Gupta, A., Scholz, C.H., 2000. A model of normal fault interaction based on observations and theory, *Journal of Structural Geology* 22 (7), 865-879

Hodge, M., Fagereng, A., Biggs, J., 2018, The role of coseismic Coulomb stress changes in shaping the hard link between normal fault segments, *Journal of Geophysical Research: Solid Earth* 123, 797-814

Horacio, J., 2014, River sinuosity index: geomorphological characterisation. Technical Note 2. CIREF and Wetlands International

Huggins, P., Watterson, J., Walsh, J.J., Childs, C., 1995, Relay zone geometry and displacement transfer between normal faults recorded in coal-mine plans, *Journal of Structural Geology* 17, 1741–1755

Jackson, C.A-L., Bell, R.E., Rotevatn, A., Tvedt, A.B.M., 2017, Techniques to determine the kinematics of synsedimentary normal faults and implications for fault growth models, In Childs et al (2017) The Geometry and Growth of Normal Faults, *Geological Society of London Special Publications* vol 439(1), 187-218

Jolivet, L., Faccenna, C., Goffe, B., Mattei, M., Rossetti, F., Brunet, C., Storti, F., Funiciello, R., Cadet, J-P, d'Agostino, N., Parra, T., 1998, Mid-crustal shear zones in postorogenic extension: Example from the north Tyrrhenian Sea, *Journal of Geophysical Research* 103, (1998), No B6, 12,123-12,160

Leopold, B.L., Wolman, M.G., and Miller, J.P., (1964), *Fluvial processes in Geomorphology,* New York, Dover Publications (1995) (first published San Francisco, WH Freeman & Co)

Lin, J. and Stein, R.S., 2004, Stress triggering in thrust and subduction earthquakes, and stress interaction between the southern San Andreas and nearby thrust and strike-slip faults, *Journal of Geophysical Research* 109, B02303, doi:10.1029/2003JB002607

Marchal, D., Guiraud, M. and Rives, T., 2001, Geometric and morphology evolution of normal fault planes and traces from 2D to 4 D data, *Journal of Structural Geology* 25, (2003) 135-138

Marchegiani, L., Van Dijk, J.P., Gillespie, P.A., Tondi, E., Cello, G., 2006, Scaling properties of the dimensional and spatial characteristics of fault and fracture systems in the Majella Mountain, central Italy, *Geolsoc London Special Publications,* (2006) *2*61, 113-131

Mildon, Z.K., Robert, G.P, Faure Walker, J.P., Iezzi, F, 2017, Coulomb stress transfer and fault interaction over millennia on non-planar active normal faults: the M_w 6.5-5.0 seismic sequence of 2016-2017, central Italy, *Geophysical Journal International* (2017) 210, 2016-1218

Mueller, J. (1968). An Introduction to the Hydraulic and Topographic Sinuosity Indexes. *Annals of the Association of American Geographers, 58*(2), 371-385. Retrieved from http://www.jstor.org.ezphost.dur.ac.uk/stable/2561621

Palumbo, L., Benedetti, L., Bourles, D., Cinque, A., Finkel, R., 2004, Slip History of the Magnola fault (Apennines, Central Italy) from ^{36}Cl surface exposure dating: evidence for strong earthquakes over the Holocene, *Earth and Planetary Science Letters,* 225 (2004) 163-176

Pizzi, A. and Scisciani, V., 2000, Methods for determining the Pleistocene-Holocene component on active faults reactivating pre-Quaternary structures: examples from the central Apennines (Italy), *Journal of Geodynamics*, 29 (2000) 445-457

Pizzi, A. and Galadini, F., 2009, Pre-existing structures and active fault segmentation in the northern-central Apennines (Italy), *Tectonophysics*, 476 (2009) 304-319

Roberts, G.P, and Michetti, A.M., 2004, Spatial and temporal variations in growth rates along active normal fault systems, an example from The Lazio-Abruzzo Apennines, central Italy, *Journal of Structural Geology* 26, (2004) 339-376

Roberts, G.P., Cowie, P., Papanikolaou, I., and Michetti, A.M., 2004, Fault scaling relationships, deformation rates and seismic hazards: an example from the Lazio–Abruzzo Apennines, central Italy, *Journal of Structural Geology* 26, (2004) 377-798

Roberts, G.P., 2008, Visualisation of active normal fault scarps in the Apennines, Italy: a key to assessment of tectonic strain release and earthquake rupture. *Google Earth Science, Journal of the Virtual Explorer* 29 (4), ISSN 1441-8142

Sagy, A., Tesei, T., and Collettini, C., 2017, Fault-surface geometry controlled by faulting mechanisms: Experimental observation in limestone faults, *Geology*, September 2017, v 45, no 9, 851-854

Schlagenhauf, A., Manighetti, I., Benedetti, L., Gaudemer, Y., Finkel, R., Malavieille, J., Pou, K., 2011, Earthquake supercycles in Central Italy, inferred from ^{36}Cl exposure dating, *Earth and Planetary Science Letters,* 307 (2011) 487-500

Toda, S., Stein, R. S., Richards-Dinger, K. and Bozkurt, S., 2005, Forecasting the evolution of seismicity in southern California: Animations built on earthquake stress transfer, *Journal of Geophysical Research* 110, B05S16, doi:10.1029/2004JB003415

Walsh, J.J., Bailey, W.R., Childs, C., Nicol, A., Bonsona, C.G., 2002, Formation of segmented normal faults: a 3-D perspective, *Journal of Structural Geology* 25, (2003) 1251-1262

Walters, R.J., Gregory, L.N., Wedmore, L.N.J., Craig, T.J., McCaffrey, K.M., Wilkinson, M., Chen, J., Li, Z., Elliott, J.R., Goodall, H., Iezzi, F., Livio, L., Michetti, A.M., Roberts, G., Vittori, E., 2018, *Earth and Planetary Science Letters,* 500 (2018) 1-14